Chair of Processing of Composites and Design for Recycling

Doctoral Thesis

Inline Process Monitoring Using Near-Infrared Spectroscopy in Liquid Composite Molding Processes: Measurement and Analysis of Critical Parameters in Epoxy/Amine Resin Systems

Moritz Salzmann, M.Sc.

July 2024

MONTANUNIVERSITÄT LEOBEN
www.unileoben.ac.at

AFFIDAVIT

I declare on oath that I wrote this thesis independently, did not use any sources and aids other than those specified, have fully and truthfully reported the use of generative methods and models of artificial intelligence, and did not otherwise use any other unauthorized aids.

I declare that I have read, understood and complied with the "Good Scientific Practice" of the Montanuniversität Leoben.

Furthermore, I declare that the electronic and printed versions of the submitted thesis are identical in form and content.

Date 21.07.2024

_____

Signature Author
Moritz Salzmann

To the two professors who shaped my scientific perspective more than anyone else, yet did not live to see the completion of this work.

To my grandfather Prof. Helmut Salzmann, known as Rainer, who will always be a role model for me and who, even after losing his sight, supported me in my first publication.

And to Prof. Ralf Schledjewski, who was an irreplaceable mentor, believed in me, and gave me the space and time to develop.

Acknowlegdement

This work would not have been possible without the support and encouragement of a number of people, to whom I would like to express my gratitude here.

I would like to thank my supervisor, Univ-Prof. Dr.-Ing. Ralf Schledjewski, for the opportunity to work and learn at the LVV (Processing of Composite Group, Montanuniversität Leoben). His support, guidance, and feedback helped me along my path to this thesis. Over time, his calm and stoic way of assessing situations also became a role model for me. I also want to thank assoz.Prof. Dipl.-Ing. Dr.mont. Ewald Fauster, who took over the leadership of the LVV after Ralf's unexpected death and provided a safe environment for me and my colleagues. His expertise and scientific discussions, as well as his support with laboratory equipment, were invaluable even before. Thank you, Ewald, for taking over my supervision during this difficult time and guiding me through the final steps. As a mentor and chemist, Univ.-Prof. Mag.rer.nat. Dr.techn. Wolfgang Kern always had a different, helpful perspective on things and was a pleasant sparring partner for scientific questions.

I would also like to thank the staff of the LVV, especially my long-time colleagues Ulrike Kirschnick, Neha Yadav, Stefan Neunkirchen, Marcel Bender, Alexander Legenstein, and Bharath Ravindran for their collaboration, camaraderie, and good times together at the LVV. Additionally, I want to thank my early colleagues at the LVV, Patrick Hergan and Yannick Blößl, from whom I learned a great deal. Furthermore, I thank the non-scientific staff Inge Kaindl, Nadine Stückler, Oliver Rausch-Schott, and Stefan Oswald for their support in various administrative and laboratory-related matters. You all made my time at the LVV much easier.

I am very grateful to the team at i-Red Infrarotsysteme GmbH, Wolfgang Märzinger, Michael Teuchtmann, and Moritz Priglinger, for their support and technical discussions. You were always immediately helpful and attentive to problems. Without your support, this work would not have been possible in its current form.

Moreover, I would like to thank all my friends for their support. My deepest gratitude goes to my family and my girlfriend Chiara, who supported me with full energy throughout the entire time.

Kurzfassung

Steigende Anforderungen an Qualitätssicherung, Prozessstabilität und -kontrolle erzeugen den Bedarf nach effizienter Erfassung, Verarbeitung und Analyse von Prozess- bzw. Produkt-relevanten Messgrößen während der Fertigung, bereits im Prozess, also inline. Häufig bringt dies außerdem ökonomische und ökologische Vorteile durch eine Reduzierung des Ausschusses und kürzere Prozesszeiten. Welche Parameter inline messbar sind, hängt von der jeweiligen Technologie ab. Eine bei der Verarbeitung Faser-Kunststoff-Verbundwerkstoff bisher kaum untersuchte Methode zum inline Monitoring, aber breit anwendbare Technologie ist die Nahinfrarot Spektroskopie (engl. Near-infrared spectroscopy). Sie nutzt, von elektromagnetischen Wellen im Bereich von 750-2500 nm angeregten Kombinations- und Obertonschwingungen funktioneller Gruppen. Aus den gemessenen Spektren können Parameter mittels Partial Least Square Regression bestimmt werden, die mit den Konzentrationen funktioneller Gruppen im Messvolumen in Zusammenhang stehen.

In der vorliegenden Arbeit werden Anwendungsmöglichkeiten der Nahinfrarot Spektroskopie zur Überwachung von Flüssigimprägnierverfahren (engl. liquid composite moulding processes) untersucht. Flüssigimprägnierverfahren wurden als Beispiel gewählt, da sich hier die wesentlichen Prozessschritte in Bezug auf die Verarbeitung des Harzsystems gut messen lassen. Außerdem erlaubt sie die Betrachtung unterschiedlicher, aber relevanter Messfälle, wie beispielsweise am reinen Harzsystem, durch Folien hindurch oder in geschlossenen Formwerkzeugen. Inline gemessen wurden dabei die Faserfeuchtigkeit von Naturfasern, das Mischungsverhältnis des Harzes und der Aushärtegrad. Außerdem wurde untersucht wie sich Mischungsverhältnis und Aushärtegrad gegenseitig beeinflussen, da die Bestimmung beider Parameter auf den gleichen funktionellen Gruppen beruht.

Als Spektrometer wurden dabei miniaturisierte Spektrometer der NIRONE Reihe verwendet. Diese zeichnen sich durch ein geringes Gewicht und Kosten, sowie simple Handhabung aus. Allerdings haben sie gegenüber klassischen

Prozessspektrometern eine erhöhte Messzeit und schlechtere physikalische Auflösung.

Im Rahmen der Arbeit gelang es für die drei genannten Parameter, Faserfeuchtigkeit, Mischungsverhältnis und Umsatz, Methoden für die Bestimmung der notwendigen Referenzwerte zu etablieren. Für alle drei Parameter konnten Regressionsmodelle zur Vorhersage der gemessenen Werte entwickelt werden. Die Leistungsfähigkeit der miniaturisierten Spektrometer und die Bereite der Anwendungsmöglichkeiten der Nahinfrarot Spektroskopie zum Prozessmonitoring der Verarbeitung von Faser-Kunststoff-Verbundwerkstoff wurde erfolgreich demonstriert.

Abstract

Increasing demands for quality assurance, process stability, and control create the need for efficient capture, processing, and analysis of process- and product-relevant measurements during manufacturing, i.e., inline. This often brings economic and ecological benefits through reduced waste and shorter process times. Which parameters are measurable inline depends on the respective technology. One technology that has been scarcely investigated for inline monitoring in the processing of fiber-reinforced polymer composites but is broadly applicable is near-infrared spectroscopy. It utilizes combination and overtone vibrations of functional groups induced by electromagnetic waves in the range of 750-2500 nm. From the measured spectra, parameters can be determined using partial least squares regression, which correlate with the concentrations of functional groups in the measurement volume.

In this study, application possibilities of near-infrared spectroscopy for monitoring liquid composite molding processes are investigated. Liquid composite molding processes were chosen as an example because the essential process steps related to the resin system can be measured well here. Additionally, it allows the consideration of different but relevant measurement scenarios, such as on the pure resin system, through films, or in closed molds. Inline measurements included the fiber moisture of natural fibers, the resin mixing ratio, and the degree of cure. Furthermore, it was investigated how the mixing ratio and degree of cure influence each other, as the determination of both parameters is based on the same functional groups.

Miniaturized spectrometers from the NIRONE series were used. These are characterized by low weight and cost, as well as simple handling. However, they have increased measurement time and poorer physical resolution compared to classical process spectrometers.

In the course of this work, methods for determining the necessary reference values were established for the three mentioned parameters, moisture content, mixing ratio and degree of cure. Regression models for predicting the measured values were successfully developed for all three parameters. The performance of the

miniaturized spectrometers and the wide application possibilities of near-infrared spectroscopy for process monitoring of fiber-reinforced polymer composites processing were successfully demonstrated.

Table of Contents

Abbreviations, Acronyms and Symbols

Abbreviations:

Abbreviation	Description
aliph.	The atom/functional group is attached to an aliphatic methyl group.
ar.	The atom/functional group is part of an aromatic system or is directly attached to it.
bend.	Bending vibration
PointAvg	Measurements taken by NIRONE spectrometers at one wavelength during one scan are to be averaged.
ScanAvg	NIRONE spectrometers average spectra to obtain one spectrum, which is saved.
Steps	Distance between two measured wavelengths of the NIRONE spectrometer
str.	Stretching vibration

Acronyms:

Acronym	Description
AI	Artificial Intelligence
CAGR	Compound Annual Growth Rate
CFRP	Carbon fiber-reinforced plastics
CV	Cross Validation
DSC	Differential Scanning Calorimetry
FRP	Fiber-reinforced polymer
FTNIR	Fourier-transformed Near Infrared
GFRP	Glass fiber-reinforced plastics
IR	Infrared
LCM	Liquid Composite molding
LV	Lateral Variable
MEMS	Micro Electronic Mechanical System
MLR	Multiple Linear Regression
NF	Natural Fiber
NIR	Near Infrared
NFRP	Natural fiber-reinforced polymers
NMR	Magnetic Resonance Spectroscopy
PC	Principal Component
PCA	Principal Component Analysis
PCR	Principal Component Regression
PLS	Partial Least Square Regression
XAS	X-ray absorption spectroscopy
XRF	X-ray fluorescence spectroscopy

Acronym	Description
OSC	Orthogonal Signal Correction OSC

Symbols:

Symbol	Unit	Description
A	-	Absorbance
α_0	-	Degree of cure at the beginning of the curing phase
α_{cured}	-	Degree of cure at the end of the curing phase
α_{DSC}	-	Degree of cure determined by DSC
α_{NIR}	-	Degree of cure determined by NIR
$\alpha_{uncured}$	-	Degree of cure at the beginning of the curing phase
c	[m/s]	Speed of Light in vacuum
c_{MC}	[wt%]	Moisture in the NF
D	-	Cook Distance
E	[J]	Energy
$\mathbf{E}$	-	Residual matrix ($n\ x\ m$)
E_v	[J]	Energy of the Equilibrium State of a Molecule
e_i^2	-	Residual of the i-th sample
H_0	[J]	Enthalpy of freshly mixed resin
H_{cured}	[J]	Enthalpy of the cured resin sample
H_{inf}	[J]	Enthalpy of the resin after the infusion
$H_{uncured}$	[J]	Enthalpy at the beginning of the curing phase
h	-	Leverage
$\hbar$	[Js]	Planck constant
I	[a.u.]	Intensity measured by the spectrometer
I_0	[a.u.]	Intensity of a reference spectrum

Symbol	Unit	Description
k	-	Number of Principle Components/Latent Variables
l	-	Number of target values
λ	[nm]	Wavelength
m	-	Number of variables (data points in the spectrum)
m_w	[g]	Weight of the wet sample
m_d	[g]	Weight of the dried sample
n	-	Number of observations (measured spectra)
ν	[s^{-1}]	Frequency
$\tilde{\nu}$	[cm^{-1}]	Wavenumber
$\mathbf{P}$	-	Loading matrix ($k\ x\ m$)
$PRESS$	-	Predicted Residual Sum of Squares
$\mathbf{Q}$	-	Loading matrix of the Y data
r	[m]	Radius
r^2	-	Coefficient of determination
r^2C	-	Coefficient of determination of Calibration
r^2CV	-	Coefficient of determination of Cross Validation
r^2P	-	Coefficient of determination of Prediction
$RMSE$	-	Root mean square error
$RMSEC$	-	Root mean square error of Calibration
$RMSECV$	-	Root mean square error of Cross Validation
$RMSEP$	-	Root mean square error of Prediction
s_R^2	-	Residual variance
s_{LV}^2	-	Variance explained by the LV
s_g^2	-	Total explained variance

Symbol	Unit	Description
$\mathbf{T}$	-	Score matrix of the X data $(n\ x\ k)$
T_g	[°C]	Glass transition temperature
$\mathbf{U}$	-	Score matrix of the Y data
V	[J]	Potential energy
$\mathbf{W}$	-	Weight matrix
$\mathbf{X}$	-	Original matrix $(n\ x\ m)$
$\mathbf{Y}$	-	Target matrix $(n\ x\ l)$
y	-	Target vector
y_i	-	Measured value for the i-th sample
$\hat{y}_i$	-	Predicted value for the i-th sample
$\bar{y}$	-	Mean of the observed target variable y_i

1 Introduction and Motivation

Fiber-reinforced polymer composites (FRPC) have seen increasing interest over the last few decades due to their specific and outstanding properties in terms of excellent lightweight potential, high strength, stiffness, and fatigue resistance, as well as a high degree of freedom in part design. The main market sectors by value using FRP composites are transportation (automotive and railway), construction (e.g., building, civil engineering, etc.), and aerospace industries. The energy, electrical and electronics, and consumer goods industries also share significant market shares. In 2024, the composite market was 13 Mt in volume [1]. Glass fiber-reinforced plastics (GFRP) accounted for the largest share by far, at over 90 %. In contrast, carbon fiber-reinforced plastics （CFRP) only made up 2 % and natural fiber (NF) reinforced plastics (NFRP) 5 % [2]. Considering the matrix material, thermosets are overweight thermoplastic matrix materials, with a market share of approximately 55 % [1]. For the following years, until 2028, a Compound Annual Growth Rate (CAGR) of 3-4 % is forecasted for the composite market. Meanwhile, the proportion (in volume) of manual processes (e.g., hand lay-up spray-up) is decreasing in favor of liquid composite molding processes (LCM, e.g., vacuum assisted resin infusion (VARI), resin transfer molding (RTM)) and continuous processes (e.g., pultrusion, filament winding) [1]. In 2021, LCM processes had a market volume of 8 % [2].

LCM processes are “processes in which a dry fibrous reinforcement is impregnated by a liquid resin inside a sealed cavity” [3]. A pressure gradient achieves the impregnation by driving the resin system into the reinforcement structure. There are different ways of categorizing the different LCM processes [3, 4]. The simplest one is by differentiating them by the driving forces responsible for the impregnation [4]. This results in two types of processes: infusion processes, where a vacuum pressure draws the matrix resin into the preform, and injection processes, where the matrix resin is squeezed by overpressure into a mold to impregnate the preform.

Over the past decades, several process variations have been developed, which can be attributed to either of those mentioned above or as a combined process to both. Table 1 gives an overview of common processes.

Table 1: Overview of common LCM processes.

Acronym	Name	Characteristic
VARI	Vacuum-assisted resin infusion	- One-sided mold - Matrix is drawn into the preform by vacuum pressure
RTM	Resin transfer molding	- rigid mold halves - Matrix is injected by pressure into the mold
RTMLight	Resin transfer molding light	- The upper mold half is semi-rigid - Can deform during injection - Reduced tooling costs, compared to RTM
VARTM	Vacuum-assisted resin transfer molding	- RTM process with supporting vacuum to increase surface quality
CRTM	Compression resin transfer molding	- Reduction of the cavity height after injection to reduce injection time
TERTM	Thermal Expansion Resin Transfer Molding	- Using a foam core that is expanded after injection to increase fiber volume content

The LCM process chain typically starts with preparing the dry textile reinforcement, the so-called preform. This can include simple cutting and stacking of the textile reinforcement. It also involves more elaborate processing steps such as stitching auxiliary threats or using polymeric binders to fix the textile reinforcement in a specific shape, which is beneficial for later process steps. Subsequently, the preform, which may consist of several parts, is placed in the mold.

From this point on, VARI and RTM differ, especially regarding saturation method and tooling. The VARI process is described here in more detail, as it is used mainly in this thesis. In VARI process the preform is usually covered with a release ply; if necessary, a flow aid and extra channels for the resin flow are placed. Afterward, inlet and outlet points are installed, and a flexible vacuum film covers it to seal it. By applying a vacuum, the preform is evacuated and transversely compacted. The thermoset resin system is mixed and degassed. The applied vacuum drives the resin system from a reservoir into the setup to infuse the preform. The constituents of the resin system start crosslinking, resulting in a solidification, which is referred to as curing. The curing can occur at room temperature or elevated temperatures, depending on the curing characteristics of the resin system. When solidification has reached an adequate state, the composite part is demolded. The release ply and all auxiliary materials are removed. As a final step, edges can be trimmed, or a coating can be applied.

Besides the expected growth of the composite market, other factors make further developments of LCM processes necessary. Stricter regulations regarding staff security necessitate to reduce the risk of employee contamination, e.g., due to errors in process management. In addition, reducing the ecological footprint is also becoming increasingly important. Reducing processing waste and rejects, as well as measures to increase energy efficiency, are beneficial not only from an environmental but also from an economic point of view.

Advancement and future development of process automation are pivotal to achieving the predicted CAGR growth, improving process functioning, and reducing rejects. To support this trend, efficient inline monitoring techniques are needed for better process understanding, quality assurance, and automated process control to shorten lead times and reduce scrap rates.

Various possible technologies for inline monitoring LCM processes, such as ultrasonic [5, 6], dielectric analysis [7, 8], or direct current [9, 10], are already in the focus of the scientific community [11]. Another promising technology, already in use for inline monitoring purposes in many other regulated industries, such as food [12, 13] and pharmacy [14, 15], is Near Infrared (NIR) Spectroscopy. However, the only process in the composite sector in which the application of NIR spectroscopy has

been under research in the past years is the prepreg production through the solvent route. Among other parameters, the solvent and resin content were determined directly during the continuing process [16–18]. However, these parameters are primarily relevant for prepreg production and not for composite processing in general. Over the last three years, a successful integration of NIR spectroscopy to determine the gel time and areal weight of the resin in a prepreg production line using the hot melt process was achieved as part of the "Spectroscopic Analysis of Prepregs" project.

1.1 Process Monitoring with NIR Spectroscopy

Similar to most other types of spectroscopy, NIR spectroscopy is named after the wavelength range of electromagnetic radiation using it. The NIR range reaches from 750 to 2500 nm. NIR, therefore, utilizes overtones and combination vibrations of the measured functional groups. Methylene, amine, and hydroxy groups are most present in NIR spectra [19]. Based on the functional groups, NIR spectroscopy can be used to make quantitative statements about changes in the concentration of the corresponding functional groups in the measurement volume. Compared to other monitoring techniques, NIR can determine a wide range of parameters, as many parameters are connected in one way or another to the concentration of a functional group. NIR is especially suitable for process monitoring as the measuring signal can be conducted via optical fibers directly from the process to the spectrometer (inline measurement). This allows the spectrometer to be placed outside demanding or hazardous environments, safe in a control cabinet. In addition, no electrical component needs to be designed for use in an ex-zone. However, corresponding NIR spectrometers for process monitoring are often designed accordingly. Furthermore, NIR requires no sample preparation and is non-destructive, which is mandatory for inline measurement. It is fast, has a measuring time shorter than 1 s, and can measure contactless if required. This is essential for some applications, such as the prepreg process mentioned above.

Alike many other technologies for process monitoring, NIR spectroscopy requires calibration. To do so, the measured NIR spectra are assigned to corresponding reference values, which are determined by traditional methods. A model is obtained using partial least square regression (PLS) that can predict the value according to

the reference value from a spectrum with unknown properties. After establishing a PLS model, process information can be obtained more or less in real-time, which enables direct intervention if necessary. Or the parameter can be used in an automated process control.

In recent years, miniaturized NIR spectrometers have been established. As the name suggests, they are smaller, allowing for more flexible handling and measuring than traditional setups. The smaller size does, however, result in a lack of resolution and increased measuring time. As trade of, the reduction in size results in a loss of resolution and increased measuring time, which in turn is balanced by significantly lower cost, often an order of magnitude or more, and reduced power consumption.

1.2 Scope and Objectives of this Work

The present work aims to demonstrate the possibilities of NIR spectroscopy for inline monitoring along the process chain of thermoset-based FRPC. The used spectrometers are recently developed miniaturized spectrometers from the NIRONE series. This allows statements about the general application possibilities of NIR spectroscopy and the suitability of miniaturized spectrometers for process monitoring in the FRP composite sector. The advantages and disadvantages of their use are discussed. Different measuring environments, e.g. directly on the neat resin system or in a closed mold, are chosen to cover a wide range of possible applications.

The LCM processes were chosen as an example for this work to create a basis for further investigations of a wide range of conceivable applications and, simultaneously, to concentrate on a few processes. In general, LCM processes cover most of the relevant process steps for processing the resin: mixing the resin, impregnating the reinforcing structure, and curing. In addition, measurements can be carried out on the reinforcement structure in advance. The monitored parameters are the moisture content of NF (c_{MC}), the mixing ratio of the resin system, and the degree of cure. Corresponding NIR measurements and suitable reference measurements were carried out for all applications. On this basis, PLS models are developed to enable process monitoring. These are ultimately also the basis for

judging the suitability of NIR spectroscopy for process monitoring in the FRP area in general and the miniaturized-spectrometers used in particular.

1.3 Outline of the Thesis

In **Chapter 2**, the theoretical background of the work is elaborated. This includes the fundamentals of NIR spectroscopy, different spectrometer concepts, and the mathematical principles necessary to convert an inline measured spectrum into a quantitative measurement of a parameter. Furthermore, the miniaturized NIR spectrometers used in this study are introduced. Additionally, the state of the art in the application of NIR spectroscopy for the processing of composite materials is presented. The overall focus is on the practical presentation of the knowledge relevant to this work rather than on conveying deep theoretical backgrounds. Suitable textbooks for a deeper understanding of the theoretical backgrounds are recommended at the appropriate sections.

In **Chapter 3**, infrared (IR) and NIR spectra are measured with an FTNIR spectrometer, and different NIRONE spectrometers are compared. The absorbance peaks are assigned to their functional groups, and, where possible, the peaks in the NIR are also linked to their fundamental vibrations in the IR. In addition, the difference in the resolution and general structure of the spectra between a full-scale process spectrometer (FTNIR spectrometer) and the NIRONE spectrometer becomes apparent.

The **Chapters 4** to **7** form the core of the work and deal with the measurement of different process parameters in LCM processes. Figure 1 assigns the chapters to the respective process steps.

In **Chapter 4**, the natural fibers (NF) moisture content in the RTM process is determined using NIR spectroscopy. First, a PLS for a NF textile is created based on the measured spectra. The model's transferability to other textiles is then tested. This allows conclusions to be drawn about how the spectra of the NIRONE spectrometers react to changes in the substrate. On the other hand, it answers the very practical question, especially for research institutions, whether a separate

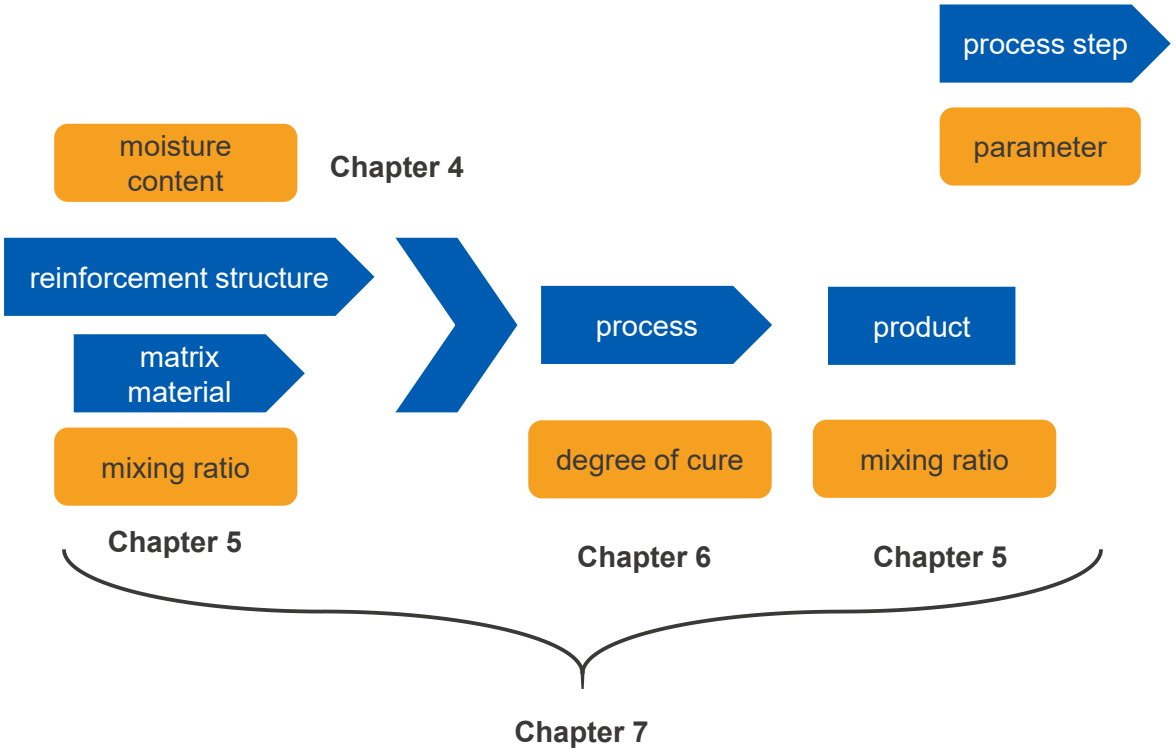

Figure 1: Graphical representation of the process-technical connections between the chapters.

calibration is necessary for each NF textile or whether it makes sense to test the transferability of a PLS model to the respective NF.

Chapter 5 deals with the mixing ratio of resin and hardener. The mixing ratio of an epoxy/amine resin is determined in the VARI and an aluminum cup. The aluminum cup represents the general application as an example. The mixing ratio is determined for both fresh and cured resin.

In **Chapter 6**, the degree of curing is monitored inline in a VARI process. In addition to the NIR measurements, a suitable reference methodology is established. Isothermal Differential Scanning Calorimetry (DSC) measurements are used as the reference method. Preliminary investigations ensure an isothermal experimental procedure. During the actual measurements, spectra are recorded with all four commercially available NIRONE spectrometers. PLS models are developed and compared for all spectrometers. The results demonstrate the potential for monitoring the degree of curing using NIR spectroscopy and highlight the impact of the utilized

wavelength range on the results, emphasizing the importance of selecting the appropriate wavelength range.

In **Chapter 7**, the influence of deviating mixing ratios on the determined degree of curing is examined. Since the determination of both parameters ultimately relies on the measurement of the same functional groups, there is an interaction between them. The impact of these variations on the measurement data from all four commercially available NIRONE spectrometers is discussed, and a proposed approach is presented.

Chapter 8 summarizes the results and discusses the potential for applying NIR spectroscopy in general and miniaturized-spectrometers in particular in composite processing.

2 Fundamentals and Advances in Near Infrared Spectroscopy

Today's scientific advances and findings would be inconceivable without spectroscopy. Spectroscopy is defined as:

> “study of the absorption and emission of light and other radiation by matter, as related to the dependence of these processes on the wavelength of the radiation.” [20]

Radiations are categorized by their wavelength ranges depending on the interaction between matter and radiation (see Figure 2). Each wavelength range interacts differently with matter; therefore, various spectroscopy methods have been developed, each of them providing different information about the investigated matter. For example, in the X-ray range (approximately 0.01 to 10 nm), X-ray fluorescence (XRF) and X-ray absorption spectroscopy (XAS) provide information about elemental composition (XRF) and the electronic and/or local geometric structure of matter (XAS). Substance identification and concentration determination are widely achieved using UV/Vis spectroscopy in the range of 200 to 780 nm. In the infrared range (approximately 780 to 25000 nm), NIR and IR spectroscopy provide information about molecular structures by analyzing functional groups and chemical bonds. At longer wavelengths microwave spectroscopy (approximately 1 mm to 1 m) provides information, among others, about bond lengths and angles.

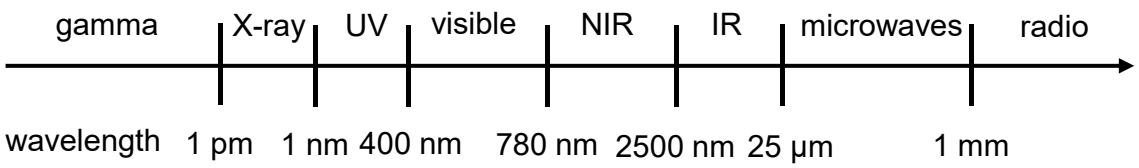

Figure 2: Spectrum of the electromagnetic radiation.

The application areas are as varied as the information supplied, from strict laboratory applications to astronomy and inline measurements under difficult process conditions. NIR (780 to 2500 nm) is especially interesting for monitoring composite manufacturing processes, as it is fast, non-destructive, requires no sample preparation, and can provide information related to concentration changes in the measuring volume.

2.1 Physical Principle of NIR spectroscopy

Electromagnetic radiation in the IR range is known for inducing fundamental molecule vibrations, which are directly observed as peaks in the IR spectra. These peaks serve as molecular fingerprints, identifying the presence of specific functional groups. In the NIR range, overtone and combination vibrations are activated, which, while subtler, correlate with the peaks observed in the IR spectra. The radiation can provide the energy E, required for the molecular vibrations and electron transitions:

$$E = \hbar\frac{c}{\lambda} = \hbar\nu \tag{1}$$

Where $\hbar$ is the Planck constant (6.626*10^{-34} Js), c is the speed of light, and ν is the frequency. The context for the frequency ν is given, as it is common to use it instead of using a higher wavelength. Equation (1) follows that the shorter the wavelength, the higher the energy provided by the radiation.

When an electromagnetic wave interacts with matter, it can transfer energy, leading to the absorption of the wave's energy by the matter. Yet, this energy exchange is subject to very precise conditions, making it possible for substances to be transparent over broad regions of the electromagnetic spectrum, indicating no interaction between the radiation and the matter. Conversely, the material may be entirely or partly opaque in other spectrum regions. The process where radiant energy is absorbed is known as absorption. To explain the absorption and associated processes, atoms or molecules are conceptualized using the Bohr model (see Figure 3). In the Bohr model, every atom has a positively charged nucleus surrounded by negatively charged electrons that orbit around it. The orbits of electrons within an atom are characterized by certain energy levels that can be quantified using quantum numbers, which are either integer or half-integer values.

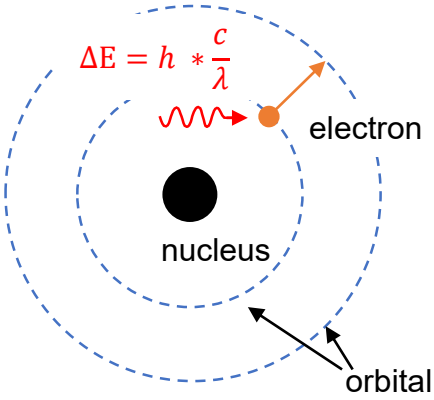

Figure 3: Diagram of the electron orbit transition according to Bohr.

When an electron switches between orbits, as shown in Figure 3, it either absorbs or releases energy. These transitions occur via defined quantum jumps following specific rules. Consequently, the energy difference between two orbits can be expressed as:

$$\Delta E = E_1 - E_2 \tag{2}$$

Since the energy required for the transition ΔE must come from electromagnetic radiation, the following also applies:

$$\Delta E = E_1 - E_2 = \hbar \frac{c}{\lambda} \tag{3}$$

This means an atom can only absorb electromagnetic radiation of a certain wavelength. If the electron falls back to its low level, the corresponding radiation is emitted.

In molecules, the atoms are held together at specific distances due to the interactions among the electrons in their outermost orbits. This interaction is crucial because it leads to different types of energy, such as vibrational and rotational energies. When molecules absorb energy, the atoms within are induced to vibrate around their equilibrium state. This vibrational energy can only adopt specific discrete, quantized values. If the supplied power is insufficient, it merely excites the molecules to rotate [21].

That molecules can only absorb discrete energies, results in the differentiation between IR and NIR. In the IR range, the molecule is excited from its ground state ($n = 0$) to $n = 1$ (see Figure 4). Its potential energy V is increased, and the distance r between the atoms can vary more. In the NIR range, the molecule is excited to higher states (n = 2, 3, 4…). The vibration of the molecules can be described as an oscillator; the regarding derivation can be found in the literature [19]. Due to quantum mechanics, these transitions (n=0 → $n \geq 2$) occur less frequently, leading to weaker absorption. Another quantomechanical effect is that the interaction of infrared radiation with a vibrating molecule is only possible if the molecule is a dipole. As a result of these restrictions, in NIR spectra, peaks are much broader but weaker than in IR spectra. Further, functional groups like methyl, hydroxy, or amine are very present, as the hydrogen-hetero atom bonding is a strong dipole.

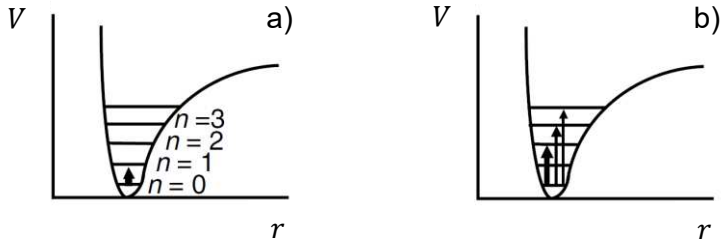

Figure 4: Energy absorption in the IR (a) and NIR (b) range[21].

2.2 Spectrometer Technologies

To measure an NIR spectrum, the sample must first be excited by absorbing specific wavelengths. The necessary electromagnetic radiation, “light”, comes from a light source. Tungsten halogen lamps are commonly used as light sources for NIR and IR spectroscopy due to their broad and continuous emission spectrum covering the visible and NIR regions. Other light sources like Light Emitting Diodes (LEDs) suffer much smaller emission spectra or shorter life spans (Xenon lamps) but are also used in special cases. In addition to selecting the appropriate light source, the correct measurement mode, probe, and spectrometer must be chosen for NIR measurements.

2.2.1 Measuring Mode

NIR and IR measurements can be conducted in three modes: transmission, reflection, and transflection (see Figure 5). In the transmission method, the light beam fully penetrates the sample. The excited light is detected at the other side of the sample. This technique is primarily employed for liquids or polymer melts. In contrast, the reflection method involves the light beam being reflected at the surface or just below it, followed by detection. This approach is predominantly used for solid materials, where complete penetration by light is not feasible. Transflection merges the previously described methodologies. In this technique, the light beam traverses the entire thickness of the sample, is reflected by a mirror, and passes through the sample again. Hence, both the transmitted and diffusely reflected light components are detected. This can be particularly beneficial for very thin samples with weak absorption lines, as the absorption can be enhanced due to the light's double passage through the sample [19].

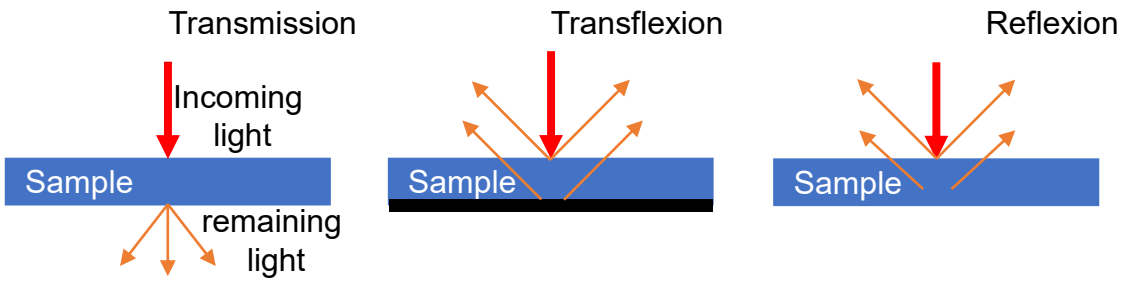

Figure 5: Measuring mode in NIR spectroscopy.

2.2.2 Measuring Probe

During the transport of captured light, NIR technology demonstrates one of its significant advantages over IR spectroscopy. In spectrometers used for laboratory applications (IR and NIR), the sample is placed and measured within the spectrometer. However, in inline measurements, positioning the spectrometer within the process is often not feasible or associated with considerable effort and risks. Depending on the process, environmental conditions such as pressure and temperature can prevail, making on-site operation impossible. Similarly, explosion protection can pose a challenging issue. In NIR spectroscopy, measurement optics that utilize optical fibers (glass fibers) can be employed, allowing the spectrometer to be positioned outside the process, for instance, in a control box, at a suitable

location. Glass fibers are transmissible in the NIR range. But their transmissibility drops around 2500 nm, making them useless in the IR range. For the IR, range chalcogenides can be used, but so far, their application is quite limited due to their brittleness and limited length. Measurement optics can be customized to meet specific requirements. Transmission, reflection, or transflexion can be implemented depending on the requirements. The light source(s) can be placed either directly in the measuring head or, like the spectrometer, outside. In the latter case, the light is directed to the measuring head via optical fibers. To capture more light, collecting lenses can be used to focus the light onto the optical fiber (see Figure 6). This measuring head for reflection measurements consists of four halogen bulbs and centrally a collecting lens. In addition to a stronger signal, collecting lenses reduce scattering effects caused by the sample's surface, as signals from more scattering centers are incorporated into the spectrum [19].

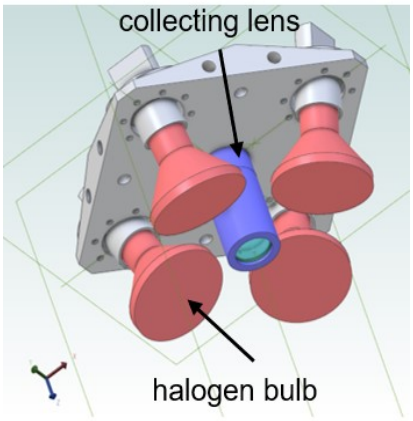

Figure 6: NIR measuring probe used for measuring gel time in the prepreg production (provided by i-Red Infrarotsysteme GmbH).

2.2.3 NIR Spectrometer

Light is converted into information (spectra) in laboratory and inline-capable spectrometers. This conversion is typically achieved using suitable photon detectors based on InGaAs, PbS, or InAs [19]. The detectors are based on photoelectric effects, transforming light into a current. The unit of measurement is the (light) intensity. However, when the polychromatic light from the sample hits the detector unfiltered, only a single measurement value containing information on all

wavelengths is obtained. Therefore it is only of limited informative value. To address this issue, there are two fundamentally different approaches:

- Separating the polychromatic light into monochromatic light and measuring each wavelength individually
- Measuring an interferogram of the polychromatic light and calculating the spectrum using Fourier Transformation.

Various technological approaches exist to separate polychromatic light, such as linear variable filters or Fabry-Pérot interferometers.

The **Fabry-Perot interferometer** consists of two semi-transparent mirrors, which, due to their high reflectivity, together constitute an optical resonator (see Figure 7) [22]. An optical resonator is a structure in which light waves are trapped through multiple reflections between reflective surfaces, allowing standing wave patterns or resonances to occur. Narrow transmission peaks are formed upon exiting the resonator due to constructive interferences when the resonance conditions are met. The peaks appear as circles on the detector. Other wavelength ranges occurring between the circles are eliminated mainly through destructive interferences. By altering the distance between the mirrors, the condition for interference can be changed, and thus, the wavelength of the transmission peaks can be changed.

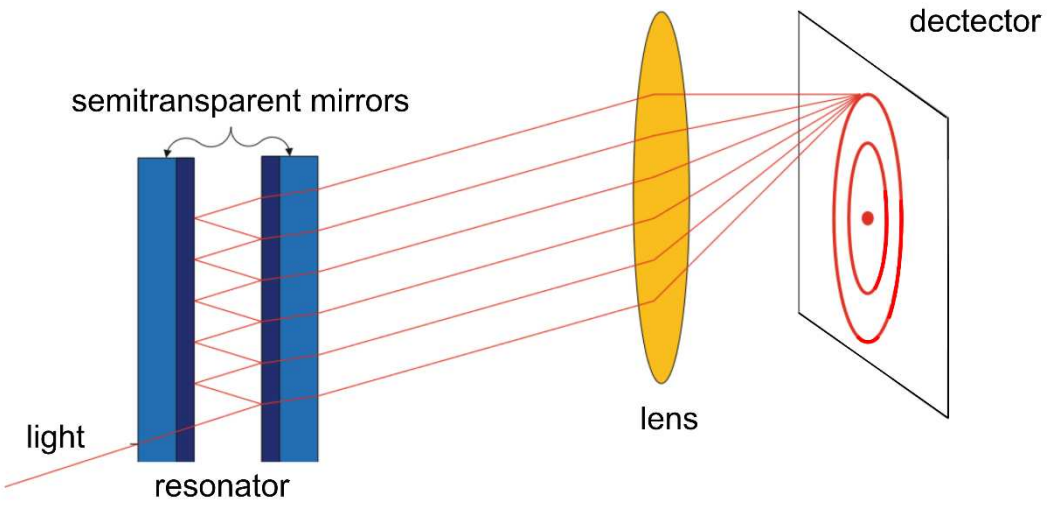

Figure 7: Concept of Fabry-Pérot Interferometer[22].

An individual value is measured for each discrete point within the spectrum to measure a spectrum over the full wavelength range of the detector.

Instead of measuring intensities of the individual wavelengths, a time-dependent interferogram contains information about all wavelengths. Typically, the Michelson interferometer is used to measure the interferogram. The light beam coming from the sample is directed towards both mirrors using a beam splitter, from which each partial beam is reflected to the beam splitter (see Figure 8). The distance traveled by the light in this process is referred to as the interferometer arm. The partial beams superimpose as they proceed toward the detector, resulting in interference. This interference depends on the position of the movable mirror and can be either constructive or destructive. When employing polychromatic light, as typically used in IR and NIR spectroscopy, each wavelength exhibits this phenomenon individually. The signal intensities of all wavelengths, depending on the mirror position, form the interferogram. For practical and measurement technical reasons, the movable mirror is not positioned statically to capture the radiation intensity at the output of the interferometer. Instead, the mirror is moved continuously at a constant speed, leading to the registered radiation flux being dependent on time. This implies that a spectrum represents the signal intensities as a function of frequency or wavenumber, whereas the interferogram displays intensities as a function of time. Another difference is that in the interferogram, each data point contains information across

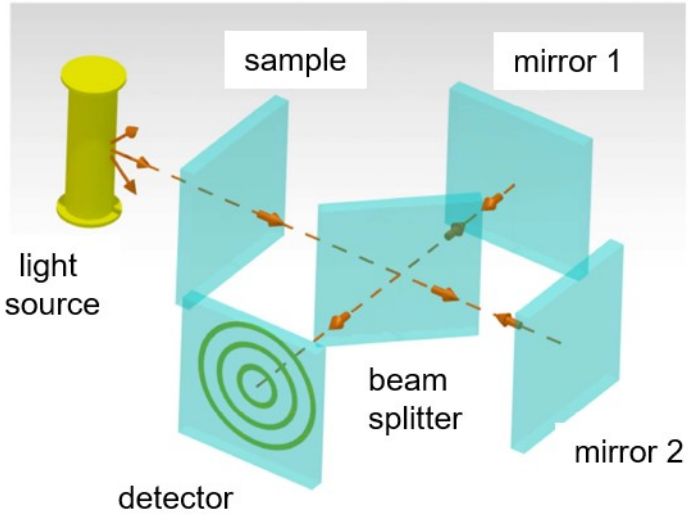

Figure 8: Concept of a FTNIR spectrometer[23].

the entire spectrum. Through Fourier Transformation, the interferogram is converted into a conventional spectrum.

2.2.4 Portable Spectrometers

Conventional NIR spectrometers are relatively large, immobile devices, whether for inline measurements or laboratory applications. However, due to the demand for mobile NIR spectrometers, various small and portable spectrometers have been developed recently. Zhu lists a total of 24 market-available portable spectrometers in 2022 [23]. Portable NIR spectrometers differ from full-sized instruments in their size and weight. There is no fixed limit in size or weight that a spectrometer is still called portable; Zhu limits his review to spectrometers lighter than 1600 g [23]. The literature primarily discusses their application in the food industry. This includes the determination of quantitative parameters such as the fat content of fish [24] or meat [25], or the firmness of tomatoes [26] or apples [27]. But also the identification of origin or individual components, for example, if food contains specific allergens [28] or in textiles, the fiber material composition [29] is done using portable spectrometers. Besides applications in the food and textile industry, among others in pharma (drug concentration [30] and product authenticity [31]) and forensic investigation (authenticity assessment of banknotes [32]) have also been demonstrated.

The miniaturization and weight reduction of the spectrometers are enabled by simplifying the spectroscopic components, electrical circuits, etc. This often involves the use of micro-electro-mechanical systems (MEMS), as in the case of the NIRONE spectrometers [33], or micro-opto-electro-mechanical systems (MOEMS), such as the MircoNIR 1700ES [34]. The reduction in size and weight comes at the cost of reduced resolution and measurement range, extended measurement times, and a poorer signal-to-noise ratio. For instance, the NeoSpectra Micro (Si-Ware Systems, California, United States of America), a portable FTNIR spectrometer, only has a resolution of 16 cm^{-1}, whereas full-sized NIR spectrometers can achieve 1.5 cm^{-1} [35]. The measurement ranges often cover only a few hundred nanometers[23]. The signal-to-noise ratio varies significantly and correlates with the measurement time, but for most portable spectrometers, it is well below the >10,000 typically stated for full-sized spectrometers [23, 35].

Despite the significantly worse performance metrics in some cases, several comparative studies have concluded that portable spectrometers can provide sufficiently accurate results in suitable applications, even when compared to full-sized spectrometers [36, 37].

2.2.4.1 NIRONE Spectrometers

Miniaturized-spectrometers of the NIRONE series (Spectral Engines GmbH, 97 Steinbach, Germany) are used in the frame of this work. As mentioned above they are based on a MEMS Fabry-Perot Interferometer. Each spectrometer covers a different wavelength range of the NIR range (see Table 2). The length of the covered wavelength range depends on the detector of the spectrometer. Compared to an FTNIR spectrometer, the spectrum is not measured at once. Instead, at each single measured wavelength, the intensity is measured. Several measurements are taken and averaged at each wavelength before going to the next one. In this way, after measuring all wavelengths, one spectrum is obtained. The number of measurements taken is referred to as "*PointAvg*" later on. Several of these spectra are then averaged to obtain one spectrum that is saved. The number of spectra used for averaging is referred as "*ScanAvg*". The distance between each two measured wavelengths is referred to as "*Steps*". This allows to find a good compromise between short measuring time, as changing the measured wavelength requires additional time, and a not too large delay between measuring the left and the right side of the spectra.

Table 2: Wavelength range of the NIRONE spectrometers.

NIRONE spectrometer	Wavelength range [nm]
S1.7	1350-1650
S2.0	1550-1950
S2.2	1750-2150
S2.5	2000-2450

2.3 Graphical Representation of NIR Spectra

NIR spectrometers measure so-called energy spectra, representing just the intensity at the regarding wavelength. However, absorption spectra are better suited for graphical visualization. The absorbance is calculated by using (4):

$$A = -log(I/I_0) \tag{4}$$

Here, A denotes the absorbance, I the measured intensity spectra, and I_0 the reference spectrum. Presenting absorbance spectra is common in the community and is a specific requirement of some journals [38]. In absorbance spectra, peak positions and differences between spectra can be seen much better (see Figure 9). The energy spectra (see Figure 9a) differ only lightly, even in the region around 1920 nm, in which the absorbance spectra show clear peaks. The absorbance spectra (see Figure 9b) show apparent differences in the peak at 1920 nm. However, it can be hard to identify how strong spectra differ; for example, it is difficult to tell if the black or red spectrum has a higher peak. After an off-set correction (see Figure 9c), this is easily possible. Now, it is evident that the black spectrum has a

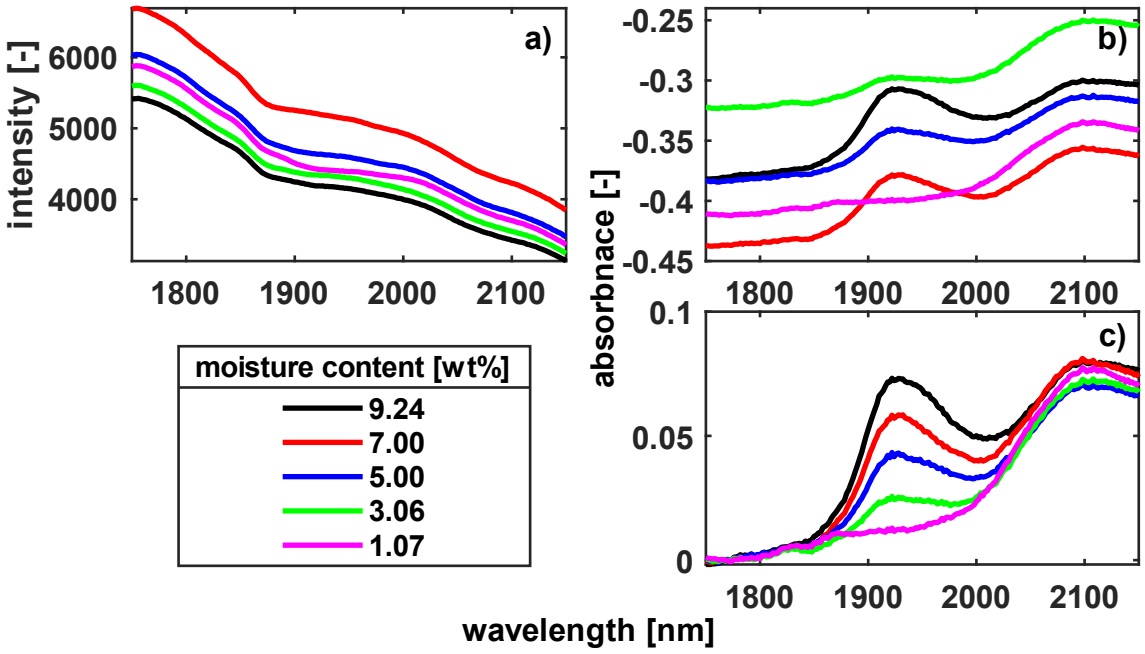

Figure 9: Energy spectra (a), absorbance spectra (b) and off-set corrected absorbance spectra (c) of natural fibers with different levels of moisture content.

bigger peak than the red one. Offset correction subtracts a constant value from the entire dataset to shift the baseline towards zero. As the constant value, the average of all spectra over a small wavelength range, unaffected by the observed phenomena, is typically used.

All presented spectra in this work use spectra of a metal plate as background spectra.

2.4 Multivariate data analysis of NIR spectra

Spectra must be evaluated regardless of the wavelength range to be used. The evaluation should be done automatically if they are to be used for process control. The presence or absence of certain absorption peaks is sufficient for qualitative statements.

However, this is insufficient for quantitative statements about a required measured value. The most commonly used approach is integration and internal normalization with a reference peak of the peaks, e.g., in IR spectroscopy or nuclear magnetic resonance (NMR) spectroscopy. To make statements about the progress of a reaction, the area of the peak obtained is then set in relation to the original area of the peak at the start of the reaction.

With NIR spectra, especially with inline measurements, this simple approach often reaches its limits. Although it is used in the literature for laboratory measurements, agreeing on a consistent and readily reproducible procedure is impossible. The discussion begins with the choice of the reference peak for defined reactions, e.g., the curing of epoxy/amine systems. Cholake commented on this discussion with "Extensive literature[20,24,32] is available suggesting various reference peaks with and without explanations." [39]. Generally, a peak not involved in chemical reactions is used as a reference peak. In epoxy/amine systems, this is typically a phenyl peak [40, 41]. However, as phenyl rings show three absorption peaks in the NIR range, a decision on which one is used must be made. Referencing the area of a changing peak to a reference peak is intended to compensate for concentration changes in the measured volume that are not caused by chemical reactions, e.g., shrinkage.

This simple approach is not used for inline NIR measurements for two reasons. First, peaks overlap strongly in the NIR range, making setting the correct integration limits

difficult. The second, more important reason is the more significant interference, such as dust, vibration, or bubble formation, in ongoing production compared to laboratory measurements. These can strongly influence the spectra, even though the spectra still contain the desired information.

Instead, the spectra are evaluated using multivariate data analysis methods to obtain quantitative statements about the values sought. Multivariate means that the measured value sought depends on several variables, in contrast to univariate analysis, in which the measured value sought depends on only one variable. Spectra provide a large number of variables; each individual measured wavelength represents a variable. Due to interference or process fluctuations, not all of these variables behave similarly over time. Therefore, it is insufficient to evaluate only the change in a representative wavelength. Instead, multivariate data analysis is used to derive the most probable measured value based on the spectrum and a previously created calibration model. Suitable preprocessing is sought to pretreat the spectra before creating the calibration model. Preprocessing includes selecting an appropriate wavelength range, deciding on using a reference spectrum, and applying other so-called chemometric methods. Wavelength ranges that negatively influence the model are usually removed. Not every wavelength contributes positively to a calibration model. A good example are water peaks, which are contained in many samples and change fast due to ambient conditions but often have nothing to do with the measured value sought. Applying chemometric methods aims to improve the influence of the measured value sought while reducing disturbing effects. Chemometrics is defined as:

> “the chemical discipline that uses mathematical and statistical methods, (a) to design or select optimal measurement procedures and experiments, and (b) to provide maximum chemical information by analyzing chemical data.” [42]

Frequently used methods for spectra are derivatives, smoothing, and mean centering.

The calibration model is then calculated using a multivariate regression method based on the spectra and the corresponding reference data. Multivariate regression methods include multiple linear regression (MLR), Principle Component Regression

(PCR), and PLS. The correct abbreviation for Partial Least Square Regression would be PLSR, but PLS has become established in the literature, which is why PLS is also used in this thesis. Nowadays, PLS is widely used to evaluate spectra as it has several advantages over the other methods (see Section 2.4.2).

Considering that each NIR spectrum consists of many data points and each calibration model is based on several spectra, the question of using artificial intelligence (AI) inevitably arises nowadays. Depending on the definition, PLS can already be seen as a method of AI, even if it has been used for much longer. Newer methods, such as e.g. neural networks, can also calibrate NIR data. In the foreseeable future, PLS will continue to predominate in the field of process monitoring:

> "Neural networks have not yet shown any advantage over PLS in our observations. In addition, the high complexity of these models makes it difficult to find the cause of incorrect output values. This is why we do not yet use neural networks and similar approaches in practice, even though we repeatedly test their possibilities on data sets".
>
> *Wolfgang Märzinger, CEO i-Red Infrarotsysteme GmbH, translated.*

Since this work focuses on applying NIR spectroscopy in the field of LCM processes and not developing data evaluation tools, the proven PLS is used.

In addition to determining quantitative measured values, NIR spectroscopy can also be used for classification, for example, to determine the manufacturer of theoretically identical resin components [43]. NIR spectra are usually classified by Principle Component Analysis (PCA). In addition to classification to assign samples with non-quantitative properties, PCA can also be of interest in the run-up to a PLS.

2.4.1 Principle Component Analysis (PCA)

PCA can be used to check how well the samples fit together, whether the class formation is apparent (intentional or unintentional, depending on how the data set is obtained), or whether the expected trends are present.

From a mathematical point of view, this is an eigenvalue problem, i.e., calculating a matrix's eigenvalues and eigenvectors. However, different names have become established in other disciplines, including PCA (statistics), factor analysis (chemistry, psychology), or Karhunen-Loeve transformation (signal processing) [44].

Many good textbooks, whether in German [45, 46] or English [42, 47, 48], explain PCA in detail. The following does not, therefore, provide a comprehensive explanation of PCA. Instead, it focuses on applying PCA to NIR spectra and the pitfalls that arise.

A spectrum does not consist of a line, as in the graphical representation, but of individual data points. Each measured wavelength represents a separate variable (m). Several samples (objects) n are measured in advance for a PLS. These can be combined into a data matrix $\mathbf{X}$ with n objects and m variables ($n \times m$).

Given a large number of variables, it is impossible to recognize patterns, and this can also be difficult to do in the graphical representation, especially when looking at energy spectra. PCA offers the possibility of obtaining essential information through simplification and information reduction. The simplification is attractive because, for example, all wavelengths in the area of a peak follow a similar trend. This means that several variables (wavelengths) describe the same information.

The simplification is achieved by describing $\mathbf{X}$ with as few new, so-called latent variables as possible. In the case of PCA, these latent variables are called Principle Components (PC).

The procedure for PCA can be divided into the following steps:

1. **Prepare data:** First, the data must be prepared. This often involves centering the data by subtracting the mean value of the corresponding dimension from each data point. For spectra, W. Kessler expressly recommends starting with the original energy spectra and only centering them if necessary. The often recommended data scaling is also not advisable for spectra, as wavelength ranges without relevant information significantly influence the PCA [44].
2. **Calculate the covariance matrix:** The covariance matrix of the centered data is calculated. The covariance matrix is a square array that indicates the covariance between each pair of dimensions in the dataset. The diagonal contains the variances of each dimension.

3. **Calculate eigenvalues and eigenvectors:** Next, calculate the eigenvalues and eigenvectors of the covariance matrix. The eigenvectors of this matrix show the directions of the principal axes of the data set, and the corresponding eigenvalues indicate the variance of the data along these axes. The eigenvalues and eigenvectors can be calculated using various numerical methods.
4. **Sorting eigenvalues and determining the PCs:** The eigenvalues (and the corresponding eigenvectors) are sorted in descending order. The largest eigenvalue corresponds to the maximum variance in the data set, and the corresponding eigenvector shows the direction of this maximum variance. This eigenvector is the first principal component (PC1). The other principal components can be found similarly by taking the eigenvectors corresponding to the successive largest eigenvalues, where each subsequent principal component is orthogonal to all previous ones and represents the next highest variance.

Apart from preparing the spectra (point 1), the other points are nowadays usually carried out automatically by computer programs such as the PLS toolbox (Matlab) or Unscrambler.

The interpretation of the PCA results is much more relevant to the application for evaluating the spectra. The general representation of PCA is:

$$\mathbf{X} = \mathbf{T}\mathbf{P}^{\mathbf{T}} + \mathbf{E} \tag{5}$$

With $\mathbf{X}$ as the original matrix, $\mathbf{T}$ as the score matrix, $\mathbf{P}$ as the loading matrix, and $\mathbf{E}$ as the residual matrix. Figure 10 shows the corresponding graphical representation. The matrix $\mathbf{X}$ contains the observed data, with each row representing an observation point (e.g., a measurement or a data set) and each column representing a variable (e.g., individual wavelengths). Suppose there are n observations and m variables (measured wavelengths). In that case, $\mathbf{X}$ has the dimensions $n \times m$. The matrix $\mathbf{T}$ contains the coordinates of the original observations concerning the new axes defined by the principal components. Thus, the elements in $\mathbf{T}$ indicate how intense each observation is concerning each principal component. It can present the observations in the space of principal components. If k is the number of principal components observed, $\mathbf{T}$ has dimensions $n \times k$, where $k \leq m$. $\mathbf{P}^{\mathbf{T}}$ is the transposed charge matrix (or pattern matrix). The columns of $\mathbf{P}$ (before transposition)

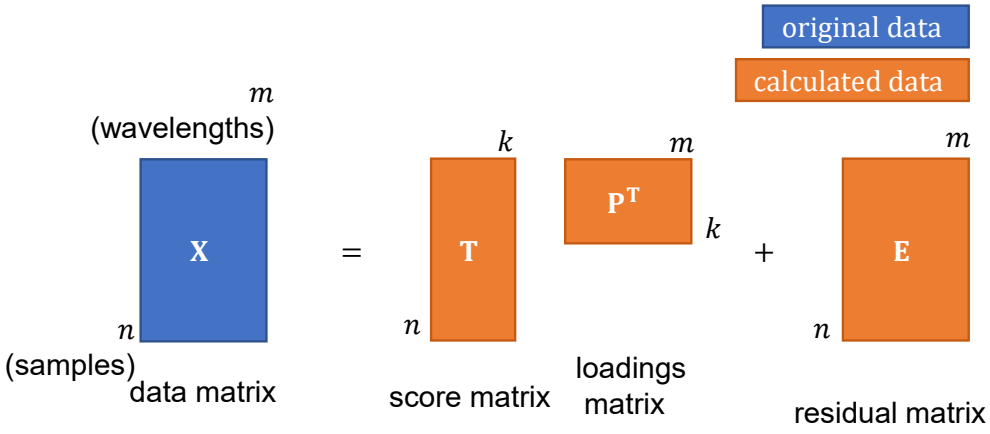

Figure 10: Schematic representation of the relationships in a PCA.

correspond to the eigenvectors of the covariance (or correlation) matrix of $\mathbf{X}$ and describe the directions of the principal components in the original variable space. The transposed form $\mathbf{P^T}$ is used in the decomposition to simplify dimensionality and interpretation. The $\mathbf{P^T}$ (or $\mathbf{P}$) elements indicate how each original variable (for spectra wavelength) contributes to the principal components. This helps to understand which variables contribute most to the variance in the data. $\mathbf{E}$ captures the variance in the data not explained by the selected principal components. This remaining variance may be considered as “noise" or information irrelevant to the analysis. Still, it may also contain important information that has been lost by reducing to the principal components. The size of the elements in $\mathbf{E}$ can be used to assess the quality of the PCA approximation. Small values in $\mathbf{E}$ indicate that the principal components successfully explain a large part of the variance in $\mathbf{X}$. Large values, on the other hand, indicate that a significant part of the data information is not captured. The dimensions of $\mathbf{E}$ correspond to those of the original data matrix $\mathbf{X}$, i.e., $n \times m$ where n is the number of observations and m is the number of variables.

The following section demonstrates the application of PCA. It tests whether spectra from different NF textiles with different moisture content can be used to identify the NF textile. For more detailed explanations of the experimental conditions, see Chapter 5. The focus is on the PCA, and the meaning of the individual matrices is clarified.

The measuring range of the spectrometer used is between 1750 and 2150 nm, measured with a step size of 2 nm. The data set consists of 115 spectra of the

different natural fiber textiles with varying moisture content. In each case, 201 wavelengths were measured. Accordingly, $\mathbf{X}$ has dimensions of 115×201, as well as $\mathbf{E}$. Representative original spectra of the textiles are shown in Figure 11.

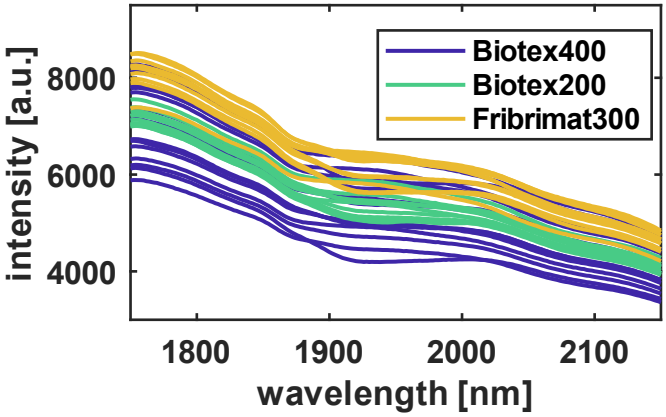

Figure 11: Energy spectra of a natural fiber with different moisture contents between 1.07 and 9.24 wt%.

The intensity of the spectra scatters strongly, at 1750 nm between 5500 and 8500 a.u., and falls slightly over the measured wavelength range. At 2150 nm, the spectra only scatter between 3200 and 5200 nm. The spectra of Biotex400 scatter more than the ones of Biotex200 and Fibrimat300. Between 1900 and 2000 nm, the spectra show differences. This is related to the moisture of the textile. The causing water peak has a maximum at 1920 nm. However, no significant differences between the spectra of the textiles can be observed. As requested by W. Kessler, the uncentered spectra are initially used for the PCA [44]. In PCA, the first principal component, PC1, is plotted against the second principal component, PC2, PC3 against PC4, etc., to identify correlations between the principle components. In this case, 99.9 % of the variance is already explained by PC1. PC2 accounts for the remaining 0.1 %. It is, therefore, very likely that PC2 only contains noise, which is why only PC1 is considered initially. In the case of only one PC, $\mathbf{T}$ has the dimensions 66×1, while $\mathbf{P}^{\mathbf{T}}$ has the dimensions 1×201. Since the usual way of displaying the scores (PC1 vs. PC2) is impossible, the scores of each object (sample) are presented in Figure 12a). The scores for all NF textiles scatter between 6 and $10 \cdot 10^4$ and show no correlation. They do not have any differences regarding the NF textile. For a better understanding of the dataset it is advantageous to understand which parameter is described by PC1, if possible. Therefore, the

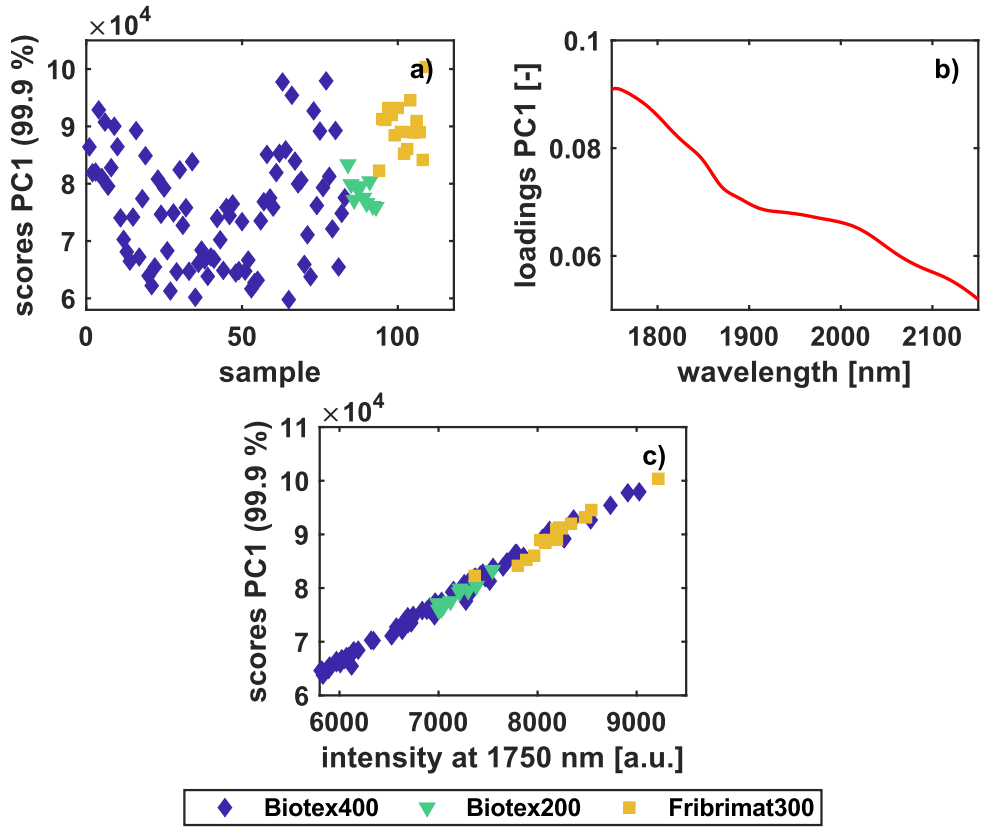

Figure 12: Scores of PC1 of each sample (a) the loadings of PC1 over the measured wavelength range (b) and) and the scores over the intensity at 1750 nm of each spectrum (c).

loadings are presented in Figure 12b), as they can provide information about the influence of variables (wavelength) on the PCA. Loadings close to 1 indicate a significant variance and, thus, possibly relevant changes in the respective wavelength. Values close to 0, on the other hand, indicate a low variance in the respective wavelength. The loadings of PC1 fall with increasing wavelength from 0.09 to 0.05. Accordingly, no wavelength considerably influences the variance, but all have a certain proportion. Overall, the loading plot looks very similar to the measured spectra. That all wavelengths add in a similar way to PC1 suggests that PC1 describes the variance in intensity. The plot of the scores of PC1 versus the intensity at 1750 nm confirms this assumption (see Figure 12c). The score of PC1 increases linearly with the intensity of the spectrum. Since PC1 does not contain the sought information and spectral differences between the NF textiles, it is worth looking at PC2, even if the remaining variance of 0.1 % is very low (see Figure 13). The PC1 vs PC2 (Figure 13a)) displays what is already known, Biotex200 and

Fribrimat300 have a higher intensity (compared to Figure 11 and Figure 12). However, in PC2, the NF textiles show no difference that would allow for textile identification. The loadings of PC2 (Figure 13b) show the dependency on the moisture content of the fibers. The peak in the loadings at 1926 nm matches with the water peak. Plotting the scores of PC2 against the moisture content of the textiles proves this. The scores decrease with increasing moisture content for all NF textiles. Two PCs already explain all variance in the data, making it unlikely to find a possibility to differentiate the NF textiles by their NIR spectra.

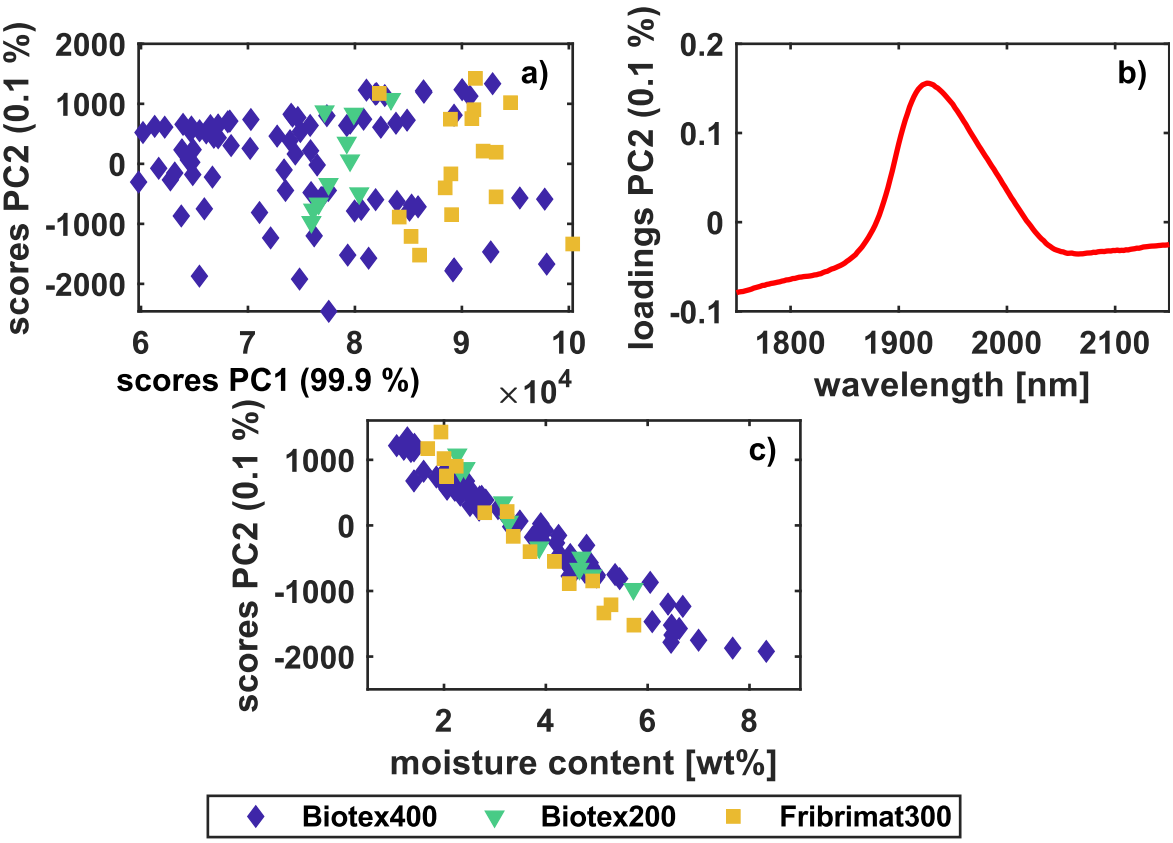

Figure 13: Scores of PC1 vs. Scores PC2 (a), the loadings of PC2 (b) and dependency of scores of PC2 on the moisture content (c).

However, the data has not yet been centered or preprocessed in any other way. By preprocessing (see Chapter 2.4.2.3), the information about the intensity can be removed from the data, making the moisture content more important for the PCA. Finding further information currently lost in the noise may also be possible.

2.4.2 Partial Least Square Regression

PLS is a powerful statistical method widely used in chemometric data analysis and has now become a standard method in spectroscopy [44]. Its primary goal is to predict one or more parameters (Y variables), such as a sample's physical or chemical properties, based on a comprehensive data set of measured values (X variables), often spectra. By considering the structure and relationships within the X variables and between the X and Y variables, PLS enables efficient modeling of complex systems, even when the number of measured values exceeds the number of observations or the measured values are highly correlated, as is the case with spectra.

The application of PLS is divided into three basic steps: calibration, validation, and the actual prediction or application. During the calibration phase, the PLS model is trained on a set of known X-Y data pairs to learn the relationship between the spectra and the sample properties. The model is tested against a separate data set in the subsequent validation phase to assess its predictive accuracy and reliability. Finally, the validated model is used in the prediction phase to estimate the properties of new samples.

Ongoing model maintenance ensures PLS-based predictions' long-term reliability and accuracy. Model maintenance includes regularly checking the agreement

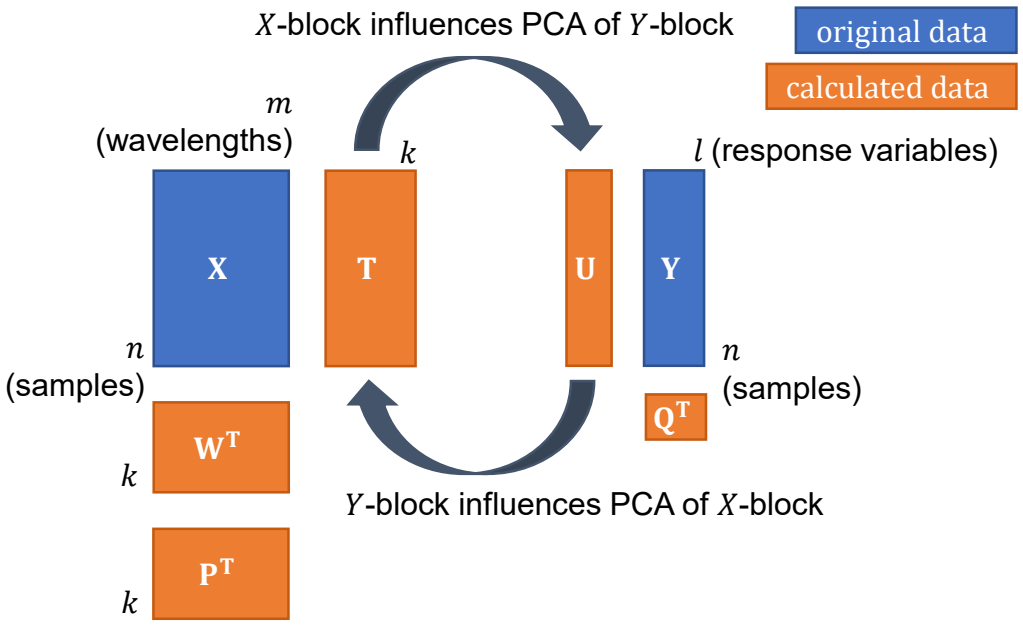

Figure 14: Schematic representation of the relationships in a PLS.

between the input and original calibration data and updating the model by integrating new reference values. This continuous adjustment allows the PLS to respond effectively to changes in the measurement conditions, the samples analyzed, or the analytical instruments, thus maintaining its predictive power. Like PCA (Section 2.3.2), PLS is based on the data matrix $\mathbf{X}$ with the dimension $n \times m$, n objects (samples), and m measured variables (e.g., wavelengths). In addition, for each object i, a target value y_i is measured ($i = 1 \dots n$) to create the vector y. If several target values y_{ij} are determined for one object, the different y_j result in the matrix $\mathbf{Y}$ with the dimensions $n \times l$, where l is the number j of the target values ($j = 1 \dots l$). The basic idea of the PLS is to carry out a PCA with both $\mathbf{X}$ and $\mathbf{Y}$, whereby both sides know about each other. The schematic sequence of the PLS is illustrated in Figure 14.

The basic idea of PLS is to extract latent variables from the $\mathbf{X}$ and $\mathbf{Y}$ data, aiming to maximize the covariance between these two data sets. In contrast to PCA, which focuses only on the variance within the $\mathbf{X}$ data, PLS explicitly considers the relationship between $\mathbf{X}$ and $\mathbf{Y}$. By using the weight matrix $\mathbf{W^T}$, the $\mathbf{X}$ data is transformed into a new space optimized to predict the $\boldsymbol{Y}$ data. This transformation allows the PLS to capture the variance within the $\mathbf{X}$ data and optimize the prediction performance with respect to the $\mathbf{Y}$ data.

The latent variables (LV) identified from the scores $\mathbf{T}$ (X data) and scores $\mathbf{U}$ (Y data) are selected to exhibit maximum covariance between the two data sets. The loading matrix $\mathbf{P}$ of $\mathbf{X}$ and its transpose $\mathbf{P^T}$ provide information on how the original $\mathbf{X}$ variables contribute to these latent variables. Similarly, the loading matrix $\mathbf{Q}$ of the Y-data (and its transpose $\mathbf{Q^T}$) provides insights into the relationship between the latent variables $\mathbf{U}$ and the original $\mathbf{Y}$-variables.

As with the PCA, the detailed mathematical derivation of the PLS is omitted here; corresponding good textbooks are available in German [44] and English [48, 49].

In the end, you get a PLS model with k LVs and a certain prediction quality for the parameter(s) being searched for. An increasing number of LVs can improve the model quality but also lead to overfitting, which deteriorates the prediction quality. A common approach is to use the LV at which the $RSMECV$ (Root Mean Square Error of Cross Validation, see Section 2.4.2.2) has a local minimum.

2.4.2.1 Cross-validation (CV)

Cross-validation is a widely used validation method that scores points for efficiently using data. It uses each object for both calibration and validation but in separate runs. This process involves repeatedly omitting some objects from the calibration data, creating a calibration model without these objects, and then predicting the omitted objects using this model to determine the residuals. This procedure makes it possible to assess the quality of the model by calculating the root mean square error of cross validation ($RMSECV$) (see Section 2.4.2.2).

Different approaches are used for selecting the samples to be omitted, ranging from full cross-validation, where each sample is omitted exactly once, to methods with larger data sets, where multiple objects are omitted simultaneously. Depending on the structure of the data set, the determination of which samples are omitted in which segments can be random or systematic.

If several objects (spectra) with different properties come from one sample, e.g., a change due to a change in the degree of cure, "*Continuous Blocks" can be used* as a CV method. *Continuous Blocks* remove a block of consecutive spectra with each run. Doing so prevents information about the predicted values in the model from being included in the CV. "*Venetian Blinds*" cross-validation is a method in which the data is divided into several segments. However, instead of using continuous data points for the validation sets, as with *Continuous Blocks, Venetian Blinds* selects data points at regular intervals across the entire data set. Each validation set contains data points distributed across the whole dataset, allowing for a more representative and less biased model validation. *Venetian Blinds* is particularly advantageous when analyzing data sets with a possible sequence or time dependency.

In addition to assessing the prediction quality for unknown data, cross-validation is particularly important for the PLS when determining the optimum number of LVs. The $RMSECV$ has a local minimum for a specific LV. The corresponding number of LVs represents a balance between the model's goodness of fit and its predictive ability for new data. A model that fits the calibration data too well will provide poorer predictions for data not included. If possible, removing approximately 8 % of a data set from each run is recommended to draw representative conclusions from the CV [50].

2.4.2.2 Evaluation of PLS models

Several characteristic values are considered for evaluating PLS models. These include the root mean square error ($RSME$) and the coefficient of determination (r^2). Depending on which step in the model creation process these characteristic values refer to, they are labeled accordingly. “C" stands for the calibration, i.e., $RMSEC$, "CV" indicates the cross-validation ($RMSECV$), and "P" indicates the validation ("Prediction"), $RSMEP$.

***RMSE*:** The $RMSE$ measures the average error and is calculated from the square root of the mean square error. To calculate the $RMSE$, the sum of the error squares, i.e., the difference between the predicted values from the regression equation and the actual reference values, is first determined. This sum is known as the Predicted Residual Sum of Squares ($PRESS$) or the error sum of squares, defined by the formula:

$$PRESS = \sum_{i=1}^{n} (y_i - \hat{y}_i)^2 \tag{6}$$

Where $\hat{y}_i$ is the value predicted by the PLS for the sample i. The residual variance s_R^2 is then calculated from the error sum of squares using the following formula:

$$s_R^2 = PRESS/n = \sum_{i=1}^{n} (y_i - \hat{y}_i)^2 /n \tag{7}$$

The $RMSE$ itself is determined as the root of this residual variance:

$$RSME = \sqrt{PRESS/n} = \sqrt{\sum_{i=1}^{n} (y_i - \hat{y}_i)^2 /n} \tag{8}$$

r^2: The coefficient of determination r^2 describes the correlation r between the measured y values and the predicted $\hat{y}$. It expresses the proportion of the variance described by the model. r^2 can be determined directly by expressing it as the ratio

of the explained variance to the total variance according to equation (9) or subtracting the unexplained variance (residuals) ratio to the total variance from 1.

$$r^2 = \sum_{i=1}^{n} (\hat{y}_i - \bar{y})^2 / \sum_{i=1}^{n} (y_i - \bar{y})^2 \\ = 1 - \sum_{i=1}^{n} (y_i - \hat{y}_i)^2 / \sum_{i=1}^{n} (y_i - \bar{y})^2 \quad (9)$$

2.4.2.3 Spectral preprocessing

As mentioned, the original measurement data in the PCA or PLS often does not provide good results. This is because the information sought is statistically lost in the amount of data. Disturbing effects in the spectra often have physical causes, such as changes in the amount of reflected light, shrinkage, or similar.

The spectra can be treated with chemometric methods to better determine better the information sought from them. The most common and frequently used techniques include normalization, centering, smoothing of the data, derivatives, and correcting scattering effects. For a detailed mathematical background, please refer to the literature [44, 49].

Normalization: Spectra are usually normalized to reduce scale effects and baseline fluctuations. Baseline variations can cause scale effects and baseline variations due to differences in sample preparation, the measurement process, or instrumental variations. Normalization can minimize these effects so that the analysis focuses more on the analytical signals and less on artifacts. The most common normalizations include vector normalization and baseline correction. With vector normalization (normed-1), each spectrum is divided by its norm (often the Euclidean norm) so that the length of the vector (in this case, the spectrum) is normalized to 1. This reduces scale effects between the spectra. For baseline correction, a baseline is estimated and subtracted from the spectrum. The estimate can, for example, run along the local minima of the spectrum. Baseline subtraction removes signal distortions due to absorption effects, light scattering, or background signals.

Centering: Centering involves adjusting the data values so that the center of the data, usually the mean value, is shifted to the origin of the coordinates. Centering is achieved by subtracting the average value of its variables from each data point. Mean Centering (MC) is the specific application of centering where the mean of each variable is subtracted from all values of that variable. This process is performed for all variables in the data set. Mean centering neutralizes differences in the magnitude of the variables, which is particularly important when the variables are measured in different units or have widely varying variances. In addition to the mean value, the median can be used as the center. Using the median reduces the influence of outliers on the position of the center. Other methods often perform centering and standardization in one step.

Smoothing: Smoothing reduces the noise in the data without significantly changing the essential characteristics of the spectrum, such as peak positions, heights, and widths. This can improve the signal-to-noise ratio. Standard methods for smoothing are the moving average and the so-called Savitzky-Golay filter. With the moving average, the value of each point is replaced by the average of a fixed number of neighboring points. The Savitzky-Golay filter uses polynomials to fit the data in a moving window and achieve smoothing without distorting significant signal characteristics.

Derivatives: First and second order derivatives of a spectrum can make small changes in the spectra more visible, which would be difficult to recognize in the original data. At the same time, a possible offset of the spectra and a possible baseline are removed, as these are close to 0 in the derivative. There are various approaches to deriving spectra. The most common are the derivative using the difference quotient method and the polynomial fit, also known as the Savitzky-Golay derivative. The difference quotient method estimates the first derivative using the simple difference between two neighboring data points. However, this approach increases noise in the spectra with each derivative. The Savitzky-Golay derivative works in the same way as smoothing with the Savitzy-Golay filter. The previously determined polynomial is derived, which makes this method more robust against noise.

Correction of scattering effects: When measuring samples by diffuse reflection, spectral differences often occur due to the sample's uneven distribution of scattering elements. These scattering phenomena are strongly influenced by the physical characteristics of the particles within the sample, particularly their size, which results in the light traveling different distances. In materials such as powders, granules, emulsions, or dispersions, the spectral information that could provide information about the chemical composition is often significantly obscured by scattering effects. The scattering is wavelength-dependent, varies with the refractive index of the materials, and thus changes across the entire spectrum. The scattering increases with decreasing wavelength. Multiplicative Scatter Correction (MSC) and Standard Normal Variate (SNV) are the most commonly used approaches for correcting scattering effects. In MSC, a linear regression is performed for each spectrum against a reference spectrum (or the mean of all spectra). This regression's slope coefficient and intercept are then used to adjust the spectra to better match the reference or average spectrum. MSC corrects for multiplicative scaling effects and additive baseline shifts. SNV is a method to correct scaling effects and scattering influences within individual spectra. Each spectrum is treated individually by subtracting the mean and then dividing by the standard deviation of the spectrum. This normalization results in each spectrum having a mean value of zero and a standard deviation of one. This transformation reduces effects caused by differences in sample presentation (such as varying particle sizes or different packing densities). SNV helps improve spectra comparability by bringing each measurement to a standard scale.

Since the preprocessed spectra are usually not shown, energy spectra of NF with different moisture contents and the effects of some preprocessing and their combinations are presented in Figure 15. The spectra originate from the experiments to determine the fiber moisture content; see Chapter 4. The original energy spectra scatter quite strongly in their intensity. Differences in moisture ($\lambda = 1920$ nm) are particularly noticeable between very low moisture contents and the rest. The spectra look similar due to similar approaches after applying normed-1 (b) and SNV (d). However, the Y-scales differ significantly. In the range of the

moisture peak, the spectra vary strongly. On the other hand, the areas not influenced by the moisture content hardly differ. However, differences between normed-1 and SNV can be observed in these areas. MC (c) removes the baseline and makes the differences in the moisture peak more visible compared to (a). As expected, the 1st Savitzky Golay derivative (d) removes the offset from the spectra. Apparent differences also occur here, especially in the moisture peak area. At the same time, the problem with the increased noise due to the derivative is also recognizable. A window width of 7 was used here. A larger window width would reduce this, but it always carries the risk of overlaying relevant information. The combination of SNV and MC (f) visualizes the differences in the spectra best. Both the moisture peak and the areas not directly influenced show apparent differences. The existing noise could still be reduced by smoothing.

In developing a PLS model, it is common practice to try out the effects of preprocessing on the model piece by piece, attempting to improve the PLS model. In addition to this approach, which is still widespread, automated model creation is tested due to the enormous computing capacities available, where many PLS models are first calculated with different preprocessings.

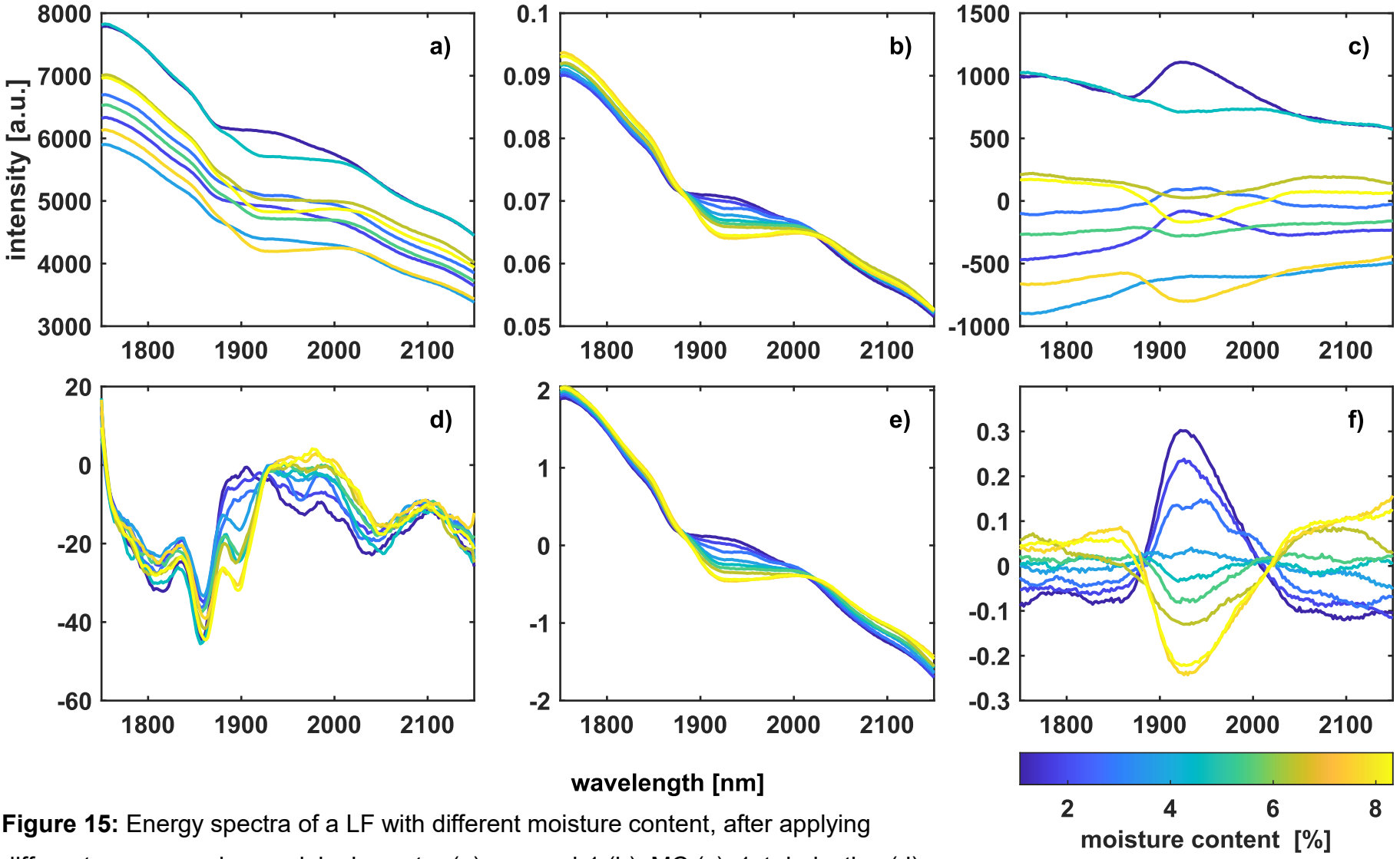

Figure 15: Energy spectra of a LF with different moisture content, after applying different preprocessings, original spectra (a), normed-1 (b), MC (c), 1st derivative (d), SNV (e) and SNV and MC (f).

2.4.2.4 Outlier analysis

An outlier analysis is a statistical process that aims to identify unusual observations in the data that differ significantly from the bulk of the data. These observations, known as outliers, may occur for various reasons, including measurement and data entry errors, or represent legitimate variations within the data. The main goal of outlier analysis is to identify these points and then decide how to deal with them - for example, whether they should be retained for further analysis, adjusted, or removed.

When evaluating NIR spectra using PLS, outlier analysis is necessary because outliers can significantly influence the calibration models. The many factors influencing NIR spectra and their complex structure can lead to spectra that do not fit the rest of the data set. These atypical data points can reduce model accuracy and predictive power by distorting the estimation of the PLS model parameters. The identification and correct treatment of outliers help to create more robust and reliable PLS models for the quantitative and qualitative analysis of NIR spectra.

There are various approaches for outlier analysis, and it must be decided on a case-by-case basis exactly how to deal with an outlier. The Cook distance is often used in regression analyses. The Cook distance measures the influence a single object has on the estimated parameters of a statistical model. It combines information about the leverage of a point - how unusual the values of its independent variables (X-block) are - and the size of the residual (the error between the observed value and the value predicted by the model) of that point. By taking both aspects into account, Cook's distance provides a comprehensive measure of how much a single observation affects the overall estimates of a regression model. The formula can calculate Cook's distance for the i-sample:

$$D_i = \frac{\mathrm{e}_\mathrm{i}^2 h_i}{s^2(1-h_i)^2} \tag{10}$$

D_i is the Cook distance of the i-sample, e_i^2 its residual, i.e., the difference between the measured and predicted value, $e_i^2 = (y_i - \hat{y}_i)^2$, and h_i is the leverage. It indicates how far the values of the independent variables (X-block) of this observation are from the average values of the independent variables in the data

set. High leverage indicates that the observation greatly influences the fit of the model. The leverage is determined via Hat-Matrix H:

$$\mathbf{H} = \mathbf{X}(\mathbf{X}^{\mathbf{T}}\mathbf{X})^{-1}\mathbf{X}^{\mathbf{T}} \tag{11}$$

H establishes the relationship between the measured and predicted values. The leverage h_i for a sample i is then $\text{the } i\text{-th}$ diagonal element of the hat matrix $\mathbf{H}$.

A high value of Cook's distance indicates that removing this observation would significantly change the estimated coefficients. However, when applying Cook's distance to outlier analysis, no absolute threshold indicates when a point is considered influential. Instead, the threshold depends on the context and must be determined by the researchers. Commonly used rules of thumb include a D_i-value greater than 1 or $D_i > 4/(n-k-1)$, where k is the number of LVs.

In practice, it is essential to examine Cook's distance, understand why samples are conspicuous, and decide how to deal with them. Cook's distance provides valuable insight, but the decision to treat an observation as an outlier and potentially remove it from the dataset should be based on a comprehensive analysis.

2.4.2.5 Application of the PLS

In practice, mathematical computation software tools such as the PLS-Toolbox of Matlab® or Unscrambler do most of the work, and the user only has to make the appropriate decisions. The application of the preprocessing and the calculation of the PLS models runs in the background. The following section provides a more profound insight into developing a PLS model and the decisions made in the process. The data set used comes from Chapter 4. It is used to predict the moisture content in NF textiles. For the calibration, 66 samples are available, each with 201 measured wavelengths (X-block: 66×201, Y-block: 66×1). The energy spectra are shown in Figure 15a. *Venetian blinds* are used for the CV, with 13 splits corresponding to the recommended approximately 8 % removed data with each split. SNV and MC were selected for preprocessing.

After choosing the preprocessing and CV, the number of used LVs is determined. Table 3 shows the change in variances (s_{LV}^2: variance explained by the LV, s_g^2: total variance explained) for the X- and Y-blocks and $RSMEC$ and $RMSECV$. Figure **16**

shows the change in $RMSEC$ and $RMSECV$ with increasing LVs. The first LV explains most of the variance of the X- and Y-blocks. The second LV already makes only a small contribution. An increasing number of LVs decreases in the X-block s_{LV}^2 while s_{LV}^2 fluctuates at a very low level in the Y-block. The $RMSEC$ decreases with increasing number of LVs. This decrease is to be expected, as the model increasingly better explains the fluctuations in the data. The $RSMECV$, on the other hand, decreases up to the fourth LV and then increases again. From then on, the PLS model is already so sensitive that it becomes unusable for data not included in the calibration. Typically, the number of LVs with the lowest $RMSECV$ is used. However, a lower number of LVs can also be used if the change in $RMSECV$ is tiny due to additional LVs. Each additional LV introduces a further dimension and, thus, further statistical uncertainty. For the present data set, two LVs were chosen. Three or four LVs improve the $RSMECV$ only insignificantly.

Table 3: Change from s_{LV}^2 and s_g^2 for X- and Y-block, as well as $RMSEC$ and $RSMECV$ with increasing number of LVs.

LV	s_{LV^2} (X-Block)	s_{g^2} (X-Block)	s_{LV^2} (Y-Block)	s_{g^2} (Y-Block)	$RMSEC$ [wt%]	$RSMECV$ [wt%]
1	97.24	97.24	97.33	97.33	0.292	0.306
2	1.17	98.41	0.79	98.13	0.245	0262
3	0.48	98.89	0.28	98.40	0.226	0.258
4	0.3	99.19	0.22	98.62	0.210	0.257
5	0.11	99.30	0.26	98.88	0.188	0.277
6	0.05	99.35	0.34	99.22	0.157	0.305

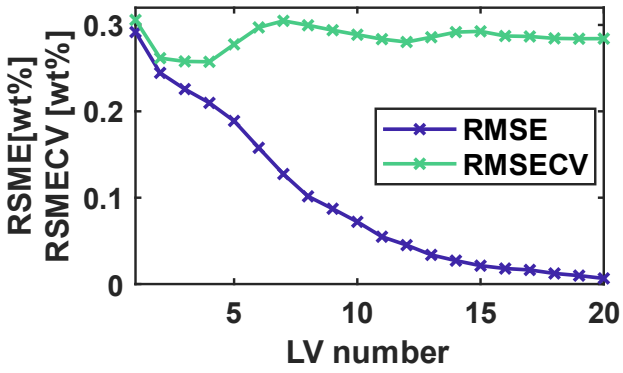

Figure 16: Change in $RMSEC$ and $RMSECV$ with increasing number of LVs.

Even now, it is often worth looking at how the PLS model performs. In Figure 17, the predicted moisture contents are plotted against the measured moisture contents, and the characteristic values for the PLS model are given. The values obtained from CV are usually shown. The predicted and measured values match if the values lie precisely on the bisector. The greater the distance between the data point and the angle bisector, the worse the model works. The model already determines the moisture content from the spectra quite well, and no value is initially conspicuous. Nevertheless, further data analysis will help to understand the model better.

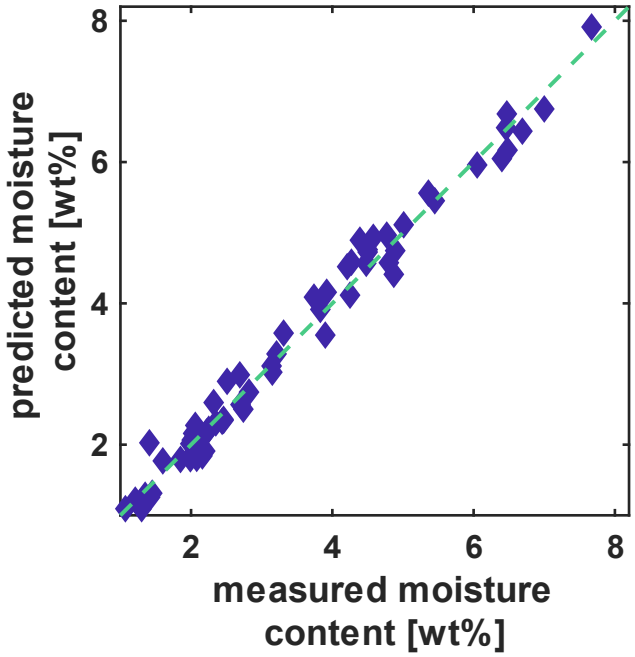

Parameters	Variable
LV	2
r^2C	0.981
r^2CV	0.979
$RSMEC$ [wt%]	0.24
$RMSECV$ [wt%]	0.26

Figure 17: Values from the CV of predicted versus measured moisture content of the NF-textile (left). Parameters of the PLS model (right).

The VIP scores indicate how much influence each variable (wavelength) has on the model (see Figure 18). Consequently, regions with changing peaks should be significantly influenced, while areas without change only contain noise. Values smaller than one are considered unimportant and could be removed from the model.

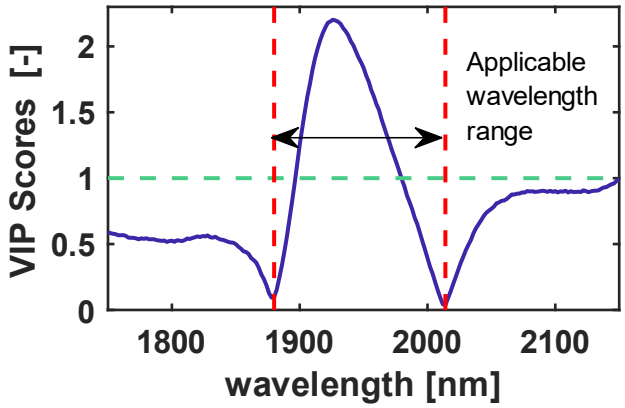

Figure 18: VIP Scores of the PLS model.

The cut is usually not set directly when the value falls below one but as soon as a local minimum is reached. This ensures that relevant peaks are mapped completely. The present PLS model is mainly influenced by the wavelength range between 1900 and 2000 nm, corresponding to the humidity peak. The PLS model could now be tested to determine whether the model improves if the other wavelength ranges are removed. However, care should be taken here, as the right-hand range, in particular, is close to one, and models can also deteriorate.

In addition to examining the influence of the individual variables via the VIP scores, the impact of the individual objects (samples) can be examined using outlier analysis. In contrast to the variables, the main aim is to remove objects with an influence that is too significant from the model in case of doubt. The Cook's distances are shown in Figure 19. All objects have a Cook's distance smaller than 1. However, the other common limit value (see formula (9)) shows potential outliers. One sample with 1.4 wt% moisture and a series with more than 6 wt% moisture are above the limit. In Figure 19, the first conspicuous sample (1.4 wt%) with a predicted moisture content of 2.03 wt% deviates significantly from the measured value. The deviation for the samples with a moisture content above 6 wt% is much smaller. Other statistical effects probably play a role here. The data set contains proportionally fewer samples with moisture contents > 6 wt% than with lower

moisture contents. At the same time, the predicted values also agree well with the measured values for high moisture contents. Whether or not samples should be removed from the data set is being tested. When considering which data should be removed here, it should also be considered whether high accuracy or a larger moisture range is more important for the model.

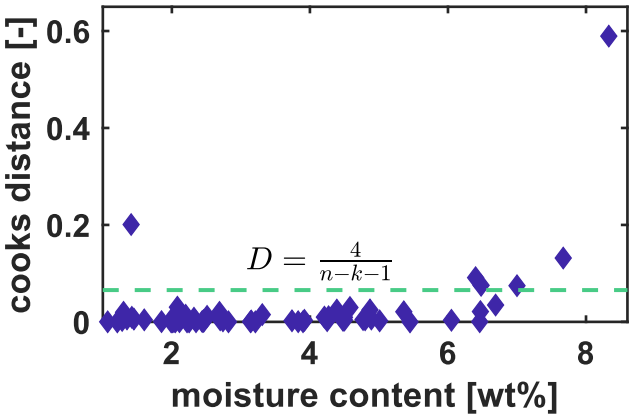

Figure 19: Cooks distance of each object using $D_i > 4/(n-k-1)$ as limit.

The steps shown for developing a PLS model are carried out iteratively to obtain a high-quality PLS model. Once a final PLS model has been found, it can be validated with the previously withheld data. Since the retained data can only be used once, the PLS model is not optimized for the validation data, so validation is not performed at this point.

2.5 Data flow during calibration and inline monitoring

In the preceding sections, it was demonstrated how spectra are measured and the fundamental workings of PLS were explained. Figure 20 connects the generation of spectra with the creation of the PLS model and its ultimate application for process monitoring, illustrating the data flow from measurement in the process to the quantitatively determined parameter. For subsequent inline measurement, it is recommended to measure the spectra directly in the process already during the creation of the PLS model (or any other evaluation method). The spectra, together with the reference data, form the X- and Y-blocks in PLS. Both blocks can be independently subjected to preprocessing. Subsequently, the calibration model, in this case, the PLS model, is developed. This model then allows for the quantitative

determination of parameters from spectra with unknown properties. With appropriate implementation, inline monitoring using NIR spectroscopy, with suitably short measurement times, can be performed almost in real-time.

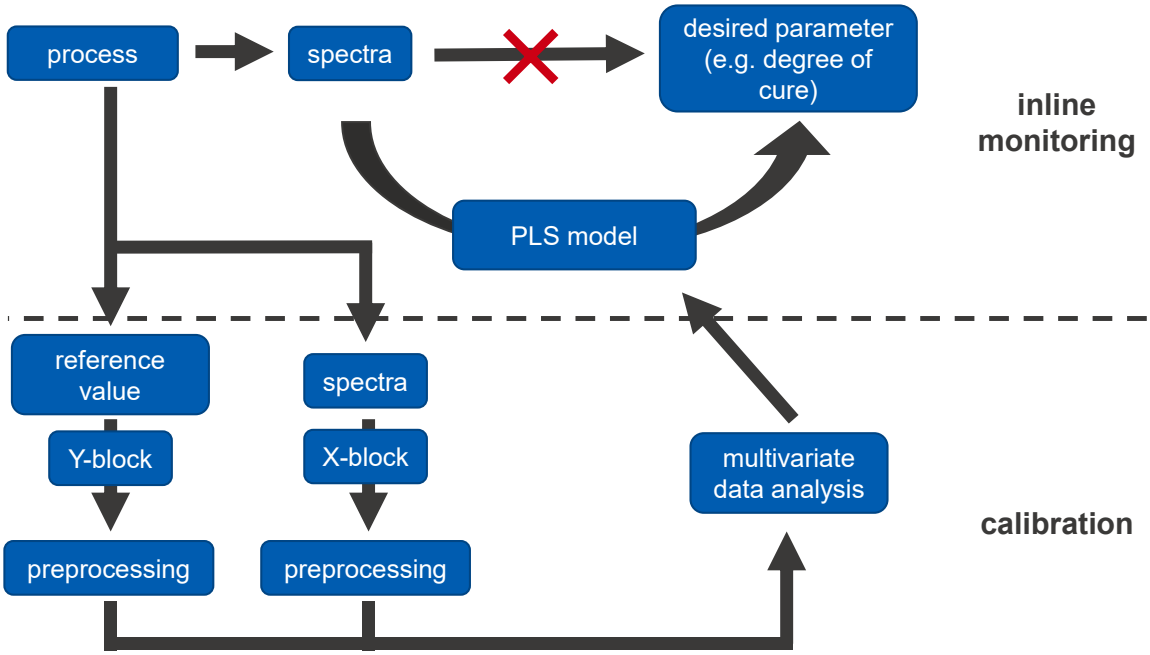

Figure 20: Overview over the data flow for applying NIR spectroscopy in a process.

2.6 State of the Art – NIR Spectroscopy in Composite Manufacturing

Process monitoring, or the continuous monitoring and analysis of process parameters, offers extensive benefits that positively affect efficiency, safety, quality, and cost control of processes and can provide valuable information about material conditions [11]. Additionally, it may be necessary to comply with legal requirements and ensure workplace safety. Process monitoring can be divided into two main categories: inline and atline monitoring. Inline Monitoring involves measurements directly in the process, while atline monitoring requires samples to be taken and analyzed near the process or in an attached laboratory. Besides inline and atline monitoring, there are other terms related to process monitoring, such as online monitoring, which refers to analysis in a specially set up bypass, or offline monitoring, often meaning a more in-depth analysis of the taken samples. However, these other terminologies ultimately fall into the previously mentioned categories of inline and atline monitoring, so no further subdivision is made here.

Inline monitoring allows for the direct and continuous monitoring of processes during operation. The measuring instruments are integrated directly into the process. This method enables real-time data collection and analysis, allowing for quick reactions to deviations or disruptions in the production process. Inline monitoring is particularly valuable in processes requiring constant quality control or adjustments. It minimizes the need for manual sampling, saving time and reducing the risk of contamination.
Atline monitoring typically requires manual sampling from the process, which is then brought to a nearby measuring device. Consequently, analysis cannot be performed in real time. However, there is often a larger selection of potential analysis methods unsuitable for inline integration. An intervention may only be possible with a delay or serve quality assurance and batch release.
In the production of FRP composites, several influencing factors along the process chain might be worth monitoring or are already being monitored. On the side of the reinforcement structure, the textile without defects, which is already commercially available through optical sensors [51], is fundamental. For resin-based matrix materials, the mixing ratio of the components and, if one goes further back, the concentration of relevant functional groups, in the case of epoxies, the epoxy equivalent weight (EEW), are relevant for the later mechanical properties [52, 53]. In the production of FRP composite using LCM, parameters such as the progress of the flow front, the degree of curing, and the void content [11] are relevant besides direct process parameters such as pressure and temperature.

2.6.1 Curing Chemistry of Epoxy/Amine Resin Systems

As many relevant parameters in LCM processes are directly related to the resin system, a fundamental understanding of the curing chemistry of the resin system is necessary. Epoxy/amine systems have been extensively studied in science but also have significant importance in mechanically demanding application fields, such as aerospace, due to their properties. These critical application fields simultaneously have an increased need for process monitoring to ensure component quality.
Epoxy resins are based on oxirane rings (also referred to as ethylene oxide groups), three-membered rings consisting of one oxygen and two carbon atoms connected via the so-called backbone. The backbone is typically either aromatic or aliphatic hydrocarbon. Epoxy resins for mechanical applications are usually based on

aromatic backbones, with bisphenol A diglycidyl ether (DGEBA) being the most common monomer.

Due to the ring strain, the oxirane ring is relatively reactive and reacts with proton donors. Common hardeners for epoxy resins include amines, amides, alcohols, acids, and anhydrides. In this case, the epoxy group reacts additively with the proton (see Figure 21). In the case of epoxy/amine resin systems, the proton shifts to the

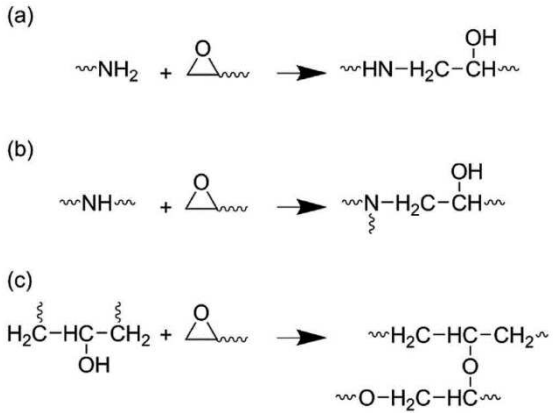

Figure 21: Curing reaction of an epoxy/amine resin system[54].

ethylene oxide group, resulting in a new hydroxy group in the addition product, while the primary amine becomes a secondary amine (Figure 21a). Subsequently, the secondary amine reacts with another ethylene oxide group, becoming a tertiary amine (Figure 21b). At significantly elevated temperatures, the formed hydroxy group can act as a proton donor and react with an ethylene oxide group (Figure 21c) [54].

2.6.2 Determination of the Degree of Cure

The degree of cure describes the extent to which functional groups have reacted, i.e., the achieved conversion. It is crucial both during processing and for the subsequent properties [55]. There are various methods for measuring the degree of cure, including differential scanning calorimetry (DSC), IR, and NIR spectroscopy.

Using DSC, the degree of cure can be determined from both isothermal and dynamic measurements or a combination of both [56–59]:

- Isothermal DSC measurement: The uncured resin is brought to the curing temperature as quickly as possible in the DSC device and maintained there for the curing time. The degree of cure as a function of time can be determined by

integrating the heat flow over time and normalizing the obtained area to the total measured heat flow.

- Dynamic DSC measurement with a constant heating rate: The heat flow into an uncured sample is measured at a constant heating rate. Additionally, several samples that were previously cured isothermally for different lengths of time are measured at the same heating rate as the uncured sample. The degree of cure for each sample is calculated as the relation of the measured residual enthalpy of each sample to the uncured sample. The dependence of the degree of cure on time can be found through interpolation.

- Dynamic DSC measurement with varying heating rates: In this approach, at least 3, often 5, samples are cured at different heating rates. The time-dependent degree of cure can be modeled from the measured DSC curves using isoconversional methods.

The degree of cure can also be determined by peak integration and normalization to a reference peak from IR and NIR spectra (see Section 2.3). Similar to the dynamic DSC measurement with a constant heating rate, several isothermally pre-cured samples are required. Alternatively, spectra can also be continuously recorded during curing. This requires a basic understanding of the spectra, of peaks directly affected by the curing reaction, and of peaks not involved in the reaction.

2.6.3 Peaks in IR and NIR Spectra

To determine the degree of cure from spectra, as described in the last section, and as a basis for analyzing the spectra via multivariable data analysis, an assignment of the peaks is necessary or at least useful. The assignment is typically done based on literature and spreadsheets referring the regarding functional groups. Similar chemical components are beneficial in the case of NIR spectra, as peaks appear in a wider range and are broader than in the IR range. In Chapter 5, the peaks of an epoxy/amine resin system are assigned to their respective functional groups and discussed.

2.6.4 Near Infrared Spectroscopy in Composite Processing

NIR spectroscopy stands out among other inline monitoring technologies primarily due to its wide range of detectable parameters and the ease of adapting the probe to the measurement environment. Essentially, it measures the concentration of functional groups in the measurement volume. Therefore, related parameters are fundamentally measurable, e.g. the degree of cure, describing the change in concentration of the reactive functional groups in a resin, determine parameters like gel time and glass transition temperature (T_g). In the literature, NIR spectroscopy has been documented for inline monitoring of composite processes for quality assurance of the resin in prepreg production [60–62] and by us in RTM processes [63, 64].

Even though it doesn't directly count towards the processing of composites, monitoring the resin synthesis and ensuring the concentration of functional groups is crucial for the quality of the later composite. The relationship between EEW and the epoxy peak seems to be so pronounced in laboratory measurements that the EEW can be determined based on the epoxy peak at 4530 cm^{-1} using the Lambert-Beer law [65]. Dan and Yi-Hui could also distinguish different batches of epoxy and phenol resins from various manufacturers using PCA with a laboratory device. The differences between the manufacturers were significantly more pronounced than the batch variations [43]. Directly during the resin synthesis, the acid and hydroxy values, equivalents to the EEW, were determined for natural and polyester resins [66, 67].

For prepreg production, the use of NIR spectroscopy in FRP composite processing is best documented. There are examples of a wide range of specific parameters and tested materials. Before impregnating the fibers, Jiang determined the sizing content of glass fibers [17], while Liu determined a powdered hardener's initiator content (0 - 0.5%) [68]. On the finished prepreg, the resin content and solvent fraction were determined for different material combinations (Glass/Epoxy resin, Glass/Phenol resin, Carbon/Epoxy resin, and Carbon/Phenol resin) [16–18, 61, 69, 70]. The degree of pre-curing of the prepreg is determined either by the gel time or the soluble resin fraction using NIR spectroscopy [17, 62, 70].

We demonstrated that the condition of the prepreg can also be checked during storage or directly before processing using NIR spectroscopy on a glass-fiber/epoxy

prepreg. The parameter we determined was the present T_g, which increases with increasing conversion [36].

In the field of LCM processes, we showed the potential for monitoring the degree of cure using NIR spectroscopy for a novel 100 % bio-based composite in the RTM process [63]. A flat textile was used as the reinforcement fabric, with a resin based on epoxidized linseed oil and crystalline citric acid as the hardener. In a more extensive study, we also determined the degree of cure of an epoxy/amine resin system in the RTM process. Due to the study's design, we encountered limitations in determining the degree of cure at the beginning of the curing phase, α_0, which is revisited in Chapter 6.

3 NIR and IR Spectra of Epoxy/Amine Resin Systems

Although analyzing spectra graphically and assigning peaks does not allow to link spectra with quantitative parameters, understanding the used spectra can provide helpful information to better understand the dataset. This knowledge can be valuable during the development of the PLS models, as it can give, e.g., indications of particularly important wavelength ranges or those that should be excluded because they might be influenced by irrelevant functional groups.

To improve the understanding of the spectra of an epoxy/amine resin system, in the following peaks in the NIR spectra of an uncured and cured epoxy/amine resin system, as well as the neat components, are assigned. This is done for all spectra of the four spectrometers of the NIRONE series. These spectra are compared with the spectra of a full-scale FTNIR spectrometer as well as with the IR spectra of the components.

3.1 Measuring an Epoxy/Amine Resin System

3.1.1 Used Material

The used epoxy resin was Epinal IR 78.31, as amine hardener Epinal IH 77.11 was used, both from bto-epoxy GmbH (Amstetten, Austria). The mixing ratio was 100/25 (resin/hardener).

3.1.2 Sample Preparation

20 g of resin was weighed into a pot, and 5 g of hardeners were added. The components were thoroughly mixed by hand. Subsequently, they were degassed for 5 min.

For the measurements with the NIRONE spectrometers, 2.5 g of each component and of the mixed resin were weighted into aluminum dishes (cross-section: 55 mm, height: 20 mm).

For the measurements with the FTNIR spectrometer, 20 g of each component and of the mixed resin were weighted into aluminum dishes (cross-section: 80 mm, height: 28 mm).

The dishes with mixed resin and a further thin sample were cured at 100 °C for at least 30 min.

3.1.3 NIR Measurements

The samples were measured with all four spectrometers of the NIRONE series (S1.7, S2.0, S2.2, and S2.5) using Steps of 5 nm, a PointAvg of 100, and a *ScanAvg* of 50.

The process spectrometer from i-Red Infrarot Systeme GmbH (Linz, Austria), equipped with a measuring head, is used as an FTNIR spectrometer. The measuring head consists of 4 halogen bulbs with a collecting lens (20 mm) in the center between them. The measuring head was connected to the spectrometer via an optical fiber (cross-section: 400 µm, length: 8 m). The measuring distance between the measuring head and the sample was 90 mm. For each measurement, 50 samples were averaged.

3.1.4 IR Measurements

The IR measurements were performed on a BRUKER VERTEX 70 (Bruker, Massachusetts, United States) in reflection mode. For all samples, 16 scans were averaged, except for the cured resin, for which 64 scans were used, each with a resolution of 2 cm^{-1}.

3.2 Assigning Peaks in NIR- and IR- Spectra

As mentioned, assigning peaks to functional groups can help understand a data set and accelerate the development of PLS models. Due to the small measurement range of the NIRONE spectrometers, it is essential to choose a suitable spectrometer that covers the relevant wavelength ranges. Therefore, the spectra of the epoxy/amine resin system are analyzed, and the absorption peaks are assigned to the functional groups that cause them. The epoxy resin Epinal IR78.31 used is referred to below as "resin", while the hardener Epinal IH77.11 is referred to as "hardener". The state of the resin system is referred to as "uncured" and "cured" to describe the measurement before and after curing, respectively.

For a better display, the spectra are given different offsets so they do not overlap but are still comparable. As the peaks of one absorption peak appear in the same

region in the samples, only one $\tilde{\nu}$ or λ is is given during the discussion. Tables 5 and 6 provide a complete overview of the peak positions in the different samples.

3.2.1 IR Measurements

The IR spectra of the pure components and the uncured and cured resin system are shown in Figure 22. Absorption peak 1, at 3510 cm^{-1}, results from the stretching vibration of O-H in phenols in the resin. It is very weak, so it could indicate unreacted hydroxy groups that remain after resin synthesis. In the cured sample, the O-H group shows a broad absorption peak, with its peak at 3390 cm^{-1} (peak 2). These hydroxy groups result from the curing process. The hardener and the uncured sample show two absorption peaks at 3364 and 3287 cm^{-1}resulting from the stretching vibration of primary and secondary amines (N-H, peak 3). The absorption peak 4, from 2840 to 3000 cm^{-1}, comes from stretching vibrations of aliphatic and aromatic C-H and is present in all four samples. The three absorption peaks belonging to 5 (1607, 1581, and 1508 cm^{-1}) are caused by the stretching of phenyl rings and overlap with the bending of the primary amine (NH2) groups (absorption peak 6), present in the hardener and the uncured sample. In the region below

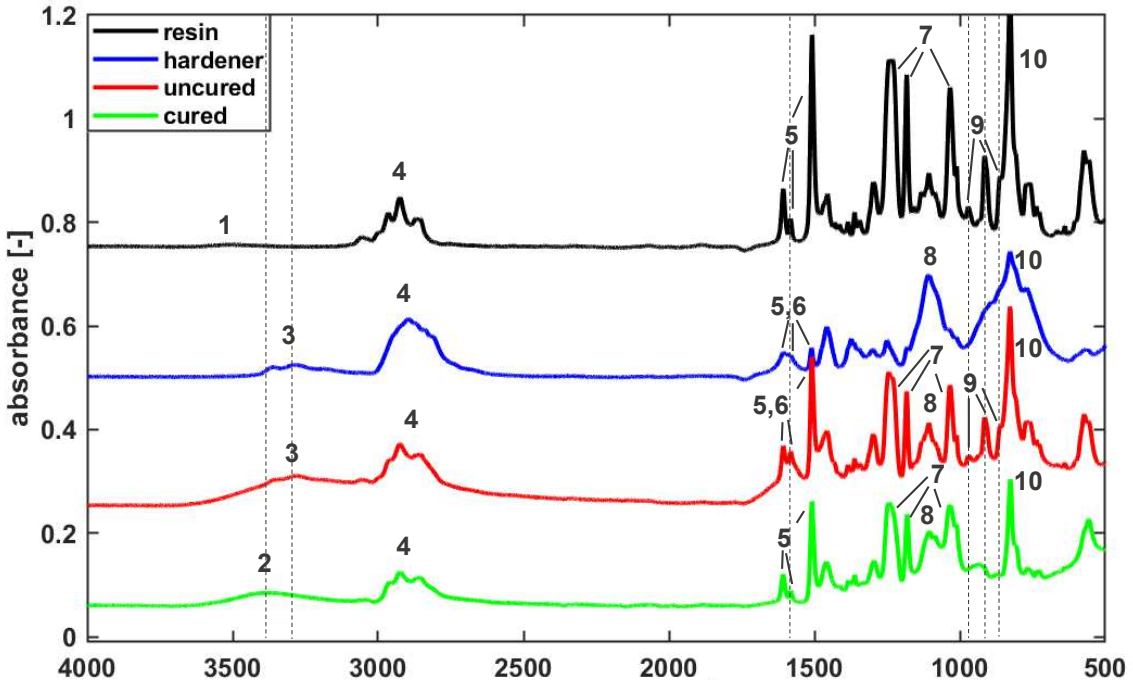

Figure 22: IR spectra of neat resin and hardener as well as of the uncured and cured resin system. Absorption peaks of functional groups consumed during curing (---) change as expected, while the peaks of the formed hydroxy groups emerge.

1500 cm^{-1}, not all peaks can be assigned clearly. Absorption peak 7 is caused by the asymmetrical (1243 and 1281 cm^{-1}) and symmetrical (1033 cm^{-1}) stretching of ether groups (C-O-C). They are present in the resin, uncured, and cured sample. As they do not change during curing, they do not represent the epoxy group (cyclic ether). Instead, they come from the oxygen atom, connecting the glycidyl group with the phenyl ring. Absorption peak 8, present in the hardener (1110 cm^{-1}), uncured (1106 cm^{-1}), and cured (1105 cm^{-1}) sample, results from the stretching of amides (C-N). From the epoxy groups, the absorption peaks occur at 970, 914, and 861 cm-1 (peak 9), present in the resin and uncured sample. All the peaks vanished in the cured sample. The peak at 861 cm-1 appears only as a shoulder of absorption peak 10 (827 cm^{-1}), which is the out-of-plane bending of aromatic hydrogen (=C-H). The assigned peaks are summarized in Table 4. The assigned absorption peaks are in good agreement with general IR tables [71, 72], more specific literature about IR spectroscopy of specific groups [73–75], and with literature assigning absorption peaks of epoxy/amine resin systems [76–79].

Table 4: Assignment for the observed absorption peaks of the pure components as well as the uncured and cured resin system.

Peak Nr.	Absorption Peak	Resin [cm^{-1}]	Hardener [cm^{-1}]	Uncured [cm^{-1}]	Cured [cm^{-1}]
1	Ph-OH, str.	3510			
2	-OH				3390
3	$-NH_2$, -NH str.		3364 and 3287	3364 and 3287	
4	-CH, $-CH_2$, $-CH_3$ (ar./aliph.)	3000-2800	3000-2800	3000-2800	3000-2800
5	-C=C- ar., str.	1607, 1581, 1508	1607, 1581, 1510	1607, 1581, 1508	1608, 1581, 1507
6	$-NH_2$, bend.		~1600,	~1600,	

Peak Nr.	Absorption Peak	Resin [cm^{-1}]	Hardener [cm^{-1}]	Uncured [cm^{-1}]	Cured [cm^{-1}]
7	-C-O-C-, str.	1243, 1182, 1033		1243, 1183, 1033	1243, 1181, 1033
8	-C-N-, str.		1110	1106	1105
9	-(CH-O-CH_2)	970, 914 and 861		970, 914 and 861	
10	C-H, ar. bend.	827	827	827	827

3.2.2 NIR Measurements

The NIR spectra measured with the NIRONE spectrometers are compared with the NIR spectra from a full-scaled process spectrometer (Figure 23), and the absorption peaks are assigned. The available NIRONE spectrometers together cover the wavelength range between 1350 to 2450 nm ($\tilde{\nu} =$ 7407 to 4081 cm^{-1}), while the useful measuring range of the FTNIR spectrometer is between 4000 and ~13000 cm^{-1} (2500 to 770 nm), covering the entire NIR region. The spectra of the NIRONE spectrometers show a much broader absorption peak than the FTNIR spectra. When comparing them with the IR spectra (Figure 21), even the absorption peaks of the FTNIR spectra are broad. The small measuring ranges of the NIRONE spectrometers and the broad absorption peaks result often in only the shoulders of a peak being present in the spectrum. In these cases, in the assignment, the peak is marked with “<” or “>” of the maximum or minimum of the wavelength of the spectrometer.

The following assignment of the absorption peak is in good accordance with the first peak assignments from the late 1950's [80, 81] and with other literature dealing with NIR spectroscopy of epoxy/amine resin system [41, 79, 82–84], epoxy resins [85, 86] and amine components [87, 88]. An overview of the absorption peaks is also given in Table 5.

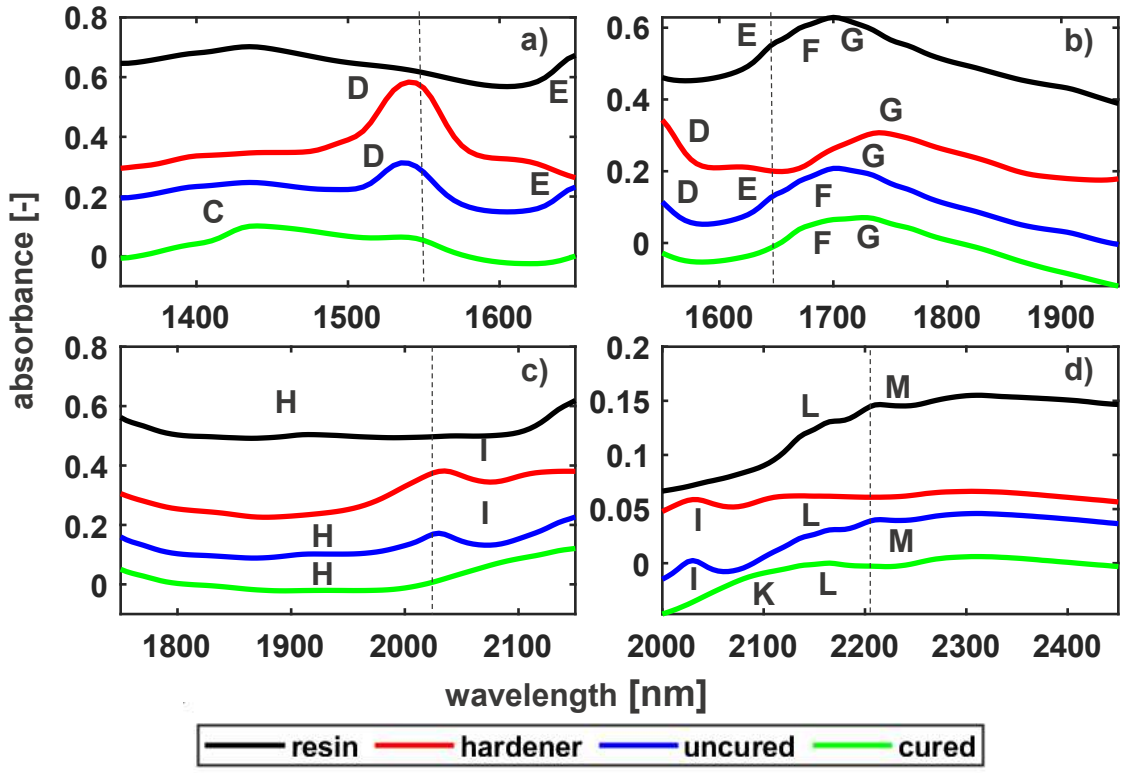

Figure 23: NIR spectra of neat resin and hardener as well as of the uncured and cured resin system measured with the NIRONE spectrometers, S1.7 (a), S2.0 (b), S2.2 (c) and S2.5 (d).

Out of the range of the NIRONE spectrometers, the spectra of the FTNIR spectrometer show two absorption peaks, A and B. Peak A ($\tilde{\nu} = 9535$ cm^{-1}) results from the second overtone of the amine stretching vibrations (IR peak 3, $\tilde{\nu} = 3364$ and 3287 cm^{-1}) and is therefore only present in the hardener and the uncured resin. Peak B ($\tilde{\nu} = 8624$ cm^{-1}) is caused by the second overtone of the epoxy groups and is only present in the resin and the uncured sample. The corresponding peak was not assigned in the IR spectra. It would be expected at $\tilde{\nu} \sim 2875$ cm^{-1}. Several peaks of methylene groups are assigned at this region of the IR spectra. The NIR spectra show further peaks in this region, which are not assigned here. The assigned peak

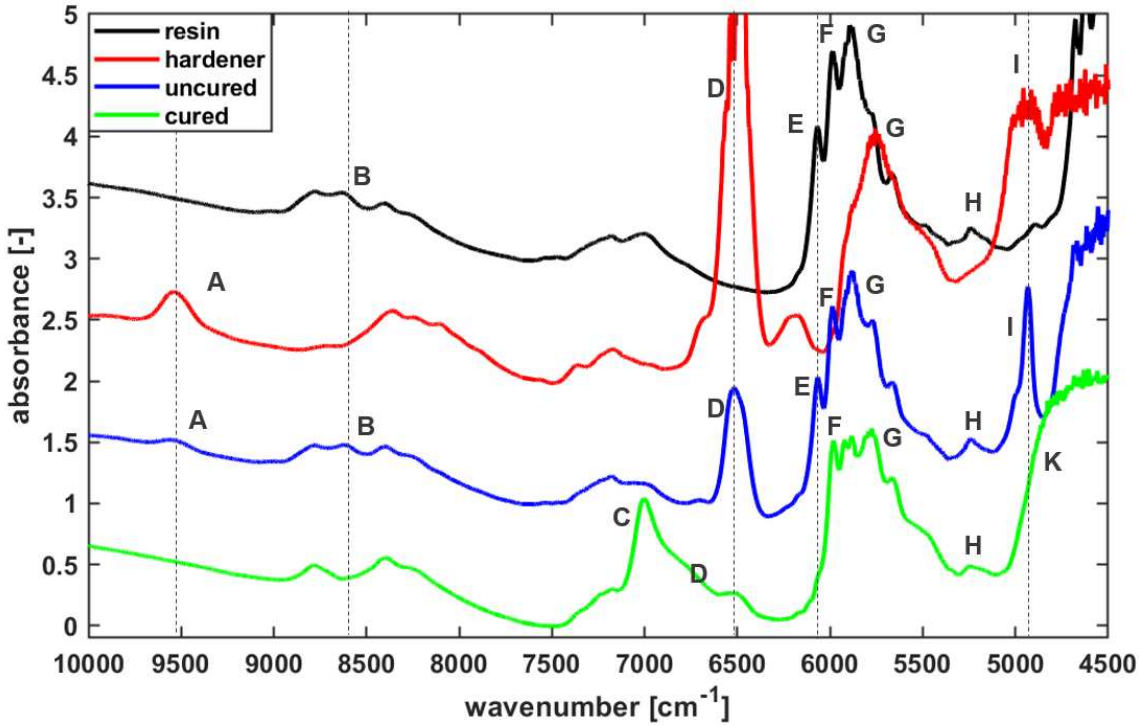

Figure 24: NIR spectra of neat resin and hardener as well as of the uncured and cured resin system measured with an FTNIR spectrometer. Absorption peaks of functional groups consumed during curing (---) change as expected, while the peaks of the formed hydroxy groups emerge.

is not present in the hardener or in the cured sample, i.e., consumed during curing, proving that it must be the epoxy peak. The first peak covered by the NIRONE S1.7 is peak C ($\tilde{\nu}$ = 6998 cm-1, λ = 1440 nm), caused by the hydroxyl groups that form during curing. This is the first overtone of the hydroxy groups (IR peak 1 and 2, $\tilde{\nu}$ = 3510 and 3390 cm^{-1}). In the spectra of the S1.7 spectrometer, it appears to be a vast peak. The absorption peak coming closest to a peak in the NIRONE spectra is peak D ($\tilde{\nu} = 6522$ cm^{-1}, λ (S1.7) = 1540 nm, λ(S2.0) < 1550 nm), the first overtone of the amine stretching vibration (IR peak 3, $\tilde{\nu} =$ 3364 and 3287 cm^{-1}). The S1.7 spectrometer covers the whole peak where it is strongly present in the hardener and uncured sample, as expected. However, the cured sample also displays a weak peak. The S2.0 displays only a shoulder of peak D; here, the same finding as for the spectra from S1.7 can be made. The same applies to the FTNIR spectra. The sample was probably not fully cured, or an excess of hardener was added. The peak of the stretching of terminal methylene groups of the epoxy group (peak E, $\tilde{\nu} = 6069$ cm^{-1}, λ(S1.7) >1650 nm, λ(S2.0) = 1650 nm) is present in the resin, and

the uncured sample. The peaks F and G are the second overtone of aliphatic (G, $\tilde{\nu}$ = 5895 cm^{-1}, λ(S2.0) = 1700 nm) and aromatic (F, $\tilde{\nu}$ = 5987 cm^{-1}, λ(S2.0) = 1670 nm) C-H stretching vibrations (IR peak 4, $\tilde{\nu}$ = 3000-2800 cm^{-1}). The absorption peak H indicates the presence of water (H2O, $\tilde{\nu}$ = 5239 cm^{-1}, λ(S2.0) = 1915 nm) in the resin, uncured and cured sample. The first combination vibration found is from amines (peak I combination $\tilde{\nu}$ = 4957 cm^{-1}, λ(S2.0) = 2035 nm, λ(S2.5) = 2030 nm). It is the combination of IR peak 3 ($\tilde{\nu}$ = 3365 cm^{-1}) and 6 ($\tilde{\nu}$ = 1607 cm^{-1}). The combination peak (peak K, $\tilde{\nu}$ ~ 4827 cm^{-1}, λ(S2.5) ~2090 nm) of the hydroxyl groups appears as a shoulder in the spectra of the cured samples. Due to the measuring setup of the FTNIR spectrometer, the rest of the NIR range is very noisy and does not deliver any further useful information. On the other hand, spectra of the NIRONE S2.5 show two additional peaks. Peak K, actually two peaks, are the combination vibrations of the aromatic methylene groups (λ(S2.5) = 2140 and 2165 nm) caused by the IR peaks 4 and 5. Peak L (λ(S2.5) = 2210 nm) is related to the methylene groups of the epoxy ring. It is present in the resin and uncured sample and vanishes during curing.

Table 5: Assignment of the absorption peaks of an epoxy/amine resin in the NIR range.

Peak	Absorption Peak	Spectrometer	Resin	Hardener	Uncured	Cured
A	Amine-2. overtone	FTNIR [cm^{-1}]		9539	9553	
B	Epoxy-2. overtone	FTNIR [cm^{-1}]	8624		8616	
C	Hydroxy-1. overtone	FTNIR [cm^{-1}]				6998
		S1.7 [nm]				1440
D	Amine-1. overtone	FTNIR [cm^{-1}]		~6500	6522	
		S1.7 [nm]		1540	1535	
		S2.0 [nm]		<1550	<1550	
E	Epoxy-1. overtone	FTNIR [cm^{-1}]	6069		6065	
		S1.7 [nm]	>1650		>1650	
		S2.0 [nm]	1650		1650	
F	Amine -2. overtone	FTNIR [cm^{-1}]	5987		5991	5983
		S2.0 [nm]	1670		1670	1670

Peak	Absorption Peak	Spectrometer	Resin	Hardener	Uncured	Cured
G	Epoxy-2. overtone	FTNIR [cm^{-1}]	5895	5765	5873	5776
		S2.0 [nm]	1700	1740	1700	1720
H	Hydroxy-1. overtone	FTNIR [cm^{-1}]	5239		5237	5246
		S2.2 [nm]	1915		1915	
I	Amine-1. overtone	FTNIR [cm^{-1}]		4957	4933	
		S2.2 [nm]		2035	2030	
		S2.5 [nm]		2030	2030	
K	Epoxy-1. overtone	FTNIR [cm^{-1}]				~4827
		S2.5 [nm]				~2090
L	ar.-CH overtones	S2.5 [nm]	2140 and 2165		2140 and 2165	2165
M	Epoxy-CH combination	S2.5 [nm]	2210		2210	

3.3 Comparing IR and NIR Spectra of an Epoxy/Amine Resin System

The peaks of the absorption bands of the FTNIR spectrometer and the NIRONE spectrometers match with reasonable precision when they are in the measuring range. They are also in agreement with the fundamental vibrations in IR spectroscopy. However, it is obvious that the spectra of the NIRONE spectrometers show broader and less intense peaks than the FTNIR spectra. This is partly due to the poorer resolution of the NIRONE spectrometers. The NIRONE spectrometers have a resolution of only 16 nm, while the FTNIR spectrometer has a resolution of 2 cm^{-1}. Due to mathematical reasons, the resolution difference between the spectrometers is not constant over the NIR range. At 1350 nm, the beginning of the measuring range of the NIRONE spectrometer, the 16 nm correspond to approximately 86 cm^{-1}, while at the upper end of the measuring range at 2450 nm, they correspond to approximately 26 cm^{-1}. The resolution of the NIRONE spectrometer is, therefore, 13 to 42 times worse than that of the FTNIR spectrometer, depending on the wavelength.A comparison of IR and FTNIR spectra also shows that the peaks becomes broader in the NIR and is less distinct than in the IR.

The presence of only a few absorption peaks in the measuring range of each NIRONE spectrometer has several implications for process monitoring. Generally, the spectrometer must be selected according to the chemical changes occurring in the process. When monitoring an epoxy/amine system, the NIRONE spectrometers show different amounts of relevant peaks. Most pertinent in this case are peaks from functional groups related to the curing process, such as epoxy, amine, and hydroxy groups. Consequently, the NIRONE S2.5 should be the most suitable, as absorption peaks of all three functional groups are located in the measuring range (peaks I, K, and M). The NIRONE S1.7 also measures all three functional groups (peaks C, D, and E), even if only one shoulder of the epoxy peak (peak E) is measured. The NIRONE S2.0 should contain considerably less information, as it only measures one epoxy peak (peak E) and the shoulder of the amine peak (D). Only the NIRONE S2.2 measures even less relevant peaks, as only the combination oscillation of the amines (peak I) lies within its measuring range.

4 Determination of the Moisture Content of Natural Fibers in the RTM Process

Natural fibers being used increasingly being used in the FRP industry, as they represent an alternative to glass fibers in terms of both price and mechanical properties [1, 89, 90]. A key parameter in the processing of NF is the moisture absorbed by the fibers, e.g. for flax fibers 8-10 wt% moisture content at ambient conditions are reported [91]. But even the smallest amounts of moisture have a negative effect on the mechanical properties of NFRP [92]. This raises the interest and necessity for determining fiber moisture content simply, fast, and automatically inline.

For this work, the fiber moisture is determined in a closed RTM mold. Corresponding measurements are carried out, and PLS models are developed based on this. The transferability of the best PLS model to other NF textiles is investigated subsequently.

4.1 Materials and Experimental Methods

4.1.1 Used Materials

For the calibration of the PLS models, a flax fiber textile, Biotex Flax 400g/m² 2x2 Twill (“Biotex400”, Composites Evolution Ltd., Chesterfield, UK), is used (see Figure 25). The transferability of the best PLS model found is tested on Biotex Flax 200g/m² 2x2 Twill (“Biotex200”, Composites Evolution Ltd., Chesterfield, UK) and a non-woven flax fabric Fibrimat F300 (“Fibrimat300” Eco-Technilin SAS, Valliquerville, France, FAW: 450 g/m²). The Fribrimat F300 contains a lot residues shives.

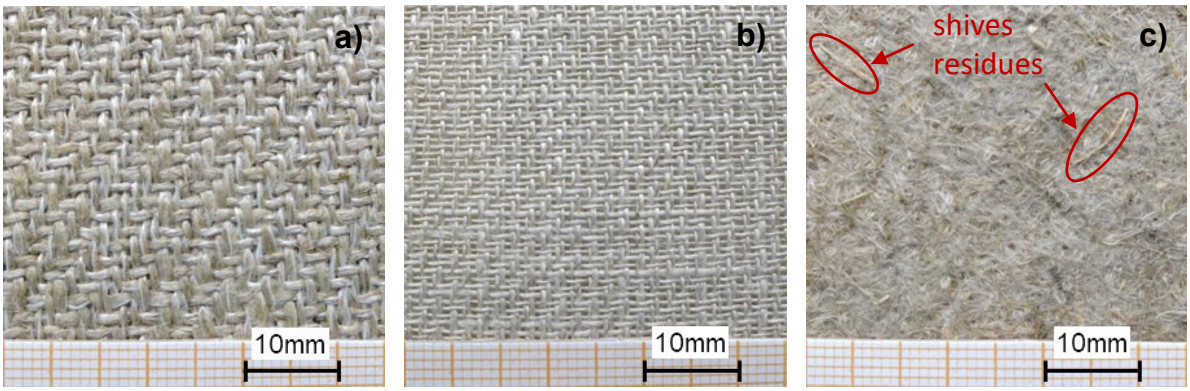

Figure 25: Used fabrics to determine the moisture content of NF fabrics in the RTM process, Biotex400 (a), Biotex200 (b), Fibrimat300 (c), reproduced with permission from Blößl[93].

4.1.2 Used RTM-Equipment

The experiments used a square flat mold ("plate mold"). The cavity dimensions were $270 \times 270 \times 4$ mm, and the mold was mounted on an LZT-OK-80-SO press (Langzauner GmbH, Lambrechten, Austria). The NIR adapter is placed in the center of the upper mold half (see Figure 26).

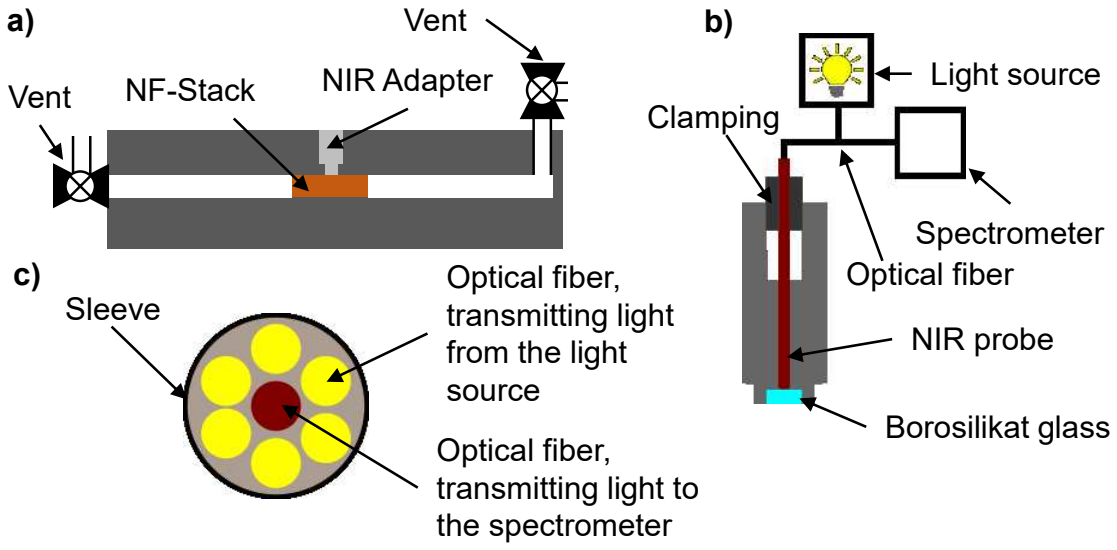

Figure 26: RTM-Mold with the NF-Stack and NIR adapter (a), concept of the NIR-Adapter (b) and cross section of the NIR-Probe (c).

4.1.3 NIR Measurements

The NIRONE S2.2 is equipped with a NIR probe (400 µm fiber core, Avantes BV, Apeldoorn, Netherlands) for the NIR measurements. The probe consists of 6 optical fibers (cross-section 400 µm each) bringing light from the light source (Avantes BV, Apeldoorn, Netherlands) into the cavity of the plate mold (see Figure 26b). The centered fiber transmits the reflected light to the NIRONE S2.2. The probe was mounted in a specifically designed adapter, holding it in place. To protect the probe's tip, the adapter covers it with a 5 mm thick borosilicate slide.

The NIR measurements are done using *Steps* of 2 nm, *PointAvg* of 10, and *ScanAvg* of 5.

4.1.4 Determination of the Moisture Content

After the NIR measurement, the top layer of the NF stack is immediately placed in the “moisture determinator” (DAB Feuchtigkeitsbestimmer 1.2, KERN & Sohn GmbH, Balingen, Germany), and the measurement is started. The DAB moisture analyzer heats the sample to 120 °C with a halogen lamp and then maintains the temperature. The weight loss is recorded. The measurement is stopped automatically if the weight changes over 45 s are less than 2 mg. The moisture content is calculated by the “moisture determinator” using:

$$c_{MC} = 1 - (m_{\mathrm{w}} - m_{\mathrm{d}})/m_{\mathrm{w}} \tag{12}$$

With c_{MC} [wt%] being the moisture content and m_w and m_d are the mass of wet and dried sample, respectively.

4.1.5 Sample Preparation

Sample stacks with cuts of 65×65 mm were used to determine the moisture content. All samples were placed in the preheated (80 °C) plate mold. The samples of Biotex400 were prepared in three different ways to cover a wide range of moisture content. Samples of Biotex200 and Fibrimat300 were only treated with the second method. The number of layers per sample is given in Table 6.

For a moisture content of less than 1.5 wt%, the samples were dried in an oven for 120 min. Then, they were stacked and immediately placed in the plate mold before it was closed. This resulted in a moisture content between 1.28 and 1.45 wt%.

The stack was placed in the plate mold to achieve a moisture content between 1.5 and 6.7 wt%. To adjust the moisture content, vacuum was then applied to the sealed mold at the outlets for 0 to 1200 s. After releasing the vacuum, the NIR spectra were recorded.

To achieve a moisture content of more than 6.7 wt%, the samples were placed in a humidity chamber with 70 % humidity at 30 °C for 1 h. They were then stored at ambient conditions for a varying period of time in order to achieve different moisture contents in the preform.

Table 6: Overview of the number of layers per sample used for the different textiles.

Textile	Number of layers per sample	Moisture content [wt%]	Sample preparation
Biotex400	5	< 1.5	Drying in an oven
		1.5-6.7	Applying vacuum on the RTM mold
		>6.7	Humidity chamber
Biotex200	10	2.2-5.9	Applying vacuum on the RTM mold
Fibrimat300	7	1.8-5.9	Applying vacuum on the RTM mold

Two datasets were measured from the Fibrimat300. In the first, it was placed under the NIR adapter similar to the other fabrics. In the second case, the samples were placed, so that shive residues were placed under the NIR measuring spot (shives are marked in Figure 25c).

4.1.6 Statistical Analysis

The moisture content was determined from a total of 83 Biotex400 samples. These were randomly divided into two data sets for calibration, 66 samples, and validation, 17 samples. Ten samples each of Biotex200 and Fibrimat300 were measured. Six samples of the shive residues in the Fibrimat300 were measured.

In the first screening, several PLS models were developed. For the LVs, a number between 1 and 10 were tested using different preprocessings (SNV, SM, 1. Deriv, 2. Deriv, MC, SNV+SM, SNV+1.Deriv, SNV+2.Deriv, SNV+MC, SNV+SM+MC, SNV+1.Deriv+MC, SNV+2.Deriv+MC). The window of the applied Savitzky-Golay Filter is seven points. The best model found was further optimized by removing outliers and limiting the used wavelength range.

Cross-validation was done by *venation blinds*, using 13 data splits. For the PCA, the original and processed datasets were tested, applying the same preprocessings as described above.

4.2 Results

The spectra from the NIRONE S2.2 of Biotex400 show only two absorption peaks, see Figure 27. The absorption peak at 2100 nm is more or less constant, while the absorption peak at 1924 nm is changing. It decreases with the moisture content. The peak at 1924 nm is attributed to the absorption of water [93]. The absorption peak at 2100 nm is unknown and cannot be assigned to a functional group. The spectrum of the sample with a moisture content of 1.07 wt% does not show any peak in the region around 1924 nm. However, the reference measurement still indicates some weight loss, which is attributed to the remaining moisture. Moisture contents below 1.07 wt% could not be achieved. Therefore, the measured weight loss is probably moisture, which is taken up during sample handling.

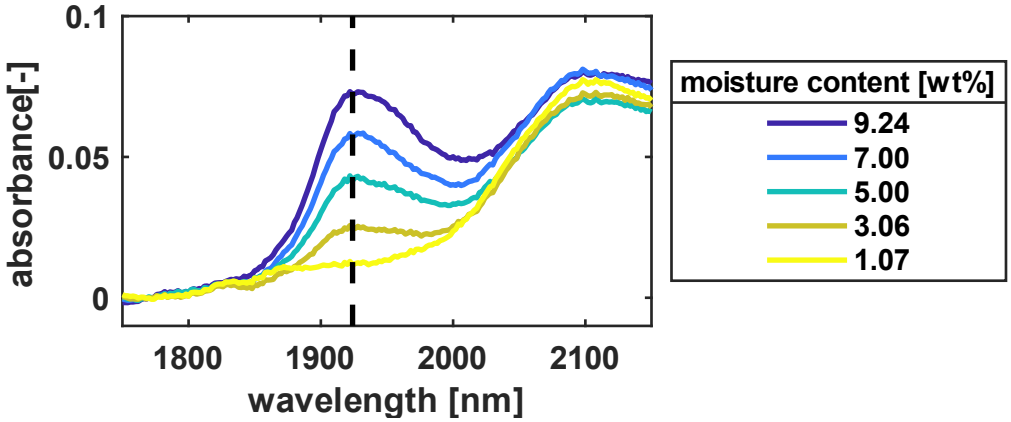

Figure 27: Spectra of Biotex400 with different moisture contents. The water peak at 1922 nm increases with the moisture content.

Comparing the spectra of different NF textiles with similar moisture content can provide an initial indication of whether transferring a PLS model to another NF textile is possible. Figure 28 shows the spectra of the different textiles with roughly 2.2 wt% moisture. The spectra do not show any relevant differences between them. There are slight differences only in the unassigned peak at 2100 nm. Biotex400 shows a slightly lower absorbance here. In contrast, all other samples are almost congruent.

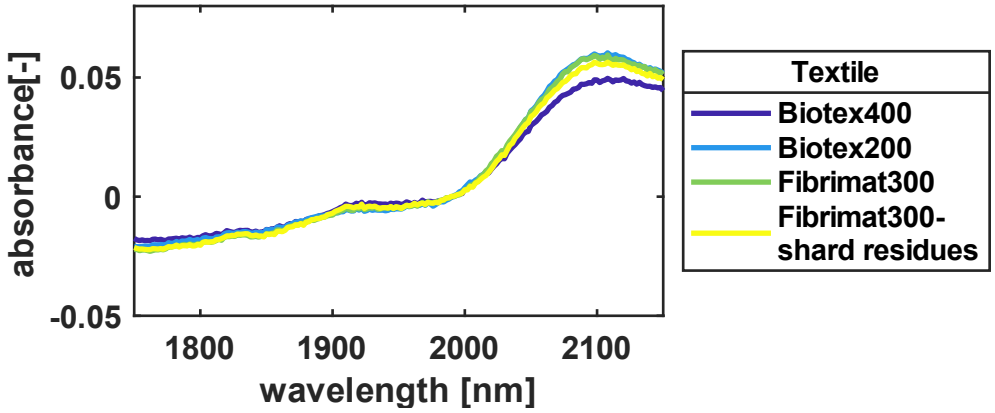

Figure 28: Spectra of different NF textiles with a moisture content of roughly 2.2 wt%.

4.2.1 Differentiating between NF Textiles using PCA

It is attempted made to differentiate between various NF textiles using PCA. This could be interesting both for identifying NF textiles and indicating whether it is possible to distinguish between different batches. Figure 29 shows the scores for PC1 and PC2. The underlying PCA is based on SNV and MC, with PC1 explaining 96.56 % and PC2 1.56 %. PC1 correlates with fiber moisture content, while no correlation was found for PC2. Differentiating between the various textiles using the current PCA model is not possible.

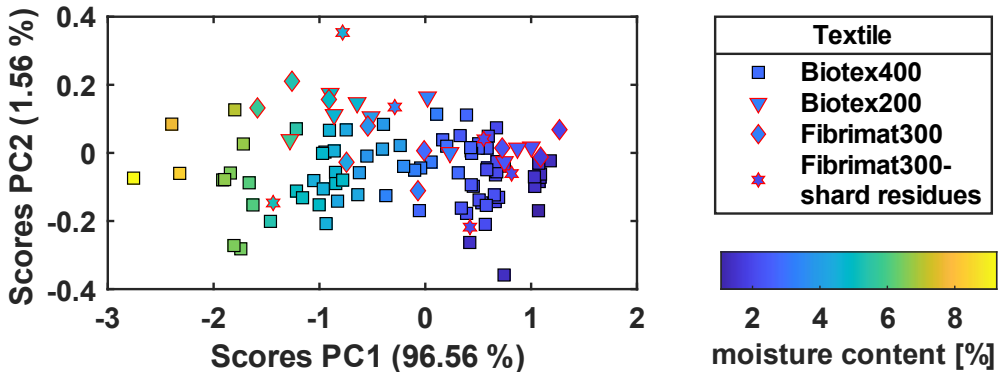

Figure 29: Scores of PC2 over PC1 of from spectra of different textiles.

None of the tested PCA models could distinguish between the NF textiles. Furthermore, the presence of shard residues in Fibrimat300 seems to have no significant impact on the spectra. Once the data were centered, PC1 consistently described moisture content, while higher PCs exhibited no recognizable correlations. This result is consistent with the NIR spectra in Figure 28, as they also show no significant differences between the textiles. Therefore, it seems likely that PLS models could be transferrable between different textiles.

4.2.2 Determining the Moisture Content of NF Textiles

The most significant developed PLS models are shown in Table 7. For MoC-1, only various pre-processings were tested without limiting the wavelength range or excluding outliers. With an r^2CV of 0.979, this model is already very suitable for quantitatively determining the moisture content. Removing the left spectral range up to 1880 nm and removing outliers improves the model and reduces the number of required LVs (MoC-2). All samples from the humidity chamber (moisture conten > 6.7 wt%) and one additional sample were removed as outliers. The

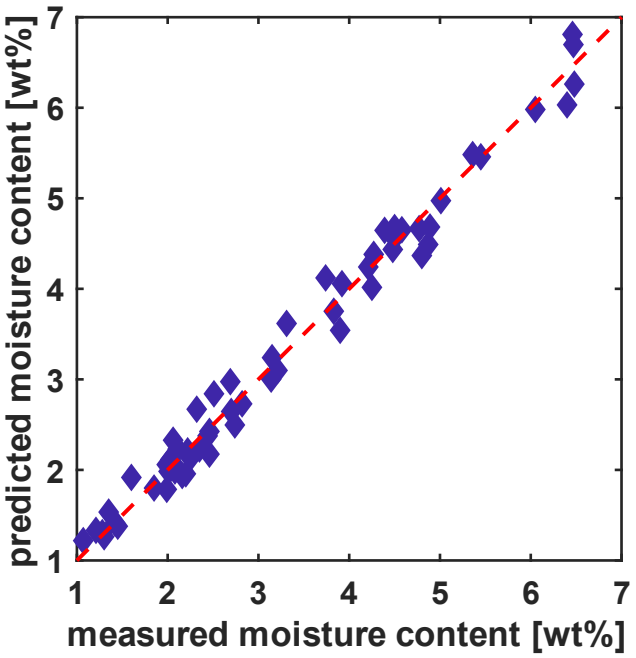

Figure 30: Predicted moisture content from CV of Biotex400 using PLS model MoC-3.

decision to remove the samples from the humidity chamber was made due to their relatively small number, especially considering the wide range, they represented (6.7 – 8.3 wt%). The results of the best model (MoC-3) are shown in Figure 31. The modified preprocessing improves especially the $RMSECV$. This leads to a better stability of the model against unknown data. MoC3 determines the moisture content with an $RMSECV$ of 0.20 wt%. Comparing this with the reference method, for which an error of 0.15 wt% is stated, MoC-3 predicts the moisture content with sufficient accuracy. For the validation of MoC-3, one spectrum with a moisture content over 6.7 wt% was removed from the validation dataset. The validation of MoC-3 with new, unknown spectra from Biotex400 results in an $RMSEP$ of 0.13 wt%. The $RMSEP$ is significantly lower than the $RMSECV$ determined for the model and the measurement accuracy of the reference method (see Figure 31). It is a coincidence, that the validation data fits much better to the PLS model than the calibration data. All measured samples were divided into calibration and validation data by using every fifth sample for validation. Typically, an $RMSEP$ similar to the $RMSECV$, or worse, if the validation data does not fit to the calibration data, would be expected. The r^2P, on the other hand, is minimally worse at 0.971 than the r^2CV at 0.983, and thus within the expected range. The obtained $RMSEP$ can be seen as a curiosity,

but it does not represent the accuracy of the measurement of NIR spectroscopy in the RTM process.

MoC-3 is also tested to predict the moisture content of NF textiles other than Biotex400 (see Figure 31 and Table 7 bottom). The r^2P of 0.974 for Biotex200 or even better for the other textiles allows for all three tested NF textiles to determine the moisture content quantitatively. However, the $RMSEP$ increases significantly, as can be expected. Surprisingly, Biotex200 has the highest $RMSEP$ at 0.40 wt%. At the same time, the shard residues have no negative impact on the $RMSEP$. Instead, they show the lowest $RMSEP$ with 0.32 wt%.

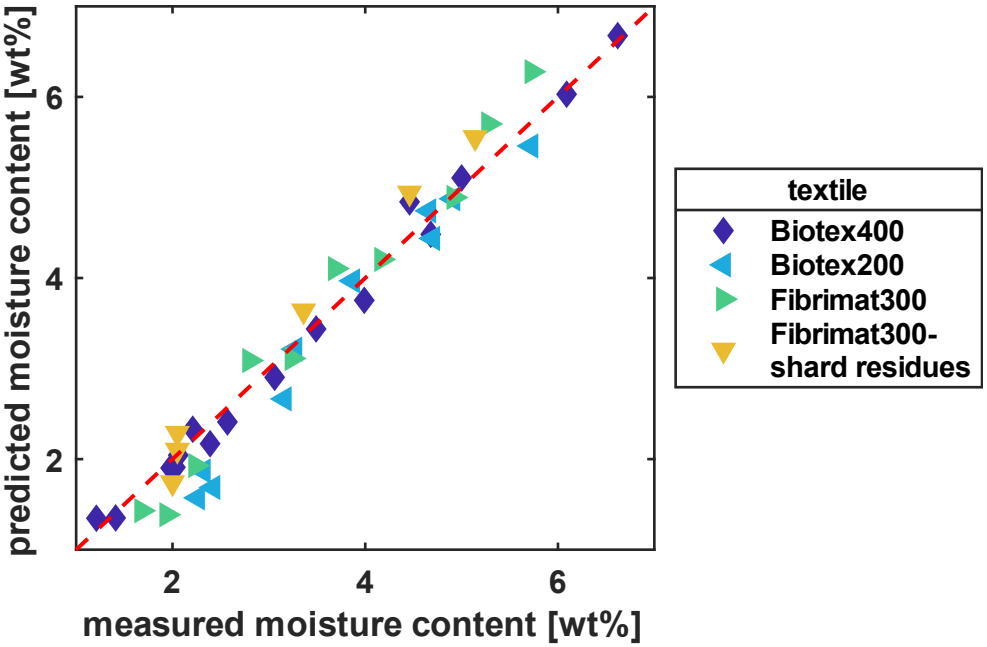

Figure 31: Predicted moisture contents of different NF textiles using MoC-3.

Table 7: Developed PLS models to predicted the moisture content (top) and application of the Model MoC-3 on different NF textiles (bottom).

Model	Outliers	Preprocessing	Wavelength range [nm]	LV	r^2C	r^2CV	$RMSEC$ [wt%]	$RMSECV$ [wt%]
MoC-1	0	SNV, SM, MC	1750-2150	4	0.985	0.979	0.22	0.26
MoC-2	0	SNV, SM, MC	1880-2150	2	0.983	0.981	0.20	0.22
MoC-3	5	SNV, 1.Deriv	1880-2150	2	0.984	0.983	0.19	0.20

Model	Tested material	Preprocessing	Wavelength range [nm]	LV	r^2C	r^2CV	$RMSEC$ [wt%]	$RMSEP$ [wt%]
MoC-3a	Biotex400	SNV, 1.Deriv	1880-2150	2	0.984	0.971	0.19	0.13
MoC-3b	Biotex200	SNV, 1.Deriv	1880-2150	2	0.984	0.974	0.19	0.40
MoC-3c	Fribrimat300	SNV, 1.Deriv	1880-2150	2	0.984	0.981	0.19	0.35
MoC-3d	Fibrimat300 shives residuals	SNV, 1.Deriv	1880-2150	2	0.984	0.989	0.19	0.32

4.3 Discussion

The application of NIR spectroscopy for determining the moisture content in NF textiles has proven to be promising, especially in terms of process control and quality assurance of NF composites.

The spectra show clear differences regarding moisture content but no discernible patterns regarding the different types of NF textiles. This suggests that NIR spectroscopy specifically captures the moisture within the fibers without the type of textile significantly affecting the measurement. Both PCA and PLS results confirm this observation, highlighting NIR spectroscopy's ability to identify moisture differences precisely. The narrow measurement range of the NIRONE S2.2 spectrometer (1750 – 2150 nm) is sufficient to determine the fiber moisture content.

The developed MoC-3 model has proven to be particularly effective for determining fiber moisture content in the RTM process. Due to the high accuracy and reproducibility of measurements with this model, fiber moisture content can be continuously monitored, which is a crucial requirement for producing high-quality NF composites. Therefore, the ability to control the moisture of the fibers directly contributes to quality assurance in the production of natural fiber composites.

The experimental setup demonstrates the feasibility of drying the fibers directly in the closed mold using vacuum. This allows for a flexible moisture content adjustment, either by readjustment or by direct drying in the cavity, making the process more efficient and controlled.

The transferability of the MoC-3 model to other natural fiber textiles shows the stability of the model. The transferability implies that batch variations in Biotex400 should not significantly impact the model. Particularly in research, but also from an application-technical perspective, the transferability is relevant as it eliminates the need for recalibration for each textile. However, the transferability of the model should be critically examined to ensure its suitability and accuracy for different types of textiles.

In summary, using NIR spectroscopy to determine the fiber moisture content in natural fiber textiles is an effective tool for quality assurance and process control in

producing NF composites. The ability to precisely control and adjust the moisture content can significantly improve the quality and performance of the final products.

5 Determining Mixing Ratio of an Epoxy/Amine Resin System

The mixing ratio, e.g., the composition of the polymeric matrix material in a composite of the resin system components, is of crucial importance for composite processing as well as the resulting material properties [94]. Deviations from the prescribed mixing ratio can cause issues during processing, incomplete curing of the composite, or worse mechanical properties. These issues can also result in liability issues in critical applications. For example, in the aerospace industry, some resin systems such as RTM6 are supplied already mixed and frozen to avoid curing, causing much higher costs. Mixing on-site for the manufacturer would be advantageous here.

The issue of the mixing ratio is more crucial to resin system curing by polyaddition reaction, such as epoxy/amine or polyurethanes, than to resin systems curing by chain growth reactions, e.g., polyester resins. In the first case, typically, a stoichiometric mixing ratio between resin and hardener is aimed for, but deviating ratios are also used for some systems. Deviations of the given mixing ratio mean reactive groups for which no reaction partner is present and which are, therefore, weakening the network.

In technical datasheets the mixing ratio is typically provided in parts per mass or volume. This means that to 100 parts resin X parts hardener are added. In the following, the mixing ratio is determined by mass, presented as 100:X (resin:hardener) or the hardener content X, referring to 100 parts of resin is given.

The mixing ratio of two epoxy/amine systems is determined on uncured and cured samples. Once, the mixing ratio is determined on neat resin, whereas in the second case, the mixing ratio is determined in the VARI process.

5.1 Materials and Experimental Methods

5.1.1 Used Material

Neat resin system: The epoxy resin Epikote RIMR135 mixed with the hardener Epikote RIMH1366, both Hexion Inc. (Columbus, United States), is used.

VARI: As resin Epinal FR10.16-A2.01 mixed with Epinal FH10.41 as hardener, both bto Epoxy GmbH (Amstetten, Austria), is used. The used textile is Biotex Flax 400g/m² 2x2 Twill (“Biotex400”, Composites Evolution Ltd., Chesterfield, UK).

5.1.2 Sample Preparation

All mixing ratios are given by weight.

Neat resin system: The resin (50 g) was weighed in a plastic pot, and the amount of hardener (see Table 8) was added. The TDS specified a mixing ratio of 100:30 by weight [95]. The resin system was properly mixed by hand and degassed for 2 min. Afterward, 5 g were weighted into an aluminum pan (cross-section 55 mm).

In total, 24 samples with different mixing ratios were prepared.

Table 8: Weight and content of the hardener (RIMH1366).

Hardener content	24.0	24.75	25.5	26.25	27.0	27.75	28.5	28.8
Hardener weight [g]	12.0	12.4	12.8	13.1	13.5	13.9	14.3	14.4
Hardener content	29.1	29.4	29.7	30.0	30.3	30.6	30.9	31.2
Hardener weight [g]	14.6	14.7	14.9	15	15.2	15.3	15.5	15.6
Hardener content	31.5	32.25	33.0	33.75	34.5	35.25	36	36.15
Hardener weight [g]	15.8	16.1	16,5	16.9	17.3	17.6	18.0	18.1

VARI: The preform was cut to 100×100 mm, and a VARI setup for a line sprue was prepared on a heating plate, using one layer of textile, peel ply and distributor channels, at the front and the end of the preform, under the vacuum bag. The resin (50 g) was weighed in a plastic pot, and the regarding amount of hardener (see Table 9) was added. The specified mixing ratio was 100:30 (resin:hardener). The resin system was properly mixed by hand and degassed for 10 min. Afterwards, the resin was infused within 15 min. The material was cured for 24 h at 55 °C. In total, 19 VARI setups with different mixing ratios were prepared.

Table 9: Weight and ratio of the hardener (FH10.41).

Hardener ratio	27.0	27.2	27.6	28.2	28.5	28.8	29.1	29.4
Hardener weight [g]	13.5	13.6	13.8	14.1	14.3	14.4	14.6	14.7
Hardener ratio	29.8	30	30.2	30.6	30.9	31.2	31.5	31.8
Hardener weight [g]	14.9	15	15.1	15.3	15.5	15.6	15.8	15.9
Hardener ratio	32.4	32.8	33					
Hardener weight [g]	16.2	16.4	16.5					

5.1.3 NIR Measurements

Neat resin system: For the NIR measurements, the NIRONE S1.7 was equipped with a NIR probe (400 µm fiber core, Avantes BV, Apeldoorn, Netherlands). The light came from the light source (Avantes BV, Apeldoorn, Netherlands). For a more detailed description, see Chapter 4. The probe is positioned 5 mm above the sample.

The NIR measurements were done using *Steps* of 2 nm, *PointAvg* of 10, and *ScanAvg* of 5. Three spectra at different positions were measured from each sample.

VARI: NIRONE S1.7 was used as a stand-alone spectrometer for the NIR measurements. Doing so, it is positioned directly on the VARI setup, measuring through the vacuum foil.

The NIR measurements are done using *Steps* of 2 nm, *PointAvg* of 10, and *ScanAvg* of 5, with an internal light source intensity of 100 %.

5.1.4 Statistical Analysis

The weight of the resin and hardener were used as reference values.

Neat resin system: The spectra of each sample were averaged, resulting in 24 spectra for the PLS modeling. Since only 24 samples were available, a split into calibration and validation samples was avoided. The quality of the PLS models is assessed using the r^2CV and $RSMECV$.

VARI: Ten spectra at different positions were measured from each of the 11 samples. As spectra from the same sample differ strongly, averaging spectra was avoided. Since only 11 samples were available, a split into calibration and validation samples was avoided. The quality of the PLS models is assessed using the r^2CV and $RSMECV$.

PLS was done as described in Section 4.1.6. Cross-validation is done by *venation blinds*, using 12 data splits.

5.2 Results

5.2.1 Neat Resin System

Representative spectra measured with the NIRONE S1.7 of different mixing ratios of resin (RIMR135) and hardener (RIMH1336) are presented in Figure 32. Most parts of the spectra, including the shoulder of the epoxy peak (see Chapter 3), do not differ. Only the amine peak (see Table 5) at 1534 nm increases with increasing hardener content.

To determine the mixing ratio of neat resin, PLS models are developed according to Section 4.2.3; relevant models are presented in Table 10. In the first screening, the best results were obtained by using quite a high number of LVs, independent of the preprocessing (see MR-1 and MR-2). The models have good values for r^2C, r^2CV and $RMSEC$ and even the $RMSECV$ is with 0.63 (MR-1) usable order of magnitude. However, the significant difference between $RMSEC$ and $RMSECV$ is

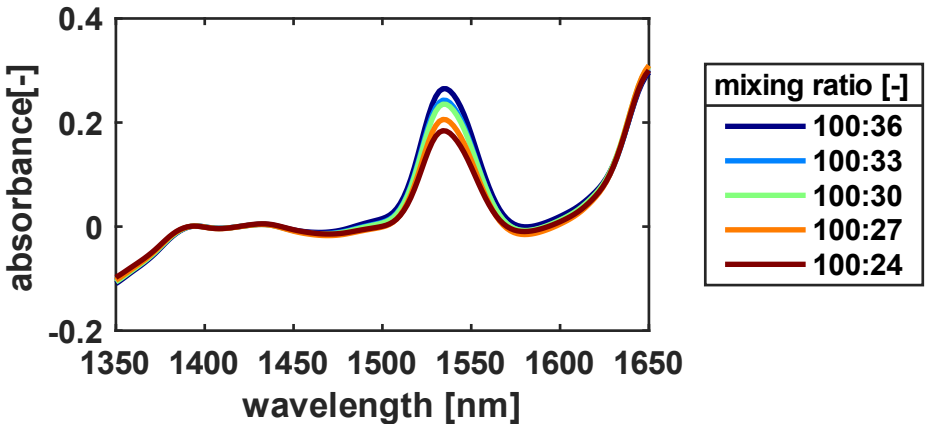

Figure 32: NIR spectra of an epoxy/amine resin system with different mixing ratios of resin and hardener.

that the $RMSECV$ is nearly double the $RSMEC$, which indicates an overfitting of the models. Overfitted models are too well adapted to the calibration data and capture not only the underlying patterns but also noise, which results in poor predictive performance on unknown data. Reducing the number of LVs barely affects the $RMSECV$, whereas r^2C, r^2CV and $RMSEC$ worsen (model MR-1a and MR-2a). Despite the deterioration r^2C, r^2CV and $RMSEC$ and $RMSECV$ of the models have good predictive qualities. The mixing ratios predicted by CV using MR-1 and MR-1b are shown in Figure 33. Reducing the wavelength range used and increasing the smoothing window improved the predictive qualities of MR-1b, especially towards the end borders of the model.

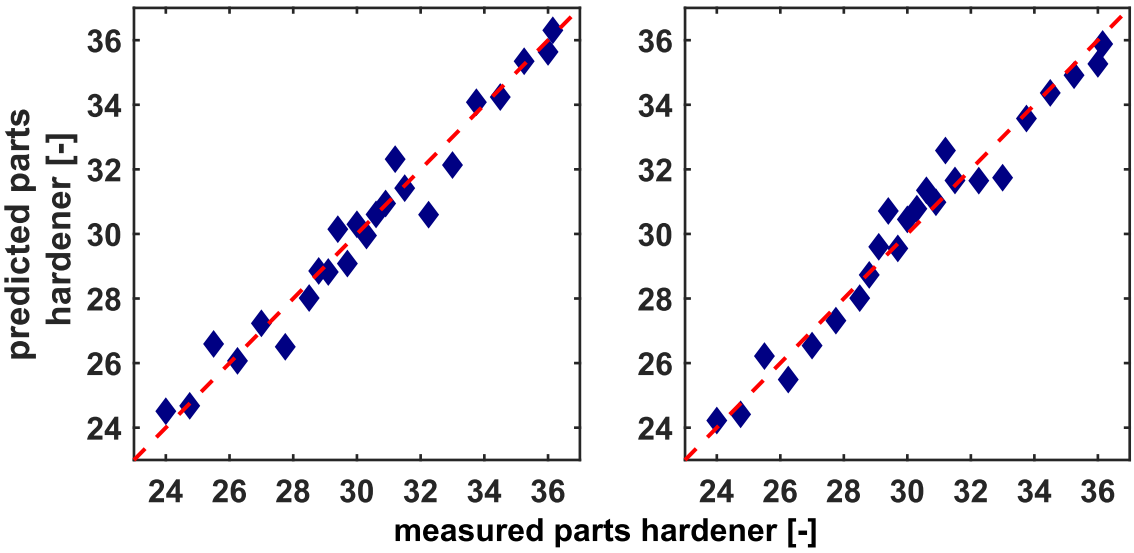

Figure 33: Predicted versus measured parts hardener, applying PLS-model MR-1 (left) and MR-1b (right).

Table 10: Developed PLS models to determine the mixing ratio of an epoxy/amine resin system.

Model	Outliers	Preprocessing	Wavelength range [nm]	LV	r^2C	r^2CV	$RMSEC$ [-]	$RMSECV$ [-]
MR-1	0	1.Deriv	1350-1650	8	0.991	0.965	0.31	0.63
MR-1a	0	1.Deriv	1350-1650	2	0.963	0.963	0.59	0.64
MR-1b	0	1.Deriv (11 pt)	1350-1650	2	0.970	0.966	0.58	0.61
MR-2	0	MC	1350-1650	9	0.990	0.961	0.34	0.66
MR-2a	0	MC	1350-1650	2	0.970	0.956	0.58	0.71

5.2.2 VARI

Representative spectra measured with the NIRONE S1.7 from VARI setups with different mixing ratios of resin (Epinal FR10.16-A2.01) with hardener (Epinal FH10.41) are presented in Figure 34. The setups are measured in an uncured (top) and cured (bottom) state. The spectra of the uncured setups show the characteristic amine peak (1538 nm) and shoulder of the epoxy peak (>1650 nm). Towards lower wavelengths, the absorbance decreases. The edge of this decrease is at a higher wavelength (around 1440 nm) than at the neat resin (compare Figure 32). The amine peak has nearly diminished in the spectra of the cured setup. Only samples with a hardener overshoot show a weak peak at 1538 nm. Also, the epoxy is much weaker but does not diminish. This is due to the overlap with the peak from aromatic C-H at around 1670 nm (see Chapter 3). The hydroxy peak appears at 1484 nm rather broad.

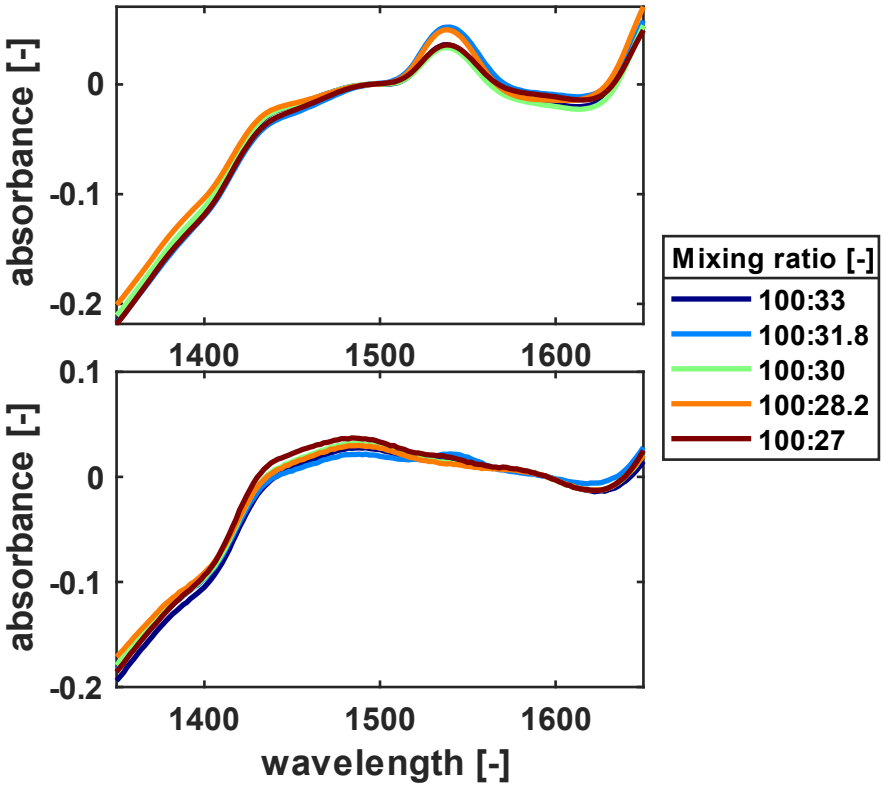

Figure 34: Spectra of different mixing ratios from the uncured (top) and cured (bottom) VARI setup.

In the uncured and cured state, the spectra do not show an apparent mixing ratio depending order, as they did for the neat resin (see Figure 32). The developed PLS

models also reflect the missing apparent trends (see Figure 35, Figure 36, and Table 11). The models tend to overfit due to the small sample number. Therefore, only models with a maximum of 5 LVs are considered. Attempts to improve the model quality after the first screening by limiting the wavelength range or testing further pre-processings were unsuccessful. The removal of outliers was omitted to illustrate the variability of the results. However, even otherwise, based on Cook's distance and leverage, only some of the standalone measurements would have been identified and removed as outliers.

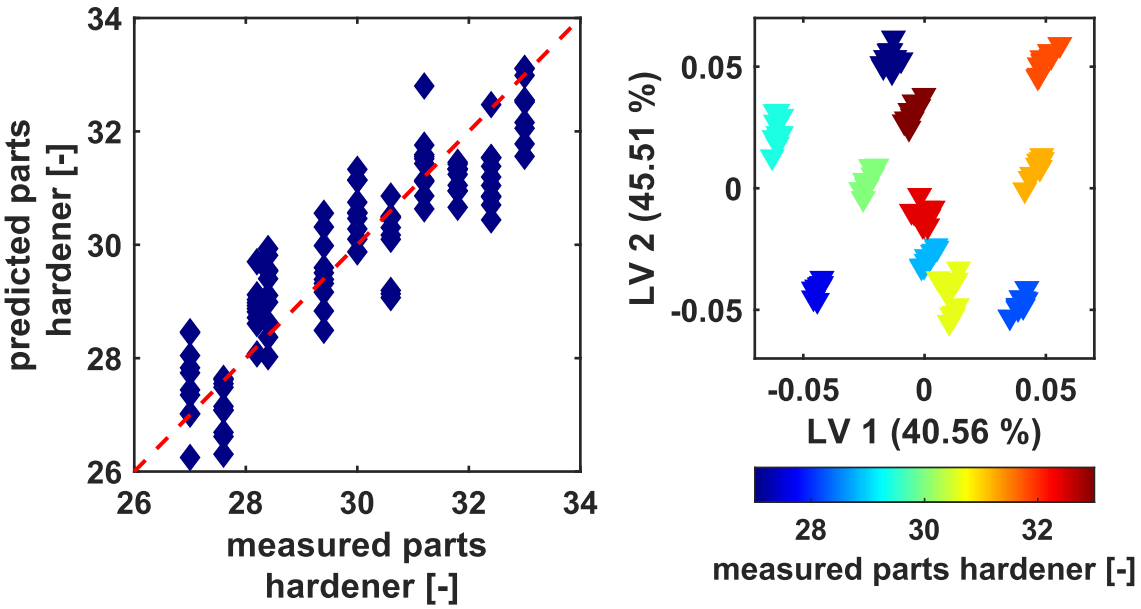

Figure 35: The predicted vs. the measured parts hardener, predicted using model CU-1 hardener content (left) and the scores of the first and second LV of the model (right).

The found models have reasonable values in $RMSEC$ and $RMSECV$, whereby from the cured VARI setup, the mixing ratio can be predicted with better quality. They are already nearly as good as from the neat resin. But all models have values below 0.9 for r^2C and r^2CV, which is the minimum for PLS models used for quantitative predictions by a rule of thumb. For the uncured (see Figure 35) and the cured (see Figure 36) VARI setup, the mixing ratios predicted for each sample scatter over a wide range, roughly 2-5 parts hardener. The first two LVs describe the largest portion of the data in all models. For model CU-1, the second LV describes more variance in the data than the first one due to the fact that the first LV also describes variance in the Y-data, which is not shown here. All samples are distinguishable for

the uncured VARI setup based on the first two LVs. From the cured VARI setup, some samples are superimposed with each other in the first two LVs. Espically, the hardener content of 27 parts scatters and might be difficult to distinguish from the hardener parts 27.6, 30, and 31.2.

With the PLS models presented, quantitative determination of the mixing ratio is impossible. However, a qualitative prediction seems possible if the spectrum of a particular composite has a mixing ratio within a specific range.

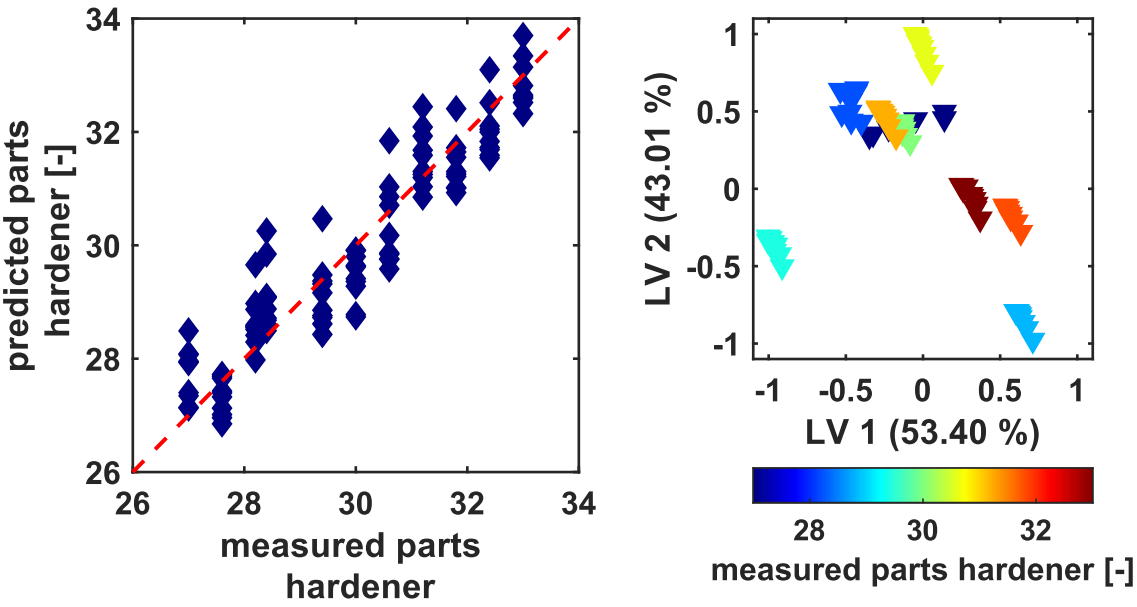

Figure 36: The predicted vs. the measured parts hardener, predicted using model CC-1 hardener content (left) and the scores of the first and second LV of the model (right).

Table 11: Developed PLS models to predict the mixing ratio of epoxy/amine resin system in an uncured (top) and cured (bottom) state**.**

Model	Outliers	Pre-processing	Wavelength range [nm]	LV	r^2C	r^2CV	$RMSEC$ [-]	$RMSECV$ [-]
CU-1	0	SNV, 1.Deriv, MC	1350-1650	5	0.886	0.817	0.65	0.83
CU-2	0	SNV, SM, MC	1350-1650	5	0.793	0.778	0.88	0.91
CU-3	0	SNC, 1.Deriv	1350-1650	5	0.773	0.725	0.92	1.01
CU-4	0	1.Deriv	1350-1650	5	0.763	0.714	0.94	1.03

Model	Outliers	Pre-processing	Wavelength range [nm]	LV	r^2C	r^2CV	$RMSEC$ [-]	$RMSECV$ [-]
CC-1	0	SNV, SM, MC	1350-1650	5	0.897	0.881	0.62	0.66
CC-2	0	SNV, MC	1350-1650	5	0.902	0.881	0.60	0.66
CC-3	0	SNC, 1. Deriv, MC	1350-1650	5	0.882	0.849	0.66	0.75
CC-4	0	SNV	1350-1650	5	0.883	0.799	0.79	0.86

5.3 Discussion

The mixing ratio of epoxy/amine resin systems was determined using the NIRONE S1.7 spectrometer on pure resin system samples and in the VARI process. For the pure resin system samples, PLS models could be developed to quantitatively determine the mixing ratio, whereas, for the VARI, only qualitative statements could be made as to whether the mixing ratio falls within a specific range.

In the measurement range of the S1.7, relevant functional groups (epoxy, amine, and hydroxy) show a peak or at least the shoulder of a peak (see Chapter 3). Thus, the determination of the mixing ratio is based on functional groups involved in the curing reaction. This is advantageous because the peaks, especially the amine peak, are particularly pronounced in the spectra of the NIRONE spectrometer. On the other hand, the initiation of the curing reaction also affects the concentrations of the crucial functional groups. For the resin systems tested, the onset of curing plays a minor role since they either cure very slowly at room temperature (RIMR135/RIMH1366 takes longer than 24 hours) or are heat-curing (Epinal FR10.41 A2.01/FH10.16 is cured at 55 °C for 24 hours). The other NIRONE spectrometer, S2.5, which also shows peaks for all three functional groups within its measurement range, was not available at the time of the measurements.

The model found for the pure resin samples is also based on the ratios of the epoxy and amine peaks since the wavelength range below the amine peak only contains noise and is not considered in the model. This underscores the above points regarding the prominence of the affected peaks. The PLS model MR-1b determines the mixing ratio with an $RMSECV$ of 0.61. Considering that for RIMR 135-based resin systems, a mixing ratio of 100:30±2 is specified [96], the developed model is sufficiently accurate for potential applications. One possible application is determining and monitoring the mixing ratio directly in a dosing and mixing plant. The necessary measurement optics could potentially be further improved through application-optimized design.

The models developed for the measurements on the VARI include the entire wavelength range of the spectrometer. It is somewhat surprising for measurements on the uncured VARI, where a similar measurement range would have been

expected for the neat resin samples. This may be due to the small number of samples and the significant variation within the samples. For cured samples, however, either amine or epoxy groups remain in the composite in non-stoichiometric resin/hardener mixes, reflected in the corresponding peaks. Hence, this information is also helpful in the PLS models for determining the mixing ratio.

The fact that only a qualitative statement can be made during measurements on the VARI and not a quantitative one is due to the significant variation of spectra within each sample. The variation stems from the measurement situation, not from poor mixing. Otherwise, varying degrees of variation would be expected, but this appears relatively constant (see Figure 35 and Figure 36). The variation is likely due to different optical situations. The peel ply and textile underneath create different surface morphologies, leading to different light reflections and absorptions. Likewise, the amount of resin in the measurement volume may change depending on whether a crossing point of the textile (see Figure 25a) is at the measurement spot, resulting in little resin or only a thread or a void, resulting in more resin. These effects are exacerbated by the small measurement spot of the NIRONE spectrometers, estimated at 3 mm. A larger measurement spot should significantly reduce the variation. The measurement spot could be increased using a collecting lens, which would also require adjusting the light source. As a rule of thumb, the size of the measurement spot should be approximately five times the size of the morphological features to average out the effects during the measurement.

The question of whether the mixing ratio could also be determined based on the different concentrations of aliphatic and aromatic methyl groups in the resin and hardener was not addressed.

The developed PLS models and results are promising regarding determining the mixing ratios of resin systems using NIR before and after curing. Based on these findings, applications for monitoring the mixing ratio, for example, directly in dosing and mixing plants, are conceivable. Similarly, using NIR for quality control of finished components is also feasible.

6 Monitoring the Degree of Cure

The degree of cure describes the progress of curing in resin systems, a central aspect of the chemistry and processing of resins. The degree of cure is usually measured by the concentration of functional groups involved in the crosslinking or related parameters such as reaction enthalpy. This parameter is extensively covered in the scientific literature; a search on Google Scholar (may 2024) yields about 3,500,000 entries for "degree of cure" [97].

In the composite industry, however, the degree of cure is typically not monitored during processing. Instead, significantly longer curing times than necessary are used to ensure a certain degree of cure. Determining the degree of cure or a correlated parameter such as gel time only plays a role when a specific degree of cure, but not complete curing, is aimed for in a process step, such as in the production of prepregs.

The use of NIR for monitoring the degree of cure or related parameters has been demonstrated in prepreg production, the determined parameters were e.g, the pre-curing degree, gel time, or soluble resin content [17, 83, 98]. Our studies have also shown the suitability of NIR for quality assurance of prepregs during transport and storage [36]. In the context of LCM processes, NIR was successfully used to monitor the degree of cure in RTM, although with limitations in determining the degree of cure at the beginning of the curing phase, α_0.

The following section analyzes the monitoring of the degree of cure in the VARI process using NIR. Here, the four commercially available NIRONE spectrometers are used to evaluate their potential for monitoring epoxy-amine systems. The required experiments take place under strictly controlled conditions suitable for composite processing. Preliminary experiments are done, measuring the temperature evolution in a VARI setup during infusion and curing. Based on the results from the temperature measurement, only one textile layer is used for calibration, while the PLS models are also tested on VARI setups with six layers. The goal is to capture the initial degree of cure, α_0, and its change over time, and to enable external validations through additional VARI experiments.

6.1 Preliminary Study investigating the Temperature Evolution in VARI

Temperature significantly impacts the processing of resin systems. It crucially influences relevant properties of the resin system, such as viscosity and curing speed. In the VARI process, the temperature distribution is locally dependent on factors such as the distance from the heat source and the infusion point. The objective of these experiments is to develop an understanding of the local temperature evolution during infusion and curing.

Isothermal process control is sought since no inline-capable reference method is available for determining the degree of cure using NIR. The isothermal curing process aims to enable the use of external isothermal reference methods for calibrating the PLS model.

In the VARI process, the resin system is typically infused at room temperature and heats up upon entering a heated mold. At this point, the resin begins to cure significantly. The resin system reaching the outlet, exhibits a distinctly higher degree of cure.

In addition to striving for an isothermal curing process, the position of the NIR measurements on the VARI setup is of particular interest. The measuring position should be as close as possible to the sprue to cover the largest possible process window and minimize the unmeasured portion of the curing. However, by the time the resin front reaches the measuring point, it should also have reached a constant temperature so that no additional thermal effects influence the curing behavior, thus allowing the use of an external isothermal reference method.

6.1.1 Methods

6.1.1.1 Used Materials

The experiements were performed using textile ampliTex 5042 (Bcomp Ltd., Fribourg, Switzerland), a twill 4/4 flax fabric. A rectangular preform (800x350 mm), with six layers, was used.The results were transferred to Hexel 1202 (Hexcel Corporation, Stamford, United States). As preforms (200x350 mm) a single layer and six layers were used.All preforms were cut at 0°, relative to the roll direction.

Epinal IR78.31, as epoxy resin and Epinal IH77.11, an amine hardener, both from bto epoxy GmbH (Amstetten, Austria), were used.

6.1.1.2 VARI Setup

A typical configuration was used for the VARI trials. For the VARI trails with NF this includes a preform, peel ply, flow media, and distribution channels under the vacuum bag (see Figure 37). Before sealing the setup, thermocouples were appropriately positioned. The heating plate was preheated to 60 °C. The resin system was prepared by mixing 1100 g resin with 275 g hardener (mixing ratio 100:25 (resin: hardener) by mass) and degassing it for 4 min. Afterwards the resin was injected within 20 min. A total of two trials with NF were carried out with different positioning of the thermocouples.

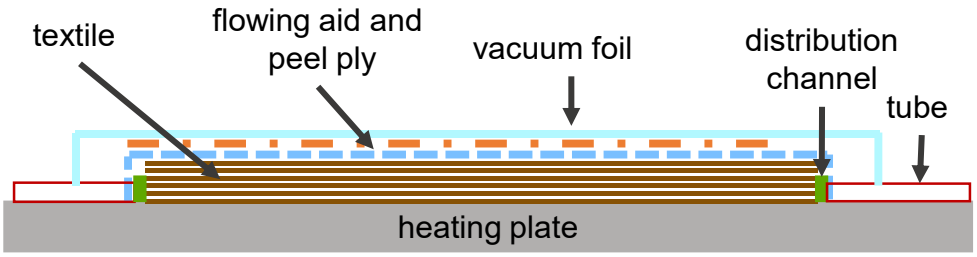

Figure 37: Schematic VARI setup.

The VARI trials with GF were done as described above. Due to changes at the heating plate, the plate was set to 64 °C. Accounting for the smaller preform 200 g resin and 50 g hardener were used. The infusion time was set to 2 min.

6.1.1.3 Temperature Measurement

Thermocouples of type K were used to measure the temperature evolution in VARI. To measure the temperature evolution of the resin flow front along the flow direction, the thermocouples were positioned on the centerline between the 5th and 6th layer of the preform, with the first layer in contact with the heating plate (see Figure 38). To measure the temperature evolution over the composite's thickness, the thermocouples were at a distance of 120 mm between the single textile layers. Transferring the results from NF to GF (Hexel 1202) the thermocouples were placed 25 mm along the center line of the VARI setup in the flowing aid. Temperature measurements were performed for VARI setups with one and six layers of textile

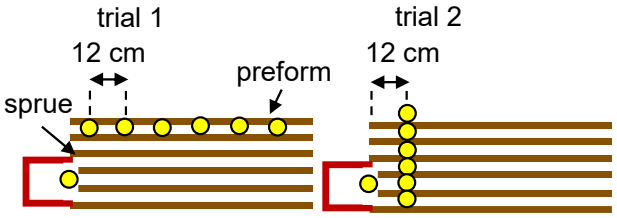

Figure 38: Positions of the thermocouples for the temperature measurements at the NF VARI trials.

6.1.2 Temperature Evolution in VARI Setups using NF

Based on the temperature profile, the different phases of processing from the start of infusion (t = 0 s) can be identified. Figure 39 shows a temperature curve in the preform at a location 20 mm after the inlet. Before the resin system reaches the sensor, the preform has a temperature of 47 °C. The temperature difference towards the heating plate is due to the insulating properties of the natural fiber preform. With arriving of the flow front, the temperature drops to 42 °C. Subsequently, the temperature rises to 44 °C and remains until the end of the injection. This increase is likely due to the improved thermal conductivity of the now saturated preform compared to the dry preform under vacuum. In addition, the resin system flows significantly slower in the preform than in the flow media. At the end of the injection and the start of the curing phase, the temperature in the composite rises sharply and reaches its maximum after about 4100 s. Afterwards, the temperature gradually drops and stabilizes at a constant value (55 °C) after around 8700 s. The rise in temperature is due to two factors. The predominant part results from the

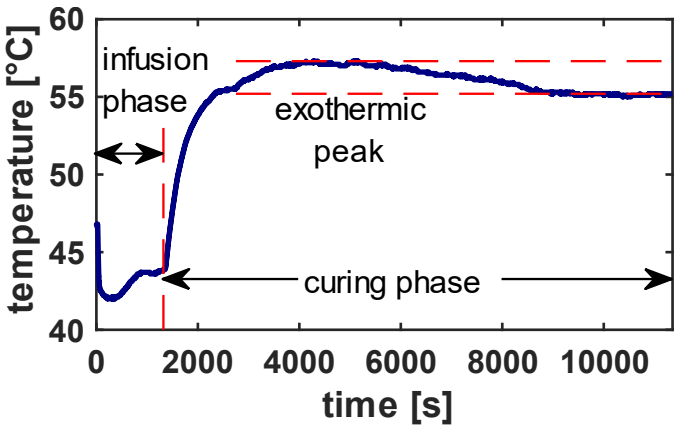

Figure 39: Temperature evolution in VARI after starting the infusion.

temperature of the heating plate. The resin system is no longer flowing, and consequently, it is quickly heated by the heating plate. The second part is the heat released by the exothermic curing of the resin system. As the curing slows down, less heat is released, so the temperature remains constant. This constant level is the temperature ultimately achieved by the heating plate. The difference to the 60 °C set temperature are due the insulating properties of the NF composite.

6.1.2.1 Temperature evolution along the flow front

At the start of the infusion, the temperature at the inlet drops significantly from 47 °C to 18 °C (see Figure 40). Throughout the infusion, it rises to 22 °C. The exothermic curing reaction in the storage container causes this increase. The remaining temperature sensors indicate the arrival of the flow front according to their respective positions. Upon reaching the flow front, the temperature initially drops slightly. This decrease diminishes with increasing flow length, from 5 °C at 12 cm to 1 °C at 48 cm and beyond. After the drop, the temperature rises again to a certain level, which is higher with increasing flow distance. At 12 cm, there is no difference between the dry and the saturated preform. However, at 60 and 72 cm, the temperature reaches 60 °C, corresponding to the heating plate's temperature. These varying temperature levels are related to the thermal history of the resin system. Upon reaching the temperature sensor, the resin comes from the flow aid, and primarily, saturation occurs in the thickness direction. At the same time, the resin also flows forward in the preform, albeit more slowly. As soon as the flow front submerges the temperature sensor, it measures resin that has already been in the preform for some time and has warmed up there. This explains the increasing

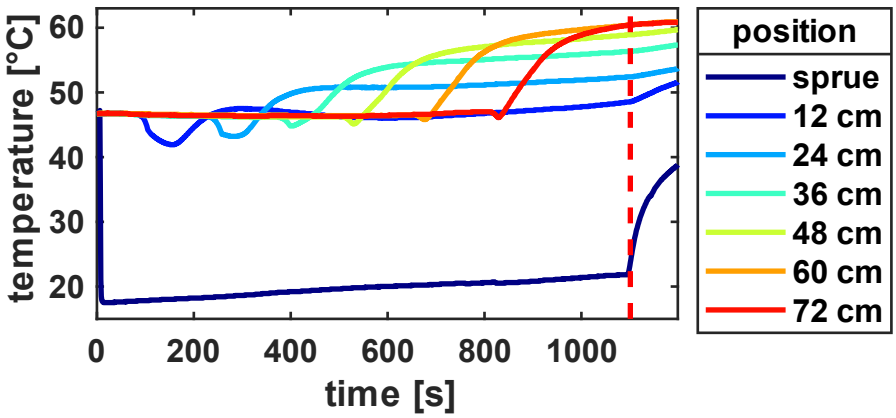

Figure 40: Temperature evolution during the infusion phase. The red, dashed line marks the end of the infusion phase.

temperature levels with increasing distance from the infusion point. The infusion is stopped after 1100 s, and the temperature starts to rise with begin of the curing phase. The rise in temperature is related to the plate's position (see Figure 41). The closer to the beginning of the plate, the more significant the increase. However, the respective measurement positions also have a lower temperature at the start of curing. The temperature probe at 12 cm records a rapid rise to 55 °C, after which the increase significantly weakens. However, it continues to rise to 57 °C, reaching the temperature level of the other temperature probes. The temperature probe at 24 cm also rises to 55 °C but then shows no further increase. This is a measurement error, as it is neither reproducible nor explainable. The other temperature probes initially rise sharply to 59 °C (36 cm) and 61-62 °C (48-72 cm). They then maintain this temperature level for about 10 minutes. The higher temperatures of the further distant measurement positions are probably related to the higher initial levels from the infusion. As the heat development weakens due to curing, they drop to 57 °C. There is no process-technical explanation for the step at 7500 s.

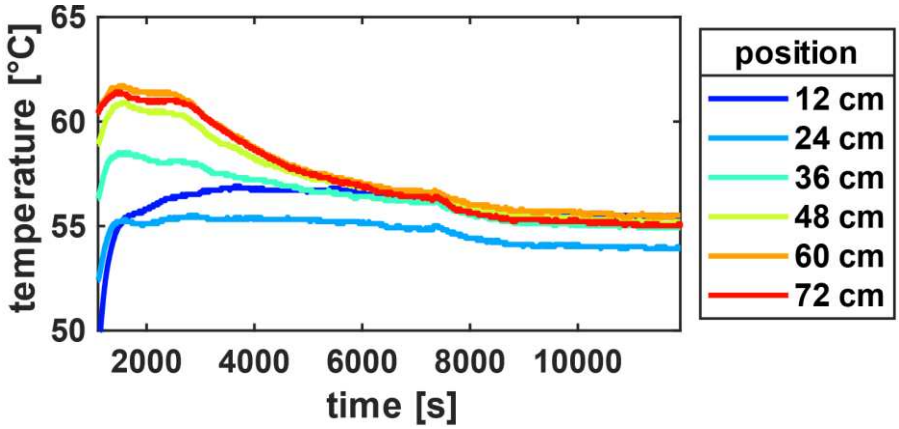

Figure 41: Temperature evolution along the flow direction during curing.

6.1.2.2 Temperature evolution over thickness

The temperature development across the thickness of the preform is measured 12 cm away from the inlet. The previously shown data appear to have the most significant changes here. The fifth layer corresponds to the measurement position of 12 cm in the previous experiment. There are already significant differences between the measurement positions, before the resin reaches the temperature sensors (see Figure 42). The first layer has a temperature of approximately 59 °C, nearly that of the heating plate. As the distance from the heating plate increases, the temperature decreases. In the sixth layer, only 43 °C is measured. However, this is also where the flow front arrives first, as the resin system primarily advances in the flow aid, and saturation mainly occurs in the thickness direction. The lower the temperature sensor, the later the drop-in temperature is measured. There is a 30-second delay between the top (sixth) and bottom (first) layers. The lower the layer the steeper, the temperature drop. At the same time, the temperature does not drop as much. In the sixth layer, the drop is 8 °C, while in the first, it is only 6 °C. This is related to the later arrival time and, thus, the longer time to warm up. Subsequently, the temperature rises again. Initially, the increase is faster the closer the layer is to the heating plate. In the more distant layers, the temperature eventually rises almost linearly throughout the infusion. The lower layers, however, approach 57 °C and maintain this temperature throughout the infusion.

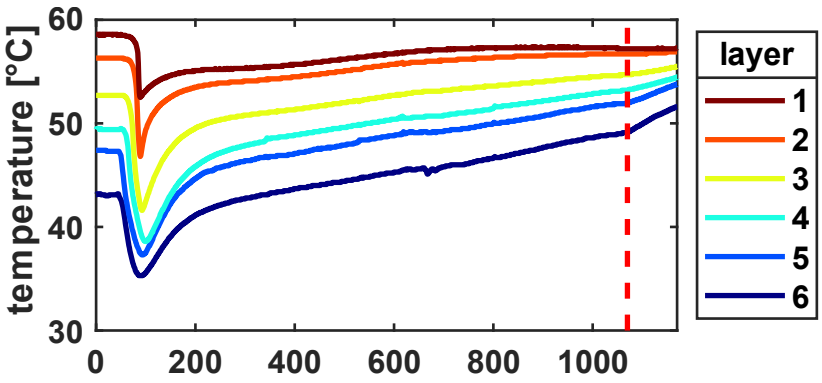

Figure 42: Temperature evolution over thickness of a composite during infusion phase. The red, dashed line marks the end of the infusion phase.

With the start of the curing phase, the temperature rises at all locations. The increase is more substantial with increasing distance from the heating plate (see Figure 43). But the maximum temperature reached decreases with increasing distance from the heating plate. The upper four layers reach their maximum

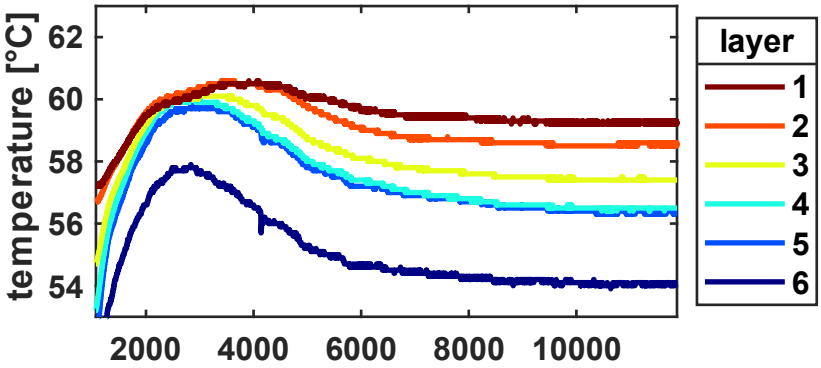

Figure 43: Temperature evolution over thickness of a composite during curing phase.

temperature after about 2700 s whereas the two bottommost layers reach their temperature peak after 4000 s. The exothermicity of the curing reaction significantly impacts the temperature profile, the effect increases with the distance of the measurement point from the heating plate. The subsequent temperature drop is more substantial the further the layer is from the heating plate. The resulting temperature level also decreases with the distance to the heating plate, dropping from 59 °C for the bottommost layer to 54 °C for the topmost layer. The differences in the temperature levels reached are due to the low thermal conductivity of the NF-composite.

6.1.3 Temperature Evolution in VARI Setups using GF

Based on the results of the last section, the temperature is monitored for a single-layer and a six-layer VARI setup. The temperature during infusion and curing is shown in Figure 44. Both the single-layer and six-layer setups exhibit the expected temperature profile during infusion. Upon the arrival of the flow front, the temperature changes. At the first two measurement positions, it initially drops. From 75 mm onwards, the resin system has reached or even exceeded the temperature of the surrounding setup. Here, the temperature rises slightly and suddenly, then remains constant at 57 to 58 °C. In the six-layer setup, the flow front progresses

more slowly, resulting in a later and less steep temperature increase at the thermocouples. Nevertheless, the 120 seconds are sufficient for a complete filling of the VARI setup.

The temperature remains largely constant during curing (Figure 42b and d). Only at the beginning of curing does the temperature fluctuate slightly. The thermocouples that had not reached the temperature level of the other thermocouples during infusion caught up during this time frame. In the single-layer setup, the initial fluctuation is likely due to the heating plate adjusting to the infusion of cold resin. The differences between thermocouples show no dependency on their position, suggesting that they are more related to the sensitivity of the thermocouples rather than to process fluctuations. The fluctuations within a single thermocouple are significantly larger in the six-layer setup than in the single-layer setup. Ignoring the first 300 seconds, the standard deviations in the six-layer setup range from 0.2 to 0.4 °C, compared to 0.1 to 0.2 °C in the single-layer setup. There is no apparent process-related reason for these deviations. In this timeframe, the average temperature in the single-layer setup is 57.8±0.4 °C, while in the six-layer setup it is 57.2±0.6 °C. The lower temperature in the six-layer setup is expected due to the higher number of layers. Compared to NF, this drop is very moderate. Considering the standard deviation, it is at the edge of measurement accuracy.

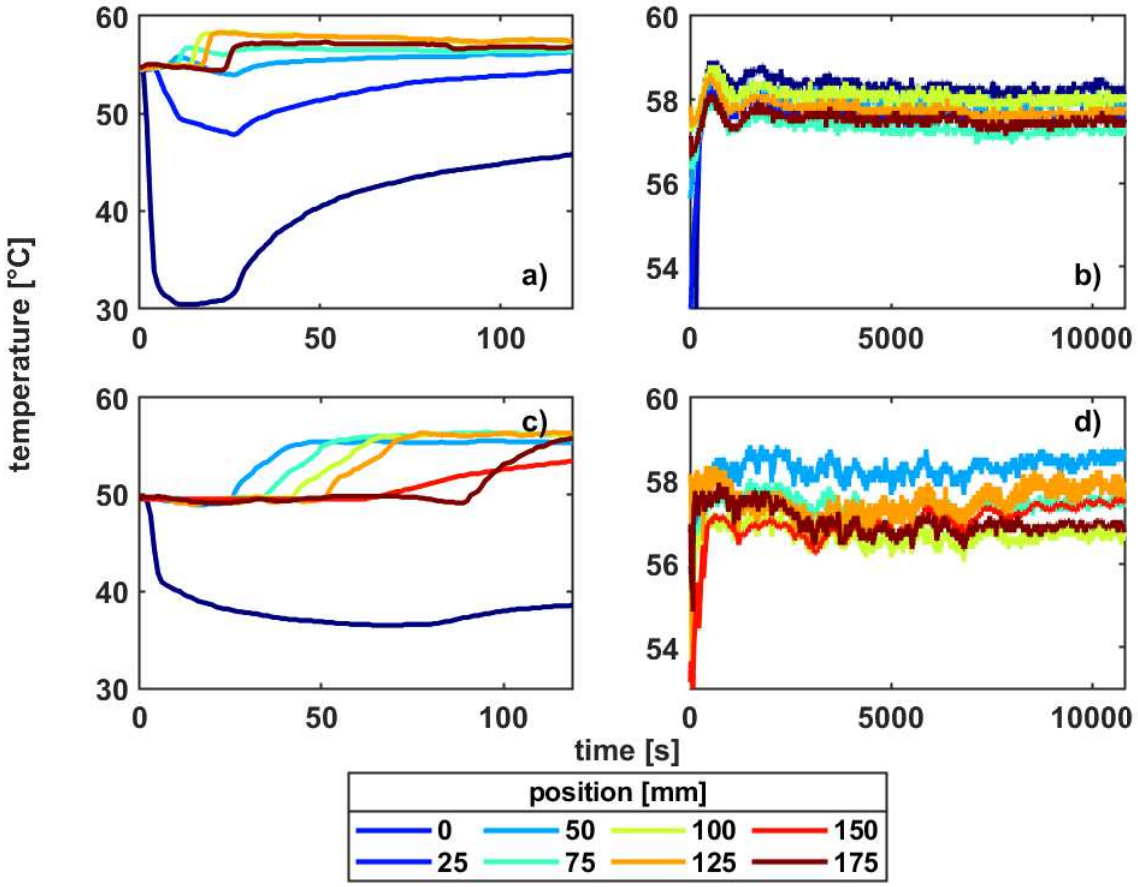

Figure 44: Temperature during infusion (a, c) and curing (b, d) in VARI with one (a, b) or six (c, d) textile layers.

6.1.4 Discussion

The temperature profile in the VARI with NF composites was measured along the flow direction and thickness of the composite. During the infusion, a constant resin temperature of the flow front was measured from 48 cm flow length onwards. From this position, the temperature sensors also showed only very minor differences among themselves throughout the experiment. The measurement across the thickness showed that the temperature change was smaller the closer it was measured with respect to the heating plate. The exothermy caused only a minor warming during curing.

The differences in temperature profiles across the thickness are due to the low thermal conductivity of NF composites, which at 0.2-0.3 W/mK [99, 100] is significantly lower than that of GF composites, for example, which is about

0.6 W/mK [101]. CF composites are even higher thermal conductivity [102, 103]. It should be noted that these values are rough guidelines, as many factors, including fiber volume content, textile structure, fillers, etc., influence the thermal conductivity. The low thermal conductivity causes the temperature values measured at the beginning and the end of the VARI trial. At the same time, it is also responsible for the increasing temperature due to the exothermy. Since the composite does not dissipate heat well, it builds up as a kind of "wave" across the thickness of the composite and consequently increases with each layer. The first effect here is stronger than the second, so there can be no exothermic accidents, at least with the combination of the tested materials.

In the VARI setups using GF the described effects are much smaller. Overall, a single-layer setup can achieve almost isothermal curing. This makes isothermal DSC measurements suitable as a reference method, provided that samples can be extracted after infusion. At the same time, using only one layer shortens the infusion time, as less resin is needed to fill the VARI setup.

The distance from the infusion point for placing the spectrometers should be sufficient. In case of the current setup this is 100 mm.

6.2 Materials and Experimental Methods

6.2.1 Used Material

As resin Epinal IR78.31 with Epinal IH77.11 as hardener, both bto Epoxy GmbH (Amstetten, Austria), is used. The used textile is HexForce 01202（Hexcel Corporation, Stamford, United States）.

6.2.2 VARI

The VARI setups were prepared according to Section 6.1.1.2. The textile dimensions were 200x350 mm. The heating plate temperature was set to 64 °C to achieve a temperature near 60 °C in the VARI setup. The increase was necessary due to changes on the heating plate between the presented here trials and those Section 6.1.1.2, which resulted in a worse temperature transfer into the VARI setup.

A timer was used during resin system preparation and infusion to ensure highly reproducible experimental conditions. Resin (200 g) and hardener (50 g) were weighed into separate pots. The deviations from the nominal weight were below 0.2 g. When the hardener was added to the resin, the timer was started. The resin system was mixed for exactly 120 s by hand and subsequently degassed for 180 s. A further 120 s were scheduled for handling between the steps and for preparing the infusion. Summing up to 420 s after adding the hardener, the infusion was started, lasting for another 120 s. Afterward, the vent at the outlet tube was closed, and the curing phase started.

6.2.3 Reference Measurements

The reference values for the degree of cure are determined by DSC (α_{DSC}) oriented at ISO 11357-5 (curing enthalpy), using DSC1 (Mettler Toledo GmbH, Schwerzenbach, Switzerland). The samples were weighed into a 40-µL aluminum crucible (10 ± 1 mg). All measurements were conducted under nitrogen atmosphere with a 50 mL/min gas flow.

The isothermal measurements were performed at the temperature of the VARI setup during curing (see Section 6.1) at 57.8 °C for 180 min. Afterwards a dynamical DSC was done to determine the remaining enthalpy (H_{cured}). The dynamical measurements were performed between -50 and 250 °C with a 10 K/min heating rate.

Samples of the resin system were taken along the VARI process preparation and quenched in liquid nitrogen to avoid further curing. A first sample was taken before infusion to determine the degree of cure after the resin preparation. From a new VARI setup, a 15 mm broad stripe over the entire width of the setup was cut out at 100 mm. With a razor blade, the resin system was wiped off. These samples were used to determine the degree of cure after infusion and for the isothermal DSC measurement. Additionally, a sample with a completely fresh resin system mixed only shortly was measured.

Using the Star-e Software α_{DSC} was obtained from the DSC measurements. From the dynamical DSC runs the curing enthalpy of the fresh resin H_0, the curing enthalpy before infusion (H_{inf}), the curing enthalpy after infusion at the measuring

spot of the spectrometers ($H_{uncured}$), and the curing enthalpy after curing 180 min (H_{cured}) are determined. They are used to calculate α at the regarding points. The degree of cure over time (α_{DSC}/dt) is calculated from the isothermal measurement, using the right horizontal line as the base line. Afterwards it was scaled towards the regarding window of α, between 12 % ($\alpha_{DSC,\ uncured}$) and 90 % ($\alpha_{DSC,\ cured}$).

6.2.4 NIR Measurements

The spectrometers were positioned 100 mm after the infusion edge directly on the vacuum foil, as the flow front temperature was already constant there. All four spectrometers measured over their full wavelength range, with *Steps* of 5 nm, 50 *Scans*, and 100 *Points*. The measurements were started before preparing the resin system.

6.2.5 Data Evaluation

In total, spectra were recorded from 14 VARI experiments with a single textile layer. However, due to measurement issues, complete data sets were not available for all four spectrometers. An overview of the available data and the extent of the data sets is provided in Table 12. The difference in the spectra per trial resulted from different covered wavelength ranges of the spectrometer and, therefore, longer measuring times per spectrum and differences in the largest step in α between two measurements. If data recording stopped during the curing process, those data sets were discarded to prevent overrepresenting lower degrees of cure in the PLS models. For each spectrum, the corresponding α was calculated based on $\alpha_{DSC}/\mathrm{d}t$. To avoid overrepresenting higher degrees of cure in the PLS models, the largest change in α between two NIR measurements was identified. This change was used as the step size to obtain data sets with an approximately equidistant spectra distribution according to α rather than the measurement time. Three trials were used for validation for each spectrometer; the remaining trials were used for calibration.The six-layer VARI setup was measured once with NIR, and the spectra were treated as described above.

PLS was done as described in Section 4.1.6. As each VARI trial contributes several spectra to the regression, *continuous blocks* was used as cross-validation method. Each block contained the spectra of one trial.

Table 12: Information about the datasets used for developing the PLS models.

Spectrometer	Valid VARI trials	Spectra per VARI trial	Spectra for calibration	Spectra in validation
S1.7	13	218	2140	674
S2.0	12	152-187	1554	526
S2.2	12	152-174	1530	522
S2.5	12	146-164	1416	472

6.3 Results

6.3.1 Determination of the Degree of Cure by DSC measurements

A combination of isothermal and dynamic DSC measurements is necessary to determine the progression of the curing process using DSC. The isothermal DSC measures the progression of the degree of cure, while the dynamic DSC measurements are used to determine the achieved conversion at specific time points. The relevant reaction enthalpies are H_0, H_{inf} and H_{cured}. Based on these, the degrees of cure α_{inf} and α_{cured} can be calculated using Equation (13).

$$\alpha(t) = 1 - \frac{\mathrm{H(t)}}{H_0} \tag{13}$$

The measurements were conducted for both the single-layer and six-layer setups. The determined enthalpies and resulting conversions are given in Table 13. A degree of cure above 90 % cannot be achieved under the given curing conditions. The temperature difference due to the different number of layers is so small that it only affects α_{inf} and α_{cured} below the measurement accuracy. However, a difference in α is observed due to the temperature difference during curing (see Figure 45). The degrees of cure for both the single-layer and six-layer setups initially

Table 13: Curing enthalpy and regarding degree of cure.

Sampling time	Single-layered ($T = 57.8\,°C$)		Six-layered ($T = 57.2\,°C$)	
	H [W/g]	α [%]	H [W/g]	α [%]
t_0	442	0	417	0
t_{inf}	388	12	367	12
t_{cured}	46	90	40	90

increase rapidly and then slow down over time. At 57.2°C, α increases slightly slower than at 57.8°C. The differences are, as expected, minimal, with both curing temperatures reaching a degree of cure of 90 % within 180 minutes.

The isothermally determined degrees of cure now allow assigning a degree of cure to the measured spectra based on their timestamp.

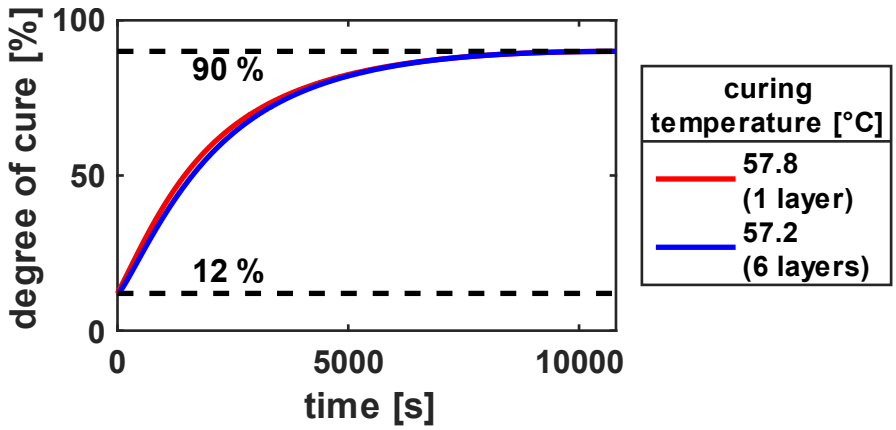

Figure 45: Evolution of the degree of cure of one-layered (57.8 °C) and six-layered (57.2 °C) VARI setups.

6.3.2 NIR Spectra during Curing in VARI

Figure 46 shows the changes in the spectra during the curing process. The spectra from all four NIRONE spectrometers exhibit significant changes during curing. The spectra from the NIRONE S1.7 display a noticeable decrease in the amine peaks (1540 nm) and a slight decrease at the shoulder of the epoxy peaks (>1650 nm), while the hydroxyl peak (1435 nm) increases significantly. In the range of the NIRONE S2.0, the shoulder of the amine peaks (<1550 nm) is still visible. The epoxy peak (1715 nm) is shifted to higher wavelengths compared to the literature (see Chapters 2.6.3 and 3). The NIRONE S2.2 shows the shoulder of the decreasing epoxy peaks (<1750 nm) and a decrease in the water peak (1920 nm) as well as the amine peaks (2040 nm). The origin of the water is unclear; most likely, it is consumed during the curing process, and the peak decreases over curing.

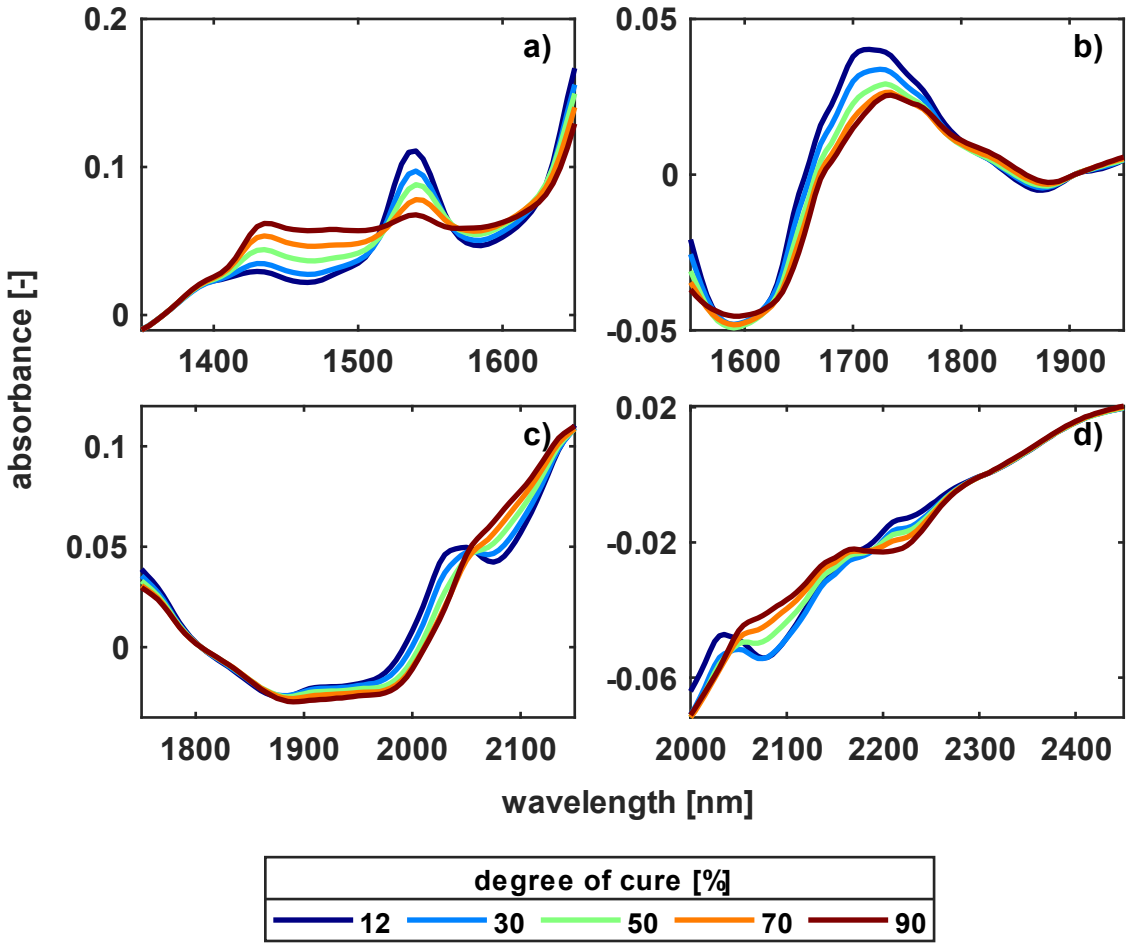

Figure 46: Spectra of the single-layered VARI setup at different degrees of cure measured with different NIRONE spectrometer (S1.7: a, S2.0: b, S2.2: c and S2.5: d).

Compared to Chapter 3, the change in the spectrum due to the hydroxyl peak (2090 nm) is also visible, although it appears only as a shoulder. Without the hydroxyl peak in this region, the absorbance at 90% should be lower than at 12%. The spectra from the NIRONE S2.5 show a decrease in the amine peaks (2035 nm) and an increase in the hydroxyl peaks (2075 nm). The hydroxyl peak appears broad again and is identifiable only by comparing spectra with and without it (e.g., 90% vs. 12%). At 2215 nm, the peak of the epoxy-methylene combination vibration is recognizable. At higher wavelengths, the spectra show no further differences.

The spectra of the six-layer setup fundamentally exhibit the same structure as the spectra of the single-layer setup in both the uncured and cured states (see Figure 47). However, at lower wavelengths, the contours of the spectra for the six-layer setup appear more pronounced compared to the single-layer setup. Conversely, at higher wavelengths, this trend seems to reverse. This is particularly evident in the

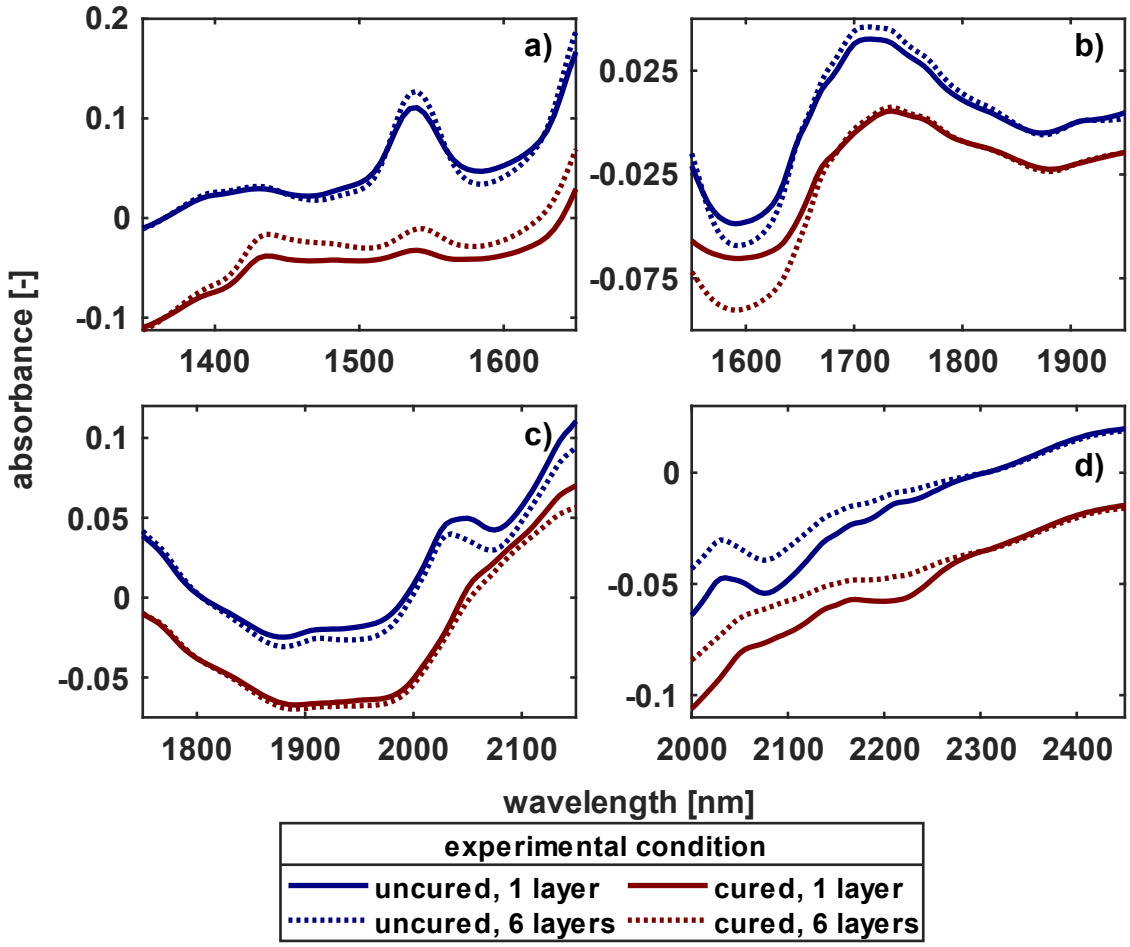

Figure 47: Spectra of the single-layered and six-layered VARI setup measured with different NIRONE-Spectrometers (S1.7: a, S2.0: b, S2.2: c and S2.5: d).

measurement range of the NIRONE S2.5. Small peaks blend with their surroundings, resulting in the spectrum of the six-layer setup appearing significantly smoother than that of the single-layer setup. These effects are likely related to the penetration depth of the light. As the wavelength increases, the light penetrates less deeply into the medium. In the current measurement case, this could mean that fewer details, particularly from the peel ply, are detected at higher wavelengths (NIRONE S2.2 and S2.5). It is unclear at this stage how these differences will impact the PLS models.

6.3.3 Predicting the Degree of Cure by PLS

With all four NIRONE spectrometers, it is possible to monitor the degree of cure throughout the entire curing process of the resin system. A selection of the developed PLS models is shown in Table 14. All models have r^2 values very close to 1, indicating they describe a large proportion of the variance in the data and are suitable for the quantitative determination of the degree of cure, α_{NIR}. But the slight difference in r^2 also reduce the meaningfulness when comparing different models. In terms of r^2 all models would allow to determine α_{NIR}, why r^2 is not further discussed in the following.

The PLS model for the NIRONE S1.7 (S17-1) can be improved primarily by reducing the wavelength range to 1495-1650 nm. This removes the wavelength range not affected by the curing reaction and the region of the hydroxy peak (see Figure 46). This reduction mainly decreases the number of necessary LV and the $RMSECV$, while the $RMSEC$ increases slightly. This divergence in the behavior of $RMSECV$ and $RMSEC$ suggests that the PLS model S17-1a is more stable against information not included in the model. Nevertheless, the S17-1a model is significantly worse regarding $RMSECV$ compared to the models of the other spectrometers. For the models for the S2.0 spectrometer, it is notable that Orthogonal Signal Correction (OSC) reduces the number of LVs from 5 to 1 while simultaneously decreasing $RMSEC$ and $RMSECV$. The use of OSC also leads to similar improvements in the NIRONE S2.5, although not to the same extent. The best models found for each spectrometer are S17-1a (NRIONE S1.7), S20-2a (NRIONE S2.0), S22-2 (NRIONE S2.2), and S25-2a (NRIONE S2.5).

Table 14: PLS models to predict the degree of cure with different NIRONE spectrometers. The underline models are best one found for each spectrometer.

Model	Outliers	Pre-processing	Wavelength range [nm]	LV	r^2C	r^2CV	$RMSEC$ [%]	$RMSECV$ [%]
S17-1	0	SNV, 2.Deriv, MC	1350-1650	5	0.986	0.971	2.7	3.8
S17-1a	98	SNV, 2.Deriv, MC	1495-1650	4	0.982	0.978	2.9	3.2
S20-1	0	SNV, 1.Deriv, MC	1550-1950	5	0.994	0.996	1.4	1.8
S20-2	0	SNV, 1.Deriv, OSC, MC	1550-1950	1	0.998	0.995	1.1	1.6
S20-2a	24	SNV, 1.Deriv, OSC, MC	1550-1950	1	0.998	0.995	1.0	1.5
S22-1	0	1.Deriv	1750-2150	4	0.994	0.993	1.7	1.9
S22-2	0	1.Deriv, MMS	1750-2150	4	0.995	0.994	1.5	1.7
S25-1	0	SNV, 2.Deriv	2000-2450	5	0.995	0.993	1.6	1.9
S25-2	0	SNV, 2.Deriv., OSC	2000-2450	3	0.997	0.993	1.2	1.9
S25-2a	0	SNV, 2.Deriv., OSC	2000-2320	3	0.997	0.993	1.2	1.8

When examining the accuracy over the degree of cure, it is evident that more significant deviations occur at the model boundaries, particularly at the upper limit (90%). Figure 48 shows every 10th predicted vs. measured value of one trial measured with the NIRONE S2.0 spectrometer and the Cook's distance of all the spectra used in the experiment as a function of the degree of cure. Cook's distance is the only parameter in the error analysis that shows these substantial deviations; other parameters, such as leverage, do not show these apparent anomalies for the data presented.

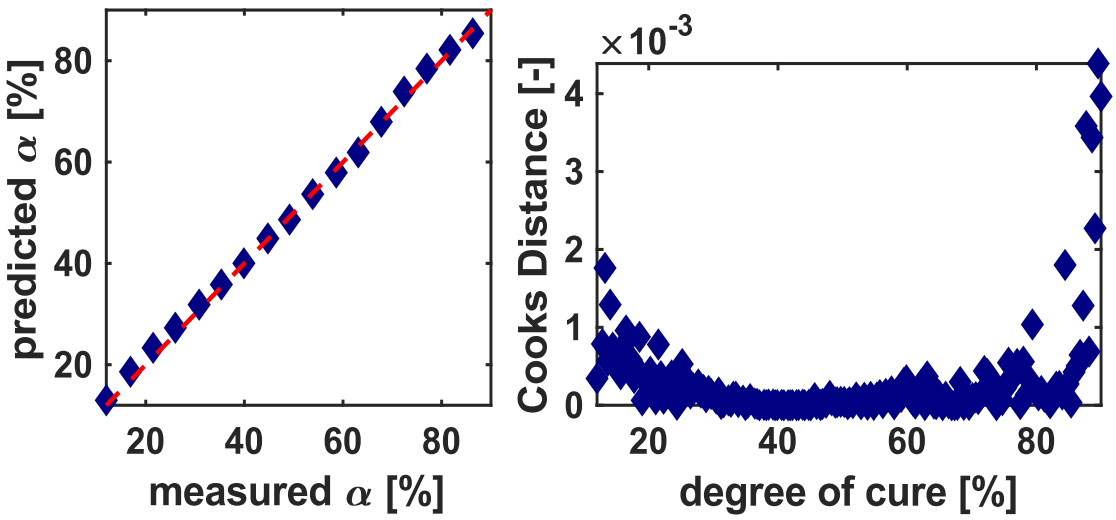

Figure 48: The predicted versus the measured **α** (left, only every 10th values displayed) and the Cooks Distances of the whole trial (right), measured with NIRONE S2.2.

The validation of the best models (see Table 15) is based on three randomly selected VARI experiments. For the NIRONE S1.7, one of these experiments was identified as an outlier based on Student's residuals and Cook's distance and was excluded from the evaluation. In the third experiment of the NIRONE S2.0, data recording ended prematurely. However, according to isothermal DSC, a conversion of over 85% was still achieved during the recording, so the experiment was not excluded in advance. The comparison of the conversion determined by NIR with that determined by DSC (see Figure 49) reflects the results from Table 15. The measurements of the NIRONE S1.7 deviate increasingly from the reference measurement from about 80 % onwards, which also explains the larger $RMSEP$. During validation, the models for the NIRONE S1.7 already showed the worst

parameters. In the NIRONE S2.0, the prematurely terminated measurement (third experiment) deviates mainly from the reference values. Removing this measurement would improve the model's quality parameters, but the criteria for outlier analysis are not overly conspicuous. For the NIRONE S2.2 and S2.5 spectrometers, the determined conversion curves are close to each other and to the reference curve, which is reflected in the good $RMSEP$s.

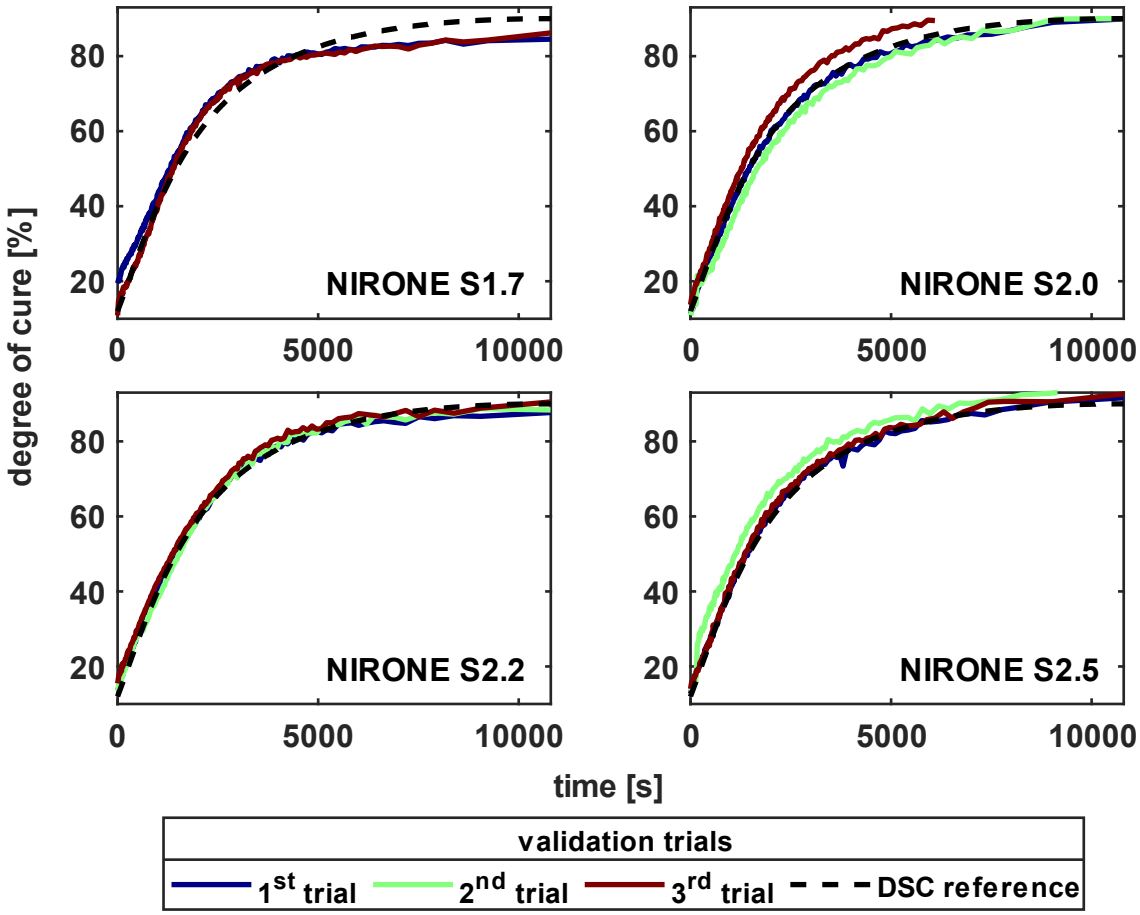

Figure 49: Degree of cure predicted by the different spectrometers.

Table 15: Validation results to predict the degree of cure.

Model	Pre-processing	Wavelength range [nm]	LV	1 layer		6 layers	
				r^2P	$RSMEP$ [%]	r^2P	$RSMEP$ [%]
S17-1a	SNV, 2.Deriv, MC	1495-1650	4	0.98	3.2	0.99	6.3
S20-2a	SNV, 1.Deriv, OSC, MC	1550-1950	1	0.98	2.6	1.00	6.8
S22-2	1.Deriv, MMS	1750-2150	4	1.00	1.9	0.98	4.6
S25-2a	SNV, 2.Deriv, OSC	2000-2320	3	1.00	1.5	0.98	6.5

6.4 Application of PLS Models to a Thicker Layer Build-Up

To evaluate the broader applicability of the best PLS models identified for each spectrometer, the degree of cure for a 6-layer VARI setup was predicted using the PLS models developed. The results are presented in Table 15 and Figure 50. The $RMSEP$ for the 6-layer setup is approximately two to four times larger than the $RMSEP$ for the single-layer VARI setups. Consequently, the r^2P decreases slightly but remains above 0.977, allowing for a quantitative determination of α. As a general rule for qualitative value determination, an r^2 value of around 0.9 is considered acceptable, as discussed in Chapter 2.

The data from the NIRONE S1.7 and S2.5 initially show good agreement; however, they significantly overestimate α from about 40% onwards. For the NIRONE S1.7, the progression in α resembles that in the single-layer setup. However, the initial increase is even steeper, causing the predicted values to align with the measured

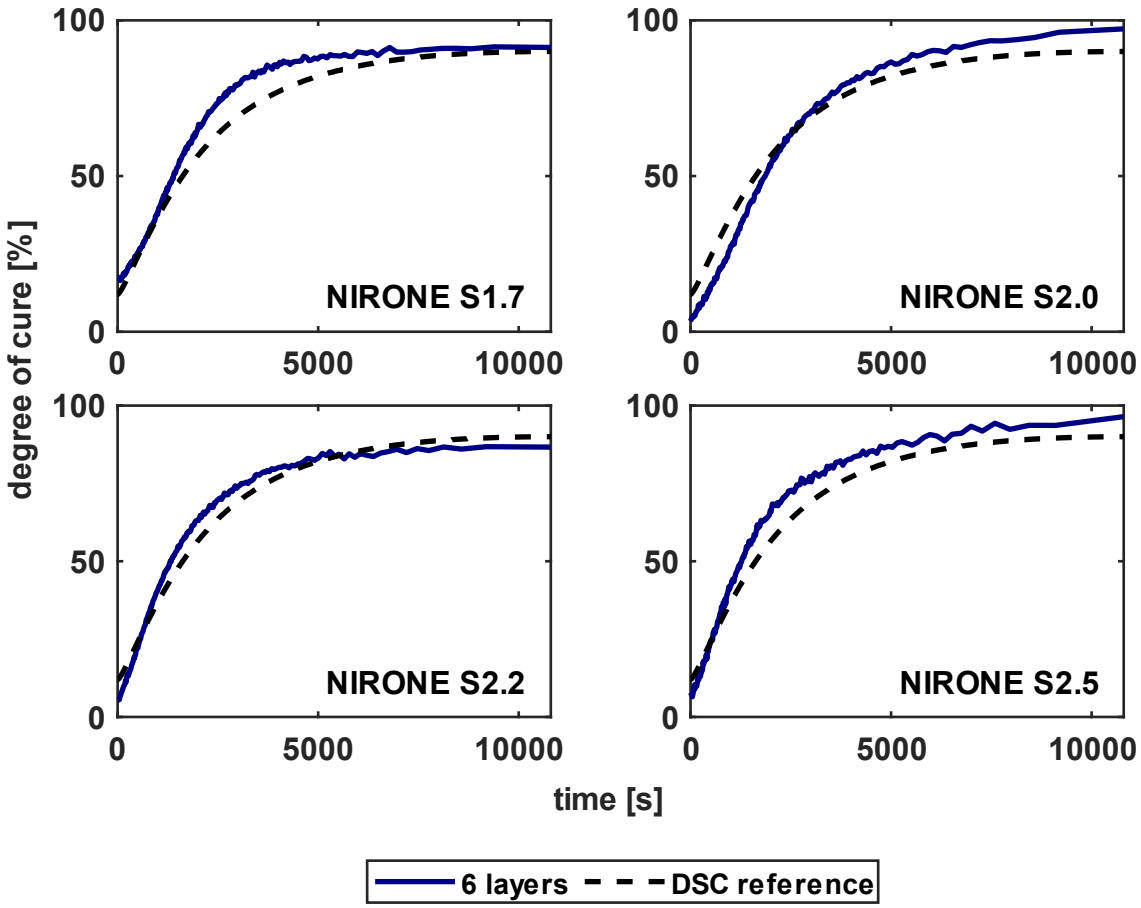

Figure 50: Application of the best PLS-models found to an VARI setup with six layers of GF textile.

values towards the end. Conversely, the NIRONE S2.5 consistently overestimates α until the end. The model S20-2a initially underestimates α, but begins to overestimate it from about 70% onwards. By far, the best predictions are provided by the model S22-2. However, even for this model, the $RMSEP$ is still more than double that of the single-layer setup.

6.5 Discussion

Establishing an appropriate reference analytics method to monitor the curing process in VARI inline using NIR spectroscopy is essential. Utilizing isothermal DSC measurements to obtain the conversion curve necessitates an isothermal process setup for the calibration measurements. PLS models with good predictive accuracy can be developed based on isothermal DSC for the NIRONE spectrometers. However, transferring these models to other layer setups results in some compromises in accuracy.

6.5.1 Reference Method and Experimental Design

The temperature measurements demonstrate that achieving isothermal temperature control in VARI with GF is significantly more straightforward compared to NF. The number of layers has only a minimal impact on the temperature level. A temperature of 57.8 °C was measured for the single-layer setup, while the six-layer setup showed 57.2 °C. These minor differences and similar infusion behavior allowed subsequent VARI experiments to be conducted with the same timeline. In contrast, in the NF textiles discussed in Section 6.1 the exothermic reaction increasingly influenced the temperature profile with more layers. This is not the case with GF textiles, where even the six-layer setup exhibited an almost isothermal temperature profile without an exothermic-induced temperature rise.

The isothermal temperature profile permits the use of isothermal DSC measurements as a reference method for determining the degree of cure. Determining α from samples taken after infusion from the VARI setup allows for the consideration of curing that occurred during the resin system and infusion preparation. The quality of the developed PLS models demonstrates that this approach, combined with stringent time constraints for each process step, fundamentally works well. Otherwise, the r^2 values would be lower and the $RMSE$s

higher, as shown in our similarly structured study on determining α in the RTM process [64]. Despite the significant agreement between the individual experiments and the reference measurement, the increased Cook's distance at the edges indicates deviations among the samples.

The presumed differences in α_{Inf} are likely due to slight variations in the process, such as fluctuating laboratory temperatures. Individual determination for each calibration trial would be advantageous but could not be implemented without damaging the vacuum foil, making NIR measurements impossible. A reason for the increased Cook's distance at the upper end could not be identified. Due to the slower curing rate, potential deviations in α_{Inf} should no longer play a role here. The shrinkage of the resin system during curing certainly affects the NIR spectra and, thus, the PLS models, as it changes the number of functional groups in the measurement volume. However, this shrinkage is mainly linear and does not explain the deviations [104, 105].

Despite the deviations in Cook's distance, the predicted values show only minor deviations from the reference values. The presented approach provides stable PLS models for determining the degree of cure in VARI.

6.5.2 Development and Performance of PLS Models for NIRONE Spectrometers

PLS models were developed for all four NIRONE spectrometers to predict the degree of cure. The models for the NIRONE S1.7 showed significantly poorer performance than the models for the other spectrometers. Plotting α_{NIR} over time reveals at least one reason for the inferior performance of the best PLS model developed for the NIRONE S1.7. Up to approximately 80%, α_{NIR} evolves roughly in line with α_{DSC}; beyond that point, α_{NIR} increasingly lags behind α_{DSC} (see Figure 49). This lag is unrelated to excluding the absorption region of the hydroxy peak (see Figure 51). The PLS model S17-1 also predicts significantly lower degrees of cure for longer curing times despite including the hydroxy peak. It might have been expected that the overall improvement in the model through the reduced wavelength range would concentrate the remaining deviations from the reference value into a smaller section. This is not the case.

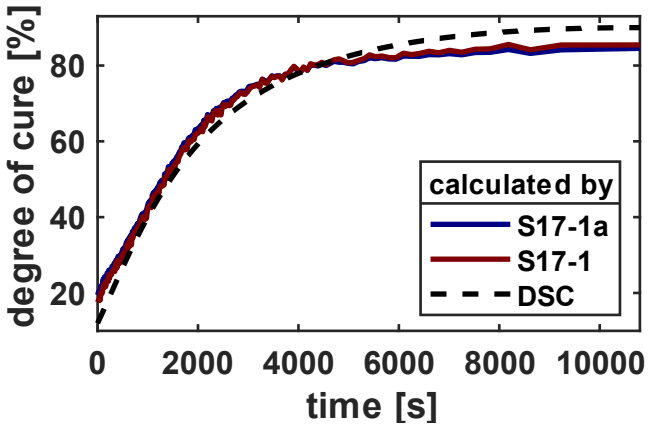

Figure 51: Degree of cure calculated for the first validation trial with the PLS-Models S17-1 and S17-1a.

Other physical effects, such as the greater penetration depths at lower wavelengths and the simultaneously broader absorption regions due to higher-order overtones, can also be ruled out. Otherwise, a trend would also be expected in the PLS models for the other spectrometers. However, this trend is not evident when comparing r^2 or the $RMSE$s.

Unlike S17-1a, in S25-2a no wavelength ranges containing potentially important information have been removed. The model S25-2a performs significantly better than S17-1a, S20-2a and S22-2. No definitive statements can be made regarding the necessary wavelength ranges or desirable absorption peaks in the spectrum, as, for example, not all three relevant functional groups show absorption peaks within the measurement range of S2.2.

During the conception of the experimental series, it was unclear whether the small measurement range of the NIRONE spectrometers could pose problems. Particularly, the interaction with the flow aid and whether the different compositions of the measurement volume from the matrix and the flow aid would lead to issues was uncertain. However, the small measurement volume of the spectrometers does not present a problem; otherwise, more significant fluctuations between the experiments would be expected.

It can be concluded that the degree of cure in VARI can be monitored inline using NIR by simply measuring through the foil. The necessary reference values can be

determined using DSC. The NIRONE spectrometers S2.0, S2.2, and S25 are particularly suitable for epoxy/amine resin systems.

6.5.3 Application to a Six-Layer Structure

The transfer of the developed PLS models for determining the degree of cure to other layer structures in VARI is possible only with significant accuracy losses. The $RSMEP$ increased over all spectrometers and models two to four times compared to the single-layered setup used for calibrating the models and the sixth-layered setup.

The reason for this is likely the altered compaction behavior, which could also affect the measurement volume of the spectrometers. However, the tested six-layer structure exhibits an approximately isothermal temperature profile, suggesting that reliable models for predicting the degree of cure can be developed using the presented approach.

7 Influence of the Mixing Ratios on the Determined Degree of Cure

NIR spectroscopy can measure the mixing ratio and the degree of cure of epoxy/amine resin systems inline (see Chapters 9 and 10). Both parameters play a crucial role in the composite's final properties and are, therefore, critical parameters during the resin system's processing.

The approaches presented in the previous chapters for determining the mixing ratio and the degree of cure using inline NIR spectroscopy ultimately rely on the same parameter: the concentration of epoxy, amine, and hydroxy groups in the measurement volume. Additionally, the concentration of aromatic and aliphatic methylene groups will likely play a role in determining the mixing ratio. However, these are barely recognizable as distinct peaks in the spectra of the NIRONE spectrometers. Since the degree of cure begins to change as soon as the resin and hardener are combined, the question arises about how the degree of cure and the mixing ratio might mutually influence each other when determined using NIR.

A stoichiometric mixing ratio is typically employed for additively curing resin systems, such as the epoxy/amine resin systems investigated here. Deviations from this ratio influence both the achievable degree of cure and the curing kinetics [106].

The following discussion focuses on how the PLS models developed in Chapter 9 respond to deviations in mixing ratios and the extent to which these deviations affect the predicted degree of cure. The potential physical reasons for these effects are not considered. Based on the investigations in Chapter 9, vacuum infusions are conducted using different resin-to-hardener mixtures, and NIR spectra are recorded during curing. Subsequently, using the PLS models from Chapter 9, the progression of curing for each mixture is determined.

7.1 Methods

The experiments' execution corresponds to the procedure outlined in Chapter 6 except for the resin and hardener mixing ratios, which are given in Table 16. The deviations from the nominal weight were below 0.2 g.

Table 16: Used mixing ratios.

Mixing ratio	resin parts	resin weight nominal [g]	hardener parts	hardener weight nominal [g]
100:20	100	200	20	40
100:22	100	200	22	44
100:25	100	200	25	50
100:28	100	200	28	56
100:30	100	200	30	60

7.1.1 Data Evaluation

The degree of cure is determined from the measured spectra using the best model found in Chapter 6. For NIRONE S1.7, this is S17-1a; for NIRONE S2.0, this is S22-2a; for NIRONE S2.2, this is S22-2; and for NIRONE S2.5, this is S25-2a.

7.2 Results

The determined degrees of cure using the PLS models from Chapter 6 follow the expected trend, with increasing curing time resulting in higher degrees of cure (see Figure 52). At the beginning of the curing process, the determined degrees of cure deviate from the expected 12% degree of cure for the correct resin-to-hardener ratio. Still, these deviations do not follow a consistent pattern.

As the curing time progresses, a trend becomes apparent. Adding too little hardener (100:20 and 100:22 ratios) leads to underestimating the degree of cure. The addition of too much hardener (100:28 and 100:30 ratios) results in an overestimation of the degree of cure, or, in the case of NIRONE S2.2, the determined degrees of cure for mixtures of 25, 28, and 30 parts of hardener coincide. Here, a high proportion of hardener (30 parts) temporarily leads to a higher degree of cure between 750 s and 3000 s. Since higher concentrations of hardener can also influence the curing rate, it cannot be ruled out that this deviation is partially kinetically driven. However, the other spectrometers do not exhibit comparable behavior. For NIRONE S2.5, the degree of cure for 30 parts of hardener raises from 13% to 34% after 125 s. The cause of this artifact is unclear but is related to the spectrometer. Since

measurements were taken simultaneously with all four spectrometers, and the other spectrometers show no anomalies, a direct correlation with the experimental procedure can be excluded.

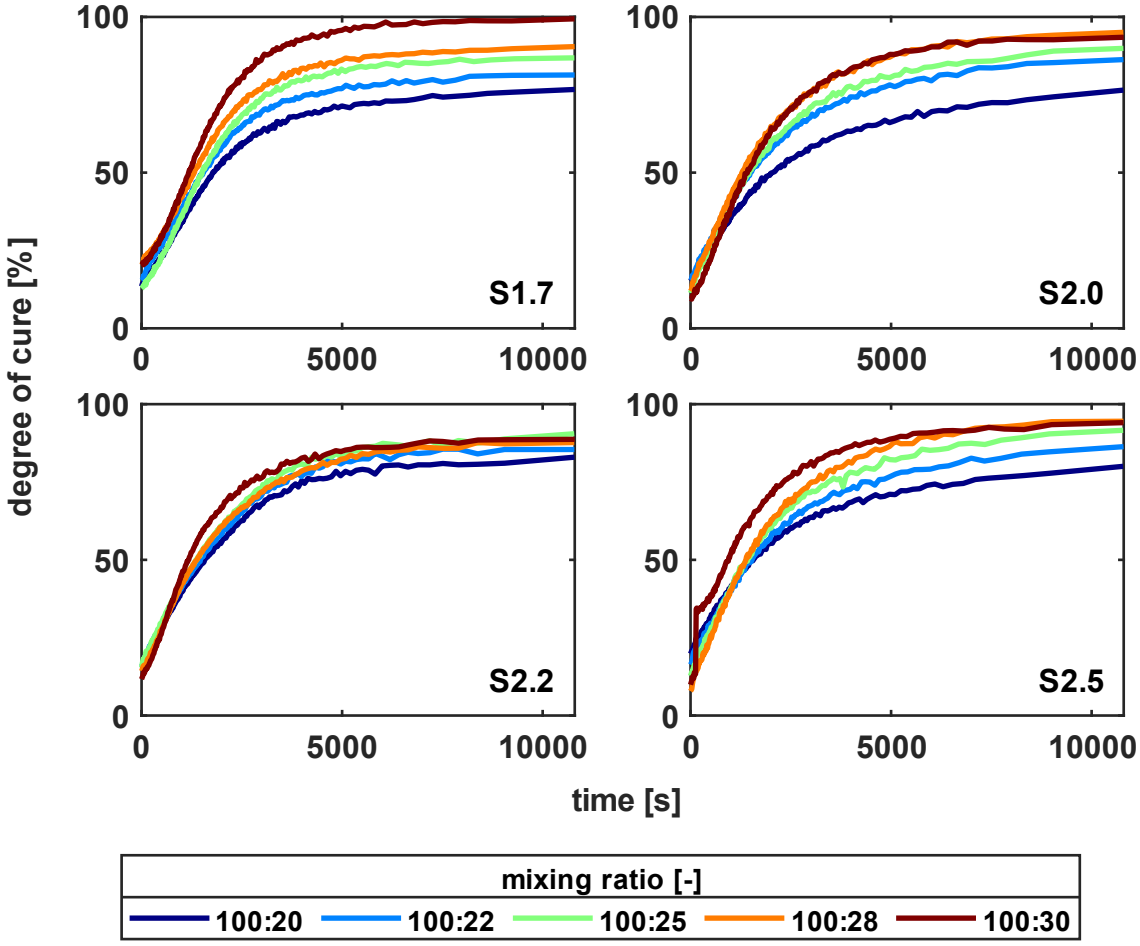

Figure 52: Influence of the diverging mixing ratios on the determined degree of cure.

The integral serves as a measure of the deviation of the degree of cure due to the incorrect hardener ratio, normalized to the 100:25 mixing ratio (see Figure 53). It clearly shows that the deviations from the altered mixing ratio are minimal for NIRONE S2.2. For a mixing ratio of 100:20, the normalized area is 8% smaller, while all other mixing ratios have a deviation of less than 3.5%. In contrast, NIRONE S1.7 exhibits a deviation of up to 16% (mixing ratio 100:30). NIRONE S2.0 and S2.5 show deviations in the determined degree of cure that lie between the other two spectrometers.

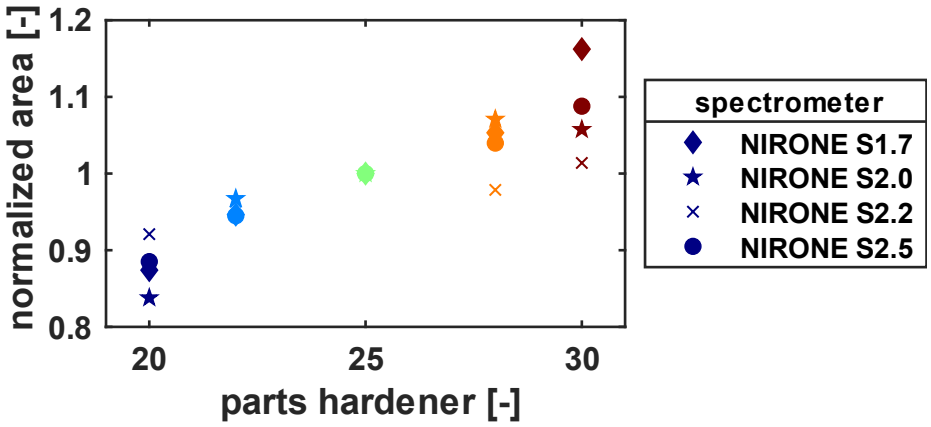

Figure 53: Normalized area under the curing curve determined with different mixing ratios. The colors correspond with the mixing ratios in Figure 52.

7.3 Discussion

The influence of varying mixing ratios on the determined degree of cure was investigated. For all tested PLS models, the predicted degree of cure is affected by the mixing ratio. Adding too little hardener results in an underestimation, whereas an excess hardener results in an overestimation. The S17-1a model increasingly overestimates the achievable degree of cure with a higher excess of hardener, while the S20-2 and S25a models reach a threshold that is not further shifted by additional hardener. The S22-2a PLS model is the least influenced by deviations in hardener ratios.

The PLS models for the NIRONE S1.7 already performed the worst in Chapter 6 and again show the most significant deviation at higher degrees of cure. The other spectrometers showed comparable performance, depending on whether $RMSECV$ or $RMSEP$ is considered. Regarding model stability against fluctuating mixing ratios, the NIRONE S2.2 is the best, as it shows the least variance due to varying mixing ratios across the entire curing range.

When examining the functional groups absorbing in the measurement range, it is noticeable that the NIRONE S2.2 is the only spectrometer that does not directly record information from the epoxy group (see Table 5 and Section 3.2.2). Instead, it only measures the combination peaks of the amine and hydroxy groups. Whether and why this is the reason for the low deviations cannot be determined at this point.

For quality assurance and process monitoring, determining the mixing ratio (see Chapter 5) before using the resin system is advisable. Since the mixing ratio affects the predicted degree of cure, it is also to be expected that the degree of cure affects the predicted mixing ratio. The PLS models for both parameters are based on the same principles and functional groups. The mixing ratio should be determined based on the freshest resin possible before infusion. If the mixing ratio is found to be outside specifications, processing can be halted. If the mixing ratio is within specifications, the degree of cure can be reliably monitored inline with an appropriate spectrometer choice (NIRONE S2.2).

8 Summary and Conclusion

Effective inline process monitoring is crucial for process automation and optimization, as well as for quality assurance and waste reduction. Some processes, including those in the FRPC (Fiber Reinforced Polymer Composites) field, only become technologically feasible through efficient inline monitoring due to their narrow process windows. Thus, inline monitoring offers technological, economic, and ecological benefits. However, the number of applicable technologies for inline monitoring is limited compared to those used for laboratory analysis. This is due to the challenging measurement conditions within the process, the need for short to very short measurement times, and the complexity or sensitivity of the technology or measuring instruments.

Near-infrared (NIR) spectroscopy presents an interesting and previously overlooked technology in the FRPC field due to its versatile and flexible applicability and ability to determine various parameters. It enables the quantification of concentration changes of functional groups in the measurement volume using Partial Least Squares (PLS) regression. Simple and cost-effective measurement optics can be developed using electromagnetic radiation between 750 and 2500 nm, allowing measurements even under difficult process conditions. The spectrometer is connected to these optics via optical fibers and can be placed outside the process, for instance, in a control cabinet.

The present work investigated NIR spectroscopy's applicability along the process chain of Liquid Composite Molding (LCM). LCM processes were chosen as a model because they encompass critical process steps for all FRPCs based on reactive resin systems and are easily accessible. The inline monitored parameters include the fiber moisture content of natural fibers (NF), the mixing ratio of the resin system, both as a pure sample and in Vacuum Assisted Resin Infusion (VARI), and the degree of cure.

Miniaturized NIR spectrometers from the NIRONE series were used. These spectrometers are more economical but less powerful than traditional process spectrometers.

The main research question is if the aforementioned parameters (fiber moisture content, mixing ratio, and degree of cure) are generally measurable with the miniaturized NIR spectrometers used. For this purpose, suitable procedures for collecting reference data were developed. PLS models were developed using the measured NIR spectra and reference data to predict the desired parameters from the NIR spectra. The quality and accuracy of the developed PLS models were then tested with data unknown to the models up to that point.

The fiber moisture content was accurately determined in a closed resin transfer molding (RTM) tool. The water peak at 1924 nm strongly correlates with the fiber moisture content. The developed PLS model (MoC-3a) determines the NF's moisture content with almost the reference method's accuracy. Since the PLS is based on the reference data, a more accurate determination than the reference method is mathematically impossible. Additionally, the applicability of the PLS model to other NF textiles was investigated. The spectra and a previously conducted Principal Component Analysis (PCA) showed no significant differences between the spectra of the different NF textiles. The PLS model predicted the moisture content for all other NF textiles with slightly less accuracy but still with satisfactory precision. Overall, the measurability of another parameter, in addition to the degree of cure, using NIR spectroscopy directly in the RTM tool was demonstrated, and the miniaturized spectrometer used proved its capability.

The mixing ratio was determined from uncured pure resin system samples and in vacuum-assisted resin infusion (VARI) before and after curing. PLS models with sufficient prediction accuracy could be developed for the pure resin system samples. For the measurements in VARI, only quantitative information, such as whether the sample likely lies within a specific range, could be obtained for uncured and cured samples. This is presumably due to more significant fluctuations caused by different optical conditions.

To monitor the degree of cure in VARI using NIR spectroscopy inline, a suitable approach for reference measurements had to be developed first. This approach is based on taking DSC samples at the measurement position after infusion. Since this damages the vacuum bag, the reference data are not from the same experiments as the NIR spectra. Near-isothermal curing had to be ensured using the curing curve

determined by dynamic and isothermal DSC curves as a reference. Therefore, stringent time specifications were made for each process step to achieve the highest possible comparability between experiments. Additionally, only one layer of textile was used for the calibration measurements. This approach also proved successful. In each VARI experiment, measurements were taken with all four commercially available NIRONE spectrometers. Suitable PLS models with good prediction accuracy could be developed for three of the four commercially available NIRONE spectrometers. Only the models for the NIRONE S1.7 significantly underestimated the degree of cure at advanced curing stages. Transferring the PLS model to a thicker layer setup proved difficult. However, temperature measurements of a six-layer setup also showed largely isothermal curing, suggesting that the approach could be transferred to multi-layer VARI setups.

The developed PLS models responded differently to variations in the mixing ratio when predicting the degree of cure. Adding too little hardener resulted in underestimating the degree of cure at higher conversions, sometimes significantly. In contrast, most cases of adding too much hardener reached a threshold that was not exceeded even at higher hardener concentrations. The PLS model for the NIRONE S2.2 was the least affected by varying hardener contents. When there was excess hardener, the degree of cure was not overestimated, while too little hardener only resulted in a slight underestimation.

The miniaturized NIR spectrometers used proved suitable for the chosen applications. A direct comparison with significantly more powerful process spectrometers did not take place. Still, it is known from our investigations that the NIRONE spectrometers, with suitable measurement optics, provide results comparable to process spectrometers. For all investigated parameters, PLS models for predicting the parameters could be developed based on the obtained spectra. The small measurement spot of the NIRONE spectrometers likely proved to be a limitation for the achievable accuracy. Using appropriate measurement optics with a collecting lens and, thus, a larger measurement spot would likely help here. On the other hand, the necessary measurement times (>1 s) did not pose a problem for the parameters to be determined. Whether peaks not involved in the curing reaction could be used to determine the mixing ratio was not investigated but is interesting

for many applications. In the case of the epoxy/amine resin systems used, these would primarily be aromatic and aliphatic hydrocarbon groups. Since these groups hardly appear as distinct peaks in the spectra of the NIRONE spectrometers, the question arises as to how good the physical resolution of the spectrometers needs to be for this measurement.

Overall, a positive conclusion regarding using NIR spectroscopy in the FRPC processing field can be drawn. In addition to the applications shown in the literature for determining essential process parameters in prepreg manufacturing, such as resin and solvent content or degree of pre-curing, further process parameters relevant to FRPC processing could be determined inline using NIR spectroscopy. The demonstrated applications are not specific to LCM processes but should be transferable to other processes without much effort. It was demonstrated that NIR spectroscopy can determine important processing parameters on open samples through a vacuum bag and closed tools. For instance, determining the mixing ratio directly in the mixing unit before impregnating the fibers is conceivable. This would ensure the quality of the resin system and could also serve as a safeguard against liability issues for critical applications. Alternatively, it could be considered for process design. For rotor blades, the curing time is doubled when bonding the rotor blade halves to ensure that even the coolest spot is fully cured. Determining the degree of cure directly in the process at critical points could significantly shorten the curing time and make the process more economical and ecological.

9 References

1. JEC Observer 2024_Overview of the global composites market 2023-2028 (2024)
2. Estin, e.a.: JEC observer. Current trends in the global composites industry 2021-2026. JEC Group, Paris (2022)
3. Bickerton, S., Govignon, Q., Kelly, P.: Resin infusion/liquid composite moulding (LCM) of advanced fibre-reinforced polymer (FRP). In: Advanced Fibre-Reinforced Polymer (FRP) Composites for Structural Applications, pp. 155–186. Elsevier (2013)
4. Neitzel, M., Mitschang, P., Breuer, U.: Handbuch Verbundwerkstoffe. Werkstoffe, Verarbeitung, Anwendung, 2nd edn. Hanser eLibrary. Hanser, München (2014)
5. Fomitchov, P.A., Kim, Y.K., Kromine, A.K., Krishnaswamy, S.: Laser Ultrasonic Array System for Real-Time Cure Monitoring of Polymer-Matrix Composites. Journal of Composite Materials **36**(15), 1889–1901 (2002). doi: 10.1177/0021998302036015245
6. Schmachtenberg, E., zur Schulte Heide, J., Töpker, J.: Application of ultrasonics for the process control of Resin Transfer Moulding (RTM). Polymer Testing **24**(3), 330–338 (2005). doi: 10.1016/j.polymertesting.2004.11.002
7. Yenilmez, B., Murat Sozer, E.: A grid of dielectric sensors to monitor mold filling and resin cure in resin transfer molding. Composites Part A: Applied Science and Manufacturing **40**(4), 476–489 (2009). doi: 10.1016/j.compositesa.2009.01.014
8. Lee, D.G., Kim, H.G.: Non-Isothermal in Situ Dielectric Cure Monitoring for Thermosetting Matrix Composites. Journal of Composite Materials **38**(12), 977–993 (2004). doi: 10.1177/0021998304040563
9. Hergan, P.: Entwicklung einer modellbasierten Fertigungstechnik zur intrinsischen Herstellung von hybriden Verbundwerkstoffen. Dissertation. Montanuniverisität Leoben (2019)
10. Garschke, C., Weimer, C., Parlevliet, P.P., Fox, B.L.: Out-of-autoclave cure cycle study of a resin film infusion process using in situ process monitoring.

Composites Part A: Applied Science and Manufacturing **43**(6), 935–944 (2012). doi: 10.1016/j.compositesa.2012.01.003

11. Konstantopoulos, S., Fauster, E., Schledjewski, R.: Monitoring the production of FRP composites: A review of in-line sensing methods. Express Polym. Lett. **8**(11), 823–840 (2014). doi: 10.3144/expresspolymlett.2014.84
12. Saad, A.G., Jaiswal, P., Jha, S.N.: Non-destructive quality evaluation of intact tomato using VIS-NIR spectroscopy. International Journal of Advanced Research **12**(2), 632–639 (2014)
13. Grassi, S., Alamprese, C.: Advances in NIR spectroscopy applied to process analytical technology in food industries. Current Opinion in Food Science **22**, 17–21 (2018). doi: 10.1016/j.cofs.2017.12.008
14. Bleye, C. de, Chavez, P.-F., Mantanus, J., Marini, R., Hubert, P., Rozet, E., Ziemons, E.: Critical review of near-infrared spectroscopic methods validations in pharmaceutical applications. Journal of pharmaceutical and biomedical analysis **69**, 125–132 (2012). doi: 10.1016/j.jpba.2012.02.003
15. Fonteyne, M., Arruabarrena, J., Beer, J. de, Hellings, M., van den Kerkhof, T., Burggraeve, A., Vervaet, C., Remon, J.P., Beer, T. de: NIR spectroscopic method for the in-line moisture assessment during drying in a six-segmented fluid bed dryer of a continuous tablet production line: Validation of quantifying abilities and uncertainty assessment. Journal of pharmaceutical and biomedical analysis **100**, 21–27 (2014). doi: 10.1016/j.jpba.2014.07.012
16. Li, W., Huang, Y.D., Liu, L., Bo, J.: On-line Monitoring of Resin Content and volatile content in Carbon/Phenolic Resin Prepreg Cloth by Near-Infrared-Spectroscopy. Polymers & Polymer Composites(14), 537–543 (2006)
17. Jiang, B., Huang, Y.: Near Infrared Spectroscopy for On-line Monitoring of Alkali- Free Cloth /Phenolic Resin Prepreg During Manufacture. IJMS **8**(6), 541–552 (2007). doi: 10.3390/i8060541
18. Li, W., Gao, W.J., Chen, P., Sun, B.L.: Near-Infrared Spectroscopy and Principal Components Regression for the Quality Analysis of Glass/Epoxy Prepreg. Polymers and Polymer Composites **19**(1), 15–20 (2010). doi: 10.1177/096739111101900103

19. Burns, D.A., Ciurczak, E.W.: Handbook of near-infrared analysis. Revised and Expanded, 3rd Ed, 3rd edn. Practical spectroscopy, vol. 35. CRC Press, Boca Raton, Fla. (2008)
20. Chu, S., Stoner, J.O., Hurst, G.S.: spectroscopy. spectral analysis (1999)
21. Gottwald, W., Heinrich, K.H.: UV/VIS-Spektroskopie für Anwender. Die Praxis der instrumentellen Analytik. WILEY-VCH, Weinheim (1998)
22. Wei, C., Li, L. (eds.): Acoustic Emission and Ultrasound Monitoring in Laser Micro/Nanofabrication. Springer (2021)
23. Zhu, C., Fu, X., Zhang, J., Qin, K., Wu, C.: Review of portable near infrared spectrometers: Current status and new techniques. J. Near Infrared Spectrosc., JNIRS **30**(2), 51–66 (2022). doi: 10.1177/09670335211030617
24. Shimamoto, J., Hasegawa, K., Kawano, S., Sato, M.: Non-destructive determination of fat content in frozen and thawed mackerel by near infrared spectroscopy. Fisheries Sci **70**(2), 345–347 (2004). doi: 10.1111/j.1444-2906.2003.00812.x
25. Zamora-Rojas, E., Pérez-Marín, D., Pedro-Sanz, E. de, Guerrero-Ginel, J.E., Garrido-Varo, A.: Handheld NIRS analysis for routine meat quality control: Database transfer from at-line instruments. Chemometrics and Intelligent Laboratory Systems **114**, 30–35 (2012). doi: 10.1016/j.chemolab.2012.02.001
26. Camps, C., Simoné, C., Gilli, C.: Assessment of the Tomato Qualtiy using portable NIR Spectroscopy and PLSR with Wavelength selection. Acta Hortic.(936), 437–442 (2012). doi: 10.17660/ActaHortic.2012.936.58
27. Beghi, R., Spinardi, A., Bodria, L., Mignani, I., Guidetti, R.: Apples Nutraceutic Properties Evaluation Through a Visible and Near-Infrared Portable System. Food Bioprocess Technol **6**(9), 2547–2554 (2013). doi: 10.1007/s11947-012-0824-7
28. Rady, A., Fischer, J., Reeves, S., Logan, B., Watson, N.J.: The Effect of Light Intensity, Sensor Height, and Spectral Pre-Processing Methods when using NIR Spectroscopy to Identify Different Allergen-Containing Powdered Foods. Sensors (Basel, Switzerland) **20**(1) (2019). doi: 10.3390/s20010230
29. Yan, H., Siesler, H.W.: Identification of textiles by handheld near infrared spectroscopy: Protecting customers against product counterfeiting. Journal of

Near Infrared Spectroscopy **26**(5), 311–321 (2018). doi: 10.1177/0967033518796669

30. Vakili, H., Wickström, H., Desai, D., Preis, M., Sandler, N.: Application of a handheld NIR spectrometer in prediction of drug content in inkjet printed orodispersible formulations containing prednisolone and levothyroxine. International journal of pharmaceutics **524**(1-2), 414–423 (2017). doi: 10.1016/j.ijpharm.2017.04.014
31. Wilson, B.K., Kaur, H., Allan, E.L., Lozama, A., Bell, D.: A New Handheld Device for the Detection of Falsified Medicines: Demonstration on Falsified Artemisinin-Based Therapies from the Field. The American journal of tropical medicine and hygiene **96**(5), 1117–1123 (2017). doi: 10.4269/ajtmh.16-0904
32. Da Silva Oliveira, V., Honorato, R.S., Honorato, F.A., Pereira, C.F.: Authenticity assessment of banknotes using portable near infrared spectrometer and chemometrics. Forensic science international **286**, 121–127 (2018). doi: 10.1016/j.forsciint.2018.03.001
33. NIRONE Sensor S. https://4905262.fs1.hubspotusercontent-na1.net/hubfs/4905262/SE_NIRONE_Sensor_S_2022_EN_web.pdf?__hstc=192714997.05a93a94c4809fcc8a2f165b99a8e04d.1669801504937.1669801504937.1669801504937.1&__hssc=192714997.1.1669824253495&__hsfp=1516979224&hsCtaTracking=109067f2-aed0-4b7c-b601-100a5e2c2c4f%7C2cf2ce31-1dbf-4735-975d-a012280494a6 (2022). Accessed 30 November 2022
34. MicroNIR 1700ES (2024)
35. Märzinger, W.: FTNIR Prozess-Spektrometer. i-Red Infrarotsysteme GmbH, i-Red Infrarotsysteme GmbH. https://i-red.at/produkte/. Accessed 3 April 2024
36. Salzmann, M., Teuchtmann, M., Schledjewski, R.: Determination of the glass transition temperature of an epoxy prepreg by Near Infrared Spectroscopy. Polymer Testing **125**, 108111 (2023). doi: 10.1016/j.polymertesting.2023.108111
37. Yang, S., Zhao, Z., Yan, H., Siesler, H.W.: Fast detection of cotton content in silk/cotton textiles by handheld near-infrared spectroscopy: a performance comparison of four different instruments. Textile Research Journal **92**(13-14), 2239–2246 (2022). doi: 10.1177/00405175221082324

38. Style Guide: Journal of Near Infrared Spectroscopy
39. Cholake, S., Mada, M., Raman, R., Bai, Y., Zhao, X., Rizkalla, S., Bandyopadhyay, S.: Quantitative Analysis of Curing Mechanisms of Epoxy Resin by Mid- and Near- Fourier Transform Infra Red Spectroscopy. DSJ **64**(3), 314–321 (2014). doi: 10.14429/dsj.64.7326
40. Xu, L., Fu, J.H., Schlup, J.R.: In situ Near-Infrared Spectroscopic Investigation of Epoxy Resin-Aromatic Amine Cure Mechanisms. J. Am. Chem. Soc. **116**(7), 2821–2826 (1994). doi: 10.1021/ja00086a015
41. Billaud, C., Vandeuren, M., Legras, R., Carlier, V.: Quantitative Analysis of Epoxy Resin Cure Reaction: A Study by Near-Infrared Spectroscopy. Appl Spectrosc **56**(11), 1413–1421 (2002). doi: 10.1366/00037020260377706
42. Otto, M.: Chemometrics. Statistics and computer application in analytical chemistry, 2nd edn. WILEY-VCH, Weinheim (2007)
43. Dan, L., Yi-Hui, W.: Rapid identification of epoxy resin and phenolic resin using near infrared spectroscopy. Journal of Near Infrared Spectroscopy **25**(5), 324–329 (2017). doi: 10.1177/0967033517732580
44. Kessler, W.: Multivariate Datenanalyse für die Pharma-, Bio- und Prozessanalytik. Ein Lehrbuch, 1st edn. WILEY-VCH, Weinheim (2008)
45. Precht, M., Kraft, R., Voit, K.: Grundbegriffe - Vektorrechnung - lineare Algebra und Matrizenrechnung - Kombinatorik - Wahrscheinlichkeitsrechnung, 6th edn. Mathematik für Nichtmathematiker / von Manfred Precht Karl Voit Roland Kraft, vol. 1. Oldenbourg, München (2000)
46. Beutelspacher, A.: Lineare Algebra. Eine Einführung in die Wissenschaft der Vektoren, Abbildungen und Matrizen, 6th edn. Vieweg, Wiesbaden (2003)
47. Härdle, W.K., Simar, L.: Applied Multivariate Statistical Analysis. Springer Berlin Heidelberg, Berlin, Heidelberg (2012)
48. Brereton, R.G.: Chemometrics. Data analysis for the laboratory and chemical plant. Wiley, Chichester (2006)
49. Varmuza, K., Filzmoser, P.: Introduction to multivariate statistical analysis in chemometrics. CRC Press, Boca Raton (2009)
50. Teuchtmann, M.: Introduction into Chemometrics, Leoben, 22 November 2022
51. Automated quality inspection of composite materials at a glance - ISRA VISION (2024)

52. Aziz, M.E.: A study on the Effect of Hardener on the Mechanical Properties of epoxy resin. University of Technology, Republic of Iraq (2010)
53. Ferracane, J.L., Greener, E.H.: The effect of resin formulation on the degree of conversion and mechanical properties of dental restorative resins. Journal of biomedical materials research **20**(1), 121–131 (1986). doi: 10.1002/jbm.820200111
54. Ramsdale-Capper, R., Foreman, J.P.: Internal antiplasticisation in highly crosslinked amine cured multifunctional epoxy resins. Polymer **146**, 321–330 (2018). doi: 10.1016/j.polymer.2018.05.048
55. Fu, H., Qin, Y., He, X., Meng, X., Zhong, Y., Zou, Z.: Effect of curing degree on mechanical and thermal properties of 2.5D quartz fiber reinforced boron phenolic composites. e-Polymers **19**(1), 462–469 (2019). doi: 10.1515/epoly-2019-0048
56. Vyazovkin, S., Sbirrazzuoli, N.: Isoconversional Kinetic Analysis of Thermally Stimulated Processes in Polymers. Macromol. Rapid Commun. **27**(18), 1515–1532 (2006). doi: 10.1002/marc.200600404
57. Vyazovkin, S.: A unified approach to kinetic processing of nonisothermal data. Int. J. Chem. Kinet. **28**(2), 95–101 (1996). doi: 10.1002/(SICI)1097-4601(1996)28:2<95:AID-KIN4>3.0.CO;2-G
58. Vyazovkin, S.: Model-free kinetics. J Therm Anal Calorim **83**(1), 45–51 (2006). doi: 10.1007/s10973-005-7044-6
59. Thermal analysis of polymers. John Wiley, Hoboken, N.J (2009)
60. Wu, Y.-H., Li, D.: Determination of ash content in silicon dioxide filled epoxy-phenolic prepreg using near infrared spectroscopy. J. Near Infrared Spectrosc. **30**(4), 227–233 (2022). doi: 10.1364/JNIRS.30.000227
61. Jiang, B., Huang, Y.D.: Quality inspection of laid fabric epoxy resins prepreg by near infrared spectroscopy. Composites Part A: Applied Science and Manufacturing **39**(5), 712–717 (2008). doi: 10.1016/j.compositesa.2008.02.009
62. Li, W., Huang, Y.D., Liu, L., Chen, N.T.: Rapid and nondestructive analysis of quality of prepreg cloth by near-infrared spectroscopy. Composites Science and Technology **65**(11-12), 1668–1674 (2005). doi: 10.1016/j.compscitech.2005.02.005

63. Salzmann, M., Blößl, Y., Todorovic, A., Schledjewski, R.: Usage of Near-Infrared Spectroscopy for Inline Monitoring the Degree of Curing in RTM Processes. Polymers **13**(18) (2021). doi: 10.3390/polym13183145
64. Salzmann, M., Märzinger, W., Teuchtmann, M., Ravindran, B., Kirschnick, U., Fauster, E.: Near-infrared spectroscopy in resin transfer molding—determination of the degree of cure. Int J Adv Manuf Technol (2024). doi: 10.1007/s00170-024-13671-z
65. Pramanik, M., Mendon, S.K., Rawlins, J.W.: Determination of epoxy equivalent weight of glycidyl ether based epoxides via near infrared spectroscopy. Polymer Testing **31**(5), 716–721 (2012). doi: 10.1016/j.polymertesting.2012.04.004
66. Blanco, M., Villaescusa, V.: Use of NIR spectroscopy in the production of modified industrial resins. Talanta **71**(3), 1333–1338 (2007). doi: 10.1016/j.talanta.2006.07.028
67. Blanco, M., Cruz, J., Armengol, M.: Control production of polyester resins by NIR spectroscopy. Microchemical Journal **90**(2), 118–123 (2008). doi: 10.1016/j.microc.2008.04.004
68. Liu, Q., Li, D., Guan, C.: Analysis of initiator content of prepreg by near-infrared spectroscopy. Reviews in Analytical Chemistry **41**(1), 74–82 (2022). doi: 10.1515/revac-2022-0035
69. Bo, J., Yu, D.H., Wei, L., Li, L.: Non-destructive and Rapid Analysis of Resin and Volatile Contents in Carbon Fibre/Epoxy Resin Prepreg Cloth by Near-infrared Spectroscopy. Iranian Polymer Journal(16), 19–326 (2007)
70. Li, W., Huang, Y.D., Chen, P.: Use of Near-Infrared Spectroscopy for On-Line Monitoring the Quality of Prepreg Cloth. Advanced Composites Letters **17**(2), 096369350801700 (2008). doi: 10.1177/096369350801700201
71. Department of Chemistry, Illinois State University: An Introduction to Laboratory Practices in Organic Chemistry. Infrared Spectroscopy. https://cpb-us-w2.wpmucdn.com/about.illinoisstate.edu/dist/3/187/files/2019/10/IR-Reference-Guide.pdf (2015). Accessed 18 November 2022
72. Stuart, B.: Infrared spectroscopy. Fundamentals and applications. Analytical techniques in the sciences. J. Wiley, Chichester West Sussex England, Hoboken NJ (2004)

73. Smith, B.C.: The Infrared Spectra of Polymers V: Epoxies. Spectroscopy, 17–19 (2022). doi: 10.56530/spectroscopy.mg2473z4
74. Brian C. Smith: Organic Nitrogen Compounds III: Secondary and Tertiary Amines. Spectroscopy **34**(5), 22–26 (2019)
75. Brian C. Smith: Organic Nitrogen Compounds II: Primary Amines. Spectroscopy **3**(34), 22–25 (2019)
76. María González González, Juan Carlos Cabanelas and Juan Baselga: Applications of FTIR on Epoxy Resins - Identification, Monitoring the Curing Process, Phase Separation and Water Uptake
77. Nikolic, G., Zlatkovic, S., Cakic, M., Cakic, S., Lacnjevac, C., Rajic, Z.: Fast Fourier transform IR characterization of epoxy GY systems crosslinked with aliphatic and cycloaliphatic EH polyamine adducts. Sensors (Basel, Switzerland) **10**(1), 684–696 (2010). doi: 10.3390/s100100684
78. Maity, P., Kasisomayajula, S., Parameswaran, V., Basu, S., Gupta, N.: Improvement in surface degradation properties of polymer composites due to pre-processed nanometric alumina fillers. IEEE Trans. Dielect. Electr. Insul. **15**(1), 63–72 (2008). doi: 10.1109/T-DEI.2008.4446737
79. Fu, J.H., Schlup, J.R.: Mid- and near-infrared spectroscopic investigations of reactions between phenyl glycidyl ether (PGE) and aromatic amines. J. Appl. Polym. Sci. **49**(2), 219–227 (1993). doi: 10.1002/app.1993.070490204
80. Goddu, R.F., Delker, D.A.: Determination of Terminal Epoxides by Near-Infrared Spectrophotometry. Analytical Chemistry(30), 2013–2016 (1958)
81. Dannenberg, H.: Determination of functional groups in epoxy resins by near-infrared spectroscopy. Polym. Eng. Sci. **3**(1), 78–88 (1963). doi: 10.1002/pen.760030117
82. Mijcovic, J., Andjelic, S.: A Study of Reaction Kinetics by Near-Infrared Spectroscopy. 1. Comprehensive Analysis of a Model Epoxy/Amine System. Macromolecules(28), 2787–2796 (1995)
83. Liu, Q.-F., Li, D., Zeng, Y.-D., Huang, W.-Z.: Determination of gel time of prepreg in copper clad laminate industry by near infrared spectroscopy. Journal of Near Infrared Spectroscopy **29**(1), 5–10 (2021). doi: 10.1177/0967033520963799

84. Mijović, J., Andjelić, S., Kenny, J.M.: In situ real-time monitoring of epoxy/amine kinetics by remote near infrared spectroscopy. Polym. Adv. Technol. **7**(1), 1–16 (1996). doi: 10.1002/(SICI)1099-1581(199601)7:1<1:AID-PAT480>3.0.CO;2-N
85. Chike, K.E., Myrick, M.L., Lyon, R.E., Angel, S.M.: Raman and Near-Infrared Studies of an Epoxy Resin. Appl Spectrosc **47**(10), 1631–1635 (1993). doi: 10.1366/0003702934334714
86. Peck, M.C.P., Carter, R.O., Qaderi, S.B.A.: Near infrared measurements of terminal epoxides in polymer resin systems. I. Analytical considerations. J. Appl. Polym. Sci. **33**(1), 77–86 (1987). doi: 10.1002/app.1987.070330107
87. Lohman, F.H., Norteman Jr., E.: Determination of Primary and Secondary Aliphatic Amines by Near-Infrared Spectrophtometry. Analytical Chemistry(35), 707–711 (1963)
88. Whetsel, K.B., Roberson, W.E., Krell, M.W.: Near-Infrared Spectra of Primary Aromatic Amines. Anal. Chem. **30**(10), 1598–1604 (1958). doi: 10.1021/ac60142a006
89. Blanchard, J., Sobey, A.J.: Comparative design of E-glass and flax structures based on reliability. Composite Structures **225**, 111037 (2019). doi: 10.1016/j.compstruct.2019.111037
90. Zhang, Y., Li, Y., Ma, H., Yu, T.: Tensile and interfacial properties of unidirectional flax/glass fiber reinforced hybrid composites. Composites Science and Technology **88**, 172–177 (2013). doi: 10.1016/j.compscitech.2013.08.037
91. Yan, L., Chouw, N., Jayaraman, K.: Flax fibre and its composites – A review. Composites Part B: Engineering **56**, 296–317 (2014). doi: 10.1016/j.compositesb.2013.08.014
92. Todorovic, A., Blößl, Y., Oreski, G., Resch-Fauster, K.: High-performance composite with 100% bio-based carbon content produced from epoxidized linseed oil, citric acid and flax fiber reinforcement. Composites Part A: Applied Science and Manufacturing **152**, 106666 (2022). doi: 10.1016/j.compositesa.2021.106666

93. Cleve, E., Bach, E., Schollmeyer, E.: Using chemometric methods and NIR spectrophotometry in the textile industry. Analytica Chimica Acta **420**(2), 163–167 (2000). doi: 10.1016/S0003-2670(00)00888-6
94. Minty, R.F., Yang, L., Thomason, J.L.: The influence of hardener-to-epoxy ratio on the interfacial strength in glass fibre reinforced epoxy composites. Composites Part A: Applied Science and Manufacturing **112**, 64–70 (2018). doi: 10.1016/j.compositesa.2018.05.033
95. Produktkatalog 2021/2022. https://www.lange-ritter.de/fileadmin/user_upload/Downloads/Download/l_r_Katalog_2021.pdf. Accessed 25 April 2024
96. Hexion Inc.: EPIKOTE™ Resin MGS™ RIMR 135 and EPIKURE™ Curing Agent MGS™ RIMH 134–RIMH 137 (2006). Accessed 1 May 2024
97. Google Scholar: Results searching for "degree of cure". https://scholar.google.de/scholar?hl=de&as_sdt=0%2C5&q=degree+of+cure&btnG= (2024). Accessed 7 May 2024
98. Li, W., Huang, Y.D., Liu, L., Jiang, B.: The application of near infrared spectroscopy in the quality control analysis of glass/phenolic resin prepreg. J Mater Sci **41**(21), 7183–7189 (2006). doi: 10.1007/s10853-006-0922-x
99. Osugi, R., Hitoshi, T., Lie, K., Gennai, Y.: THERMAL CONDUCTIVITY BEHAVIOR OF NATURAL FIBER-REINFORCED COMPOSITES, Yokohoma, Japan (2009). Accessed 6 May 2024
100. Ramanaiah, K., Ratna Prasad, A.V., Chandra Reddy, K.H.: Mechanical Properties and Thermal Conductivity of Typha angustifolia Natural Fiber–Reinforced Polyester Composites. International Journal of Polymer Analysis and Characterization **16**(7), 496–503 (2011). doi: 10.1080/1023666X.2011.598528
101. Takizawa, Y., Chung, D.D.L.: Through-thickness thermal conduction in glass fiber polymer–matrix composites and its enhancement by composite modification. J Mater Sci **51**(7), 3463–3480 (2016). doi: 10.1007/s10853-015-9665-x
102. Macias, J.D., Bante-Guerra, J., Cervantes-Alvarez, F., Rodrìguez-Gattorno, G., Arés-Muzio, O., Romero-Paredes, H., Arancibia-Bulnes, C.A., Ramos-Sánchez, V., Villafán-Vidales, H.I., Ordonez-Miranda, J., Li Voti, R., Alvarado-

Gil, J.J.: Thermal Characterization of Carbon Fiber-Reinforced Carbon Composites. Appl Compos Mater **26**(1), 321–337 (2019). doi: 10.1007/s10443-018-9694-0

103. Joven, R., Das, R., Ahmed, A., Roozbehjavan, P., Minaie, B.: Thermal Properties of Carbon Fiber-Epoxy Composites with different Fabric Weaves. SAMPE. https://www.researchgate.net/profile/Ronald-Joven/publication/288102626_Thermal_properties_of_carbon_fiber-epoxy_composites_with_different_fabric_weaves/links/56be27e408aee5caccf2f5d3/Thermal-properties-of-carbon-fiber-epoxy-composites-with-different-fabric-weaves.pdf (2011). Accessed 6 May 2024
104. Zarrelli, M., Skordos, A.a., Partridge, I.K.: Investigation of cure induced shrinkage in unreinforced epoxy resin. Plastics, Rubber and Composites Processing and Applications **2002**(31), 377–384
105. Nawab, Y., Shahid, S., Boyard, N., Jacquemin, F.: Chemical shrinkage characterization techniques for thermoset resins and associated composites. J Mater Sci **48**(16), 5387–5409 (2013). doi: 10.1007/s10853-013-7333-6
106. Olaya, M., Shah, S., Maiaru, M.: Thermoset Polymers Characterization as a Function of Cure State Using Off-stoichiometry Proxies (2022). doi: 10.26434/chemrxiv-2022-ddlc9

10 Appendix

Artificial Intelligence (AI) Software used for this work:

Task	AI Software	Share of AI [%]	Comments
Improvement of the linguistic readability	Grammarly (v1.2.79.1406)	100	n/a
Translation German to English	Deepl (24.1.211804)	5	The text was formulated fully in German without the use of further AI tools.
Translation German to English	ChatGPT, V 3.5	25	The text was formulated fully in German without the use of further AI tools.
Text generation from notes or questions	ChatGPT, V 3.5	12	AI-generated text was used as a starting point and then adapted in detail.
Matlab code	ChatGPT, V 3.5	30	Support in writing Matlab code for data structuring and plotting; But no direct data evaluation or deriving plots from data.
Generation of the Title	ChatGPT, V 3.5	100	Based on the texts translated from German

Financial Support:

Main parts of this research work were done within the context of the projects “Reliable and Sustainable composite production for Biobased Components” (RSBC) [Contract No. 858688] and “Spektroskopische Analyse von Prepregs” (SAPP) [Contract No. 883906], funded by the Ministry for Transportation, Innovation and Technology (BMVIT) in frame of the research, technology and innovation initiative “Production of the Future”. I kindly acknowledge the possibilities for my research work which were given to me in the course of these projects